University of California

Los Angeles

Muon Timing and Searches for Heavy Stable Charged Particles with the Compact Muon Solenoid Detector at the Large Hadron Collider

A dissertation submitted in partial satisfaction

of the requirements for the degree

Doctor of Philosophy in Physics and Astronomy

by

Christopher Patrick Farrell

2013

The dissertation of Christopher Patrick Farrell is approved.

_____

Peter Felker

_____

Michael Gutperle

_____

David Saltzberg

_____

Jay Hauser, Committee Chair

University of California, Los Angeles

2013

To my parents who have always been supportive of me

Table of Contents

LIST OF FIGURES

List of Tables

xiii

Acknowledgments

I want to say thank you to my advisor Jay Hauser whose teaching and advice allowed me to grow into a contributing member of the scientific community. Jay has always been available to aid in my understanding of problems and to give ideas when I was unsure of what to do going foward. I could not have completed this work without him.

My development as a physicist has been shaped by discussions and guidance by my colleagues on CMS. The list includes but is not limited to Greg Rakness, Amanda Deisher, Mikhael Ignatenko, Chad Jarvis, Loic Quertenmont, and Todd Adams.

I am also grateful to David Saltzberg, Michael Gutperle, and Peter Felker for being willing to be on my committee and review my dissertation.

Finally I want to thank my family for their constant support. Especially, I want to thank my parents who have always worked to make my life as happy and fulfilling as possible.

<center>Vita</center>

1985	Born, New Jersey, USA.
2008	B.S. Physics, University of Florida.
2008–present	Research Assistant, University of California, Los Angeles.

<center>PUBLICATIONS</center>

S. Chatrchyan *et al.* [CMS Collaboration], "Search for heavy long-lived charged particles in *pp* collisions at $\sqrt{s} = 7$ TeV." *Phys.Lett.*, B713:408–433, 2012.

The CMS Collaboration. "Performance of CMS muon reconstruction in pp collision events at $\sqrt{s} = 7$ TeV." *Journal of Instrumentation*, 7:2P, October 2012.

Abstract of the Dissertation

Muon Timing and Searches for Heavy Stable Charged Particles with the Compact Muon Solenoid Detector at the Large Hadron Collider

by

Christopher Patrick Farrell

Doctor of Philosophy in Physics and Astronomy

University of California, Los Angeles, 2013

Professor Jay Hauser, Chair

Proton–proton collisions at the Large Hadron Collider at $\sqrt{s} = 7$ and 8 TeV are studied using the Compact Muon Solenoid (CMS) detector. The measurement of the arrival time of particles to the muon system of CMS is detailed. The timing is used to associate the particle with the correct proton–proton crossing and to help identify different particles. Additionally, four analyses are presented that use timing and ionization energy loss to search for the production of long-lived charged particles predicted in many theories of new physics. The searches are sensistive to a variety of signatures, including the possibility that the particles will only be detectable during part of their passage through CMS. Limits are placed on the production of long-lived gluinos, stops, staus, and multiply charged particles. The limits are the most stringent in the world to date.

CHAPTER 1

Introduction

Particle physics is concerned with studying what matter is made of and how it interacts at a fundamental level. The desire to understand nature at its most basic level has long been of interest to humankind, dating back to at least the ancient Greek philosophers. The field of particle physics began to come into its own beginning with the discovery of the electron in 1897 by J.J. Thompson [1]. In the more than a century since that discovery, the field has been revolutionized many times. Whenever it seemed that the final piece of the puzzle was within reach a surprising result would be found, fundamental particles shown to be composites, inviolate symmetries found to be broken, or an expanding universe in contradiction to gravitational expectation.

The current state of knowledge in particle physics is contained in the standard model (SM) of particle physics. The SM contains all of the known particles and the way that they interact with one another. The SM has been developed over the last forty years and has proven to be a very successful theory. Numerous experiments have validated the theory with the discovery of predicted particles or agreement of parameter values.

The last particle predicted by the SM to be found is the Higgs Boson. The discovery of the Higgs Boson is one of the reasons the Large Hadron Collider (LHC) was built outside of Geneva, Switzerland. The LHC collides protons at an energy higher than any previous experiment at an extremely high rate [2]

producing many particles in the collisions. Surrounding the points where the LHC brings the protons to a collision are experiments designed to measure and reconstruct the particles emanating from the collisions. Two of these experiments, CMS and ATLAS, announced in June of 2012 the discovery of a new particle with properties like that of the SM Higgs Boson [3, 4], possibly indicating that the last piece of the SM has been found.

Following the history of particle physics, just when the theory looks to be the most stable can be when a discovery revolutionizes the field. There are many models which predict physics beyond the SM [5, 6] that would be produced by the LHC and could be detected by the LHC experiments. One of the most popular models is supersymmetry (SUSY) where all of the SM particles are given a superpartner with spin different by one half. Some of these models, including versions of SUSY, predict the production of new heavy (meta-)stable charged particles (HSCP) which would directly interact with the LHC experiments. All of the long-lived particles in the SM have a small mass meaning that a discovery would be a clear indication that a new theory must be developed to explain these particles.

There are numerous different types of HSCP predicted in the models of new physics and the different types can leave exotic signatures in the LHC detectors. Some types of HSCPs would form composite objects with SM particles and undergo nuclear interactions with the detector material that change the SM particles in the composite particles. This could lead to the HSCP changing its electric charge during its propagation through the detector. Other HSCP could be produced with electric charge not equal to e, the charge of an electron, unlike almost all electrically charged SM particles.

Multiple complimentary searches for HSCP produced at the LHC were car-

ried out using data collected by the CMS experiment and are presented in this work. Each of the searches is designed to be sensitive to different signatures that HSCP could have in CMS but many of the tools and techniques used are common between searches. The searches exploit the characteristics of HSCP that allow them to be separated from the very large background of SM particles. Requirements are placed on these characteristics and the residual background due to SM particles is evaluated. The data are then checked to see whether the observation is consistent with this background. If it is not consistent, then this indicates the presence of a new particle beyond the SM while if it is consistent then this places limits on models of physics beyond the SM.

One of the characteristics that separate an HSCP from a SM particle is the late arrival of HSCP to the outer portion of CMS due to its large mass making it slow moving. In order to observe this, it must be possible to measure the arrival time of hits in the outer portions of CMS. This time measurement is important not only for HSCP but also for SM particles in order to associate them to the correct LHC beam collision and to separate out SM particles not coming from LHC collisions, such as from cosmic rays.

Chapter 2 of this work discusses the SM and a few models of physics beyond the SM. An emphasis is placed on theories which include new long-lived charged particles. In Chapter 3, the experimental apparatus used in this work is presented, this includes the LHC and CMS, in particular parts of the apparatus especially important for searches for long-lived charged particles are given extra detail. Chapter 4 discusses the measurement of the arrival time of hits in the outer portion of CMS. Chapter 5 details four complimentary searches for new heavy long-lived charged particles. Concluding remarks on the presented work are given in Chapter 6.

CHAPTER 2

Relevant Theoretical Issues

2.1 Introduction

Our understanding of particles and how they interact is constantly evolving through new experimental results and theoretical breakthroughs. In this chapter, the current theoretical framework in particle physics is briefly described. Also, theories of physics beyond this framework are introduced, with a focus on theories which predict the existence of new long-lived charged particles.

2.2 Standard Model

The Standard Model (SM) of particle physics is a framework for describing fundamental and composite particles and the forces that govern how they interact. More information about the Standard Model can be found in [7, 1]

Particles in the SM are split into bosons, which have integer spin, and fermions, which have half integer spin. The bosons are the carriers of the forces of the SM while the fermions act as the matter fields.

Formally, the SM is described according to the symmetry group

$$SU(3)_C \times SU(2)_L \times U(1)_Y \tag{2.1}$$

where SU(N) denotes special unitary groups of dimension N. Reading from left

to right the groups represent color, weak isospin, and hypercharge. The color symmetry group is responsible for the strong force which is carried by the gluon. A mixture of the weak isospin and hypercharge groups are responsible for the weak and electromagnetic forces. Left handed fermions are doublets of the isospin group while the right handed fermions are singlets as they do not interact with the raising and lowering operators of the SU(2) group. The weak force is carried by the W and Z bosons while the electromagnetic force is carried by the photon.

The last of the bosons in the SM is the Higgs Boson. The Higgs Boson is a scalar which allows it to have a non-zero vacuum expectation value (VEV). This non-zero VEV breaks the electroweak symmetry and results in the W and Z bosons acquiring mass while the photon remains massless. The Higgs Boson's non-zero VEV also gives mass to the fermions by allowing for a coupling between the singlet right handed fermions and doublet left handed fermions which is otherwise not allowed. In June 2012, the CMS and ATLAS experiments at the Large Hadron Collider (see Ch. 3) announced the discovery of a new particle with properties similar to the Higgs Boson. If the particle is confirmed to be the Higgs Boson, this would represent the final particle of the SM to be discovered.

The fermions in the standard model are split between quarks and leptons. Both the quarks and leptons are arranged into three families with each family containing two quarks and two leptons. The first family contains the up and down quarks, the electron, and the electron neutrino. The second family has the strange and charm quarks, the muon, and the muon neutrino. The third family contains the bottom and top quarks, the tau, and the tau neutrino. The down, strange, and bottom quarks have charge -1e/3 while the up, charm, and top quarks have charge +2e/3. The electron, muon, and tau have charge -1e and all of the neutrinos are electrically neutral. All of the electrically charged particles

in the SM have an antiparticle with the opposite charge.

The quarks and gluons have color charge and interact through the strong force. There are three copies of each quark for each of the three different color charges. The strength of the strong force increases with distance leading to color confinement where no free particles can exist with color charge. Thus all quarks and gluons will form composite particles that are color neutral, called hadrons. There are three combinations of particles that lead to color neutral composites. The first is a quark and an anti-quark referred to as mesons such as a charged pion which is made of an up quark and and down antiquark. The second is three quarks (or anti-quarks) referred to as baryons and includes the proton and neutron. Mesons and baryons can be either electrically charged or neutral. The third is a pair of gluons, this type of particle is theoretically allowed but has never been experimentally observed. It would always be electrically neutral.

When quarks and gluons are produced at high energies, the binding of the strong force normally results in numerous secondary quarks and antiquarks being produced. These quarks and antiquarks will then form hadrons in a process called hadronization. All of the hadrons will be traveling in roughly the same direction resulting in a stream of colinear particles from the production point. This beam of partilces is referred to as a jet.

Most particles in the SM, both fundamental and composite, have very short lifetimes preventing them from being directly detected. The only stable particles in the SM are the electron, proton, photon, and the neutrinos. Additionally, a free neutron has a lifetime of eight minutes but it may be stable inside a nucleus. A few other particles have lifetimes long enough to be detected before decaying including the muon, pion, and kaon.

The proton-proton collisions at the LHC will create vast numbers of these SM

particles. As the strong force has the largest coupling, a large majority of the events will be the production of light quarks and gluons. A small fraction of the events, though a large total number given the very high rate of collisions at the LHC, will produce particles such as W and Z bosons, top quarks, and possibly, if it is confirmed, the Higgs Boson. These particles will quickly decay into other SM particles like muons, electrons, and b quarks. This production of stable and long lived SM particles, particularly muons, form part of the background for the search for HSCP detailed in Chapter 5.

The production of SM particles proceeds not only in the proton-proton collisions at the LHC but also through astrophysical processes. The earth is constantly being bombarded with high momentum protons from astronomical sources. These protons interact with the earth's atmosphere resulting in the production of numerous charged and neutral pions. Charged pions will then decay into high momentum muons. As the muons will have a large relativistic boost, they will be able to reach the earth before decaying. Muons lose only a small amount of energy in interactions with matter, allowing the highest energy cosmic ray muons to penetrate through large amounts of earth. This allows cosmic ray muons to reach the detectors of the LHC potentially creating a background for searches for new physics.

2.3 Beyond Standard Model Theories and Heavy Stable Charged Particles

More information about theories beyond the SM and heavy stable charged particles can be found in [8, 5, 6].

While the SM has proven to be a very robust theory, there are numerous rea-

sons to believe it is not complete. The reasons for this include runaway radiative corrections and large amounts of fine tuning of parameters. At a minimum, the theory must be replaced at the Planck energy scale ($10^{18}GeV$) where the gravitational force becomes as strong as the other forces. To address issues like these numerous theories have been put forth for physics beyond the SM (BSM). If these BSM theories are accurate, evidence of them would likely be present in the high energy collisions produced at the LHC. Some of these BSM theories predict the existence of heavy meta-stable charged particles (HSCP) with lifetimes greater than a few ns, long enough to traverse the length of typical particle detectors.

One of the most popular BSM theories is supersymmetry (SUSY). In SUSY, a new symmetry is added to the SM which gives each SM particle a superpartner particle with spin different by one half. The names of the SUSY particles are generally found by prepending an s (for scalar) to the SUSY partners of spin 1/2 particles, so the SUSY partner of the electron is the selectron, and adding ino to the end of other particles, so the higgs SUSY partner is the higgsino. As no SUSY particles have yet been discovered the symmetry must be broken at some scale giving the SUSY particles masses larger than SM particles. In order to address the unresolved issues in the SM, this mass gap is expected to be no larger than about 1 TeV. In addition to adding a new symmetry, SUSY also predicts the existence of a new multiplicatively conserved quantity called R-parity. SUSY particles have an R-parity value of -1 while SM particles have a value of 1. This implies that the lightest SUSY particle (LSP) will be stable and in most SUSY theories it is taken to be electrically and color neutral so as to be the astronomically observed dark matter.

Other SUSY particles besides the LSP could have a long lifetime in certain areas of SUSY parameter space. In the minimal supersymmetric standard model

(MSSM) the LSP is the neutralino (superpartrner of a neutrino) in most cases. The next lightest SUSY particle (NLSP) can be long-lived if the mass splitting between the NLSP and the LSP is small, this can happen for many different particles as the NLSP. Non-universal squark masses can be used to make the mass difference between the stop and the neutralino too small for the stop decay to a neutralino and a bottom quark to be kinematically allowed. Then the stop decay happens via the radiative decay to a charm quark and neutralino making the stop very long-lived.

Another variant of supersymmetry is split SUSY. In split SUSY, scalar SUSY particles have very large masses while other particles remain at the TeV scale. As gluinos $\tilde{g}$ (superpartners of the gluon) must decay through squarks this can make the gluino quite long-lived.

Gluinos and stops have color charge and as such will form composite hadrons with SM quarks and gluons after production, referred to as $R - hadrons$. These $R - hadrons$ can be mesons, baryons, or, for gluinos, a glue-ball made of a gluino and a SM gluon. $R - hadrons$ can be electrically neutral or have charge Q, taken here and everywhere else in this paper unless otherwise stated as the absolute value of the charge, of 1e or 2e, where e is the charge of the electron. One particularly interesting case is for glue-balls which will always be electrically neutral. The fraction of gluinos forming glue-balls is a free parameter in the theory. If the fraction is 100% then all gluino $R - hadrons$ will be produced electrically neutral.

After the $R - hadrons$ are produced at the LHC, they will propagate out to and interact with the LHC detectors. In the interactions with the detectors it is possible for the electrical charge of the $R - hadron$ to change, possibly going from neutral to charged or from charged to neutral. The process occurs through

an exchange of quarks with the detector material in nuclear interactions. The modelling of these interactions has some uncertainty, of particular interest is the fraction of $R-hadrons$ that will be electrically charged after an interaction. Two models are considered in this work. The first is the model presented in [9, 10] which is referred to as the cloud model where the $R - hadron$ is pictured as a spectator HSCP surrounded by a cloud of light, color-charged SM quarks and gluons. This model results in a mixture of neutral and charged $R - hadrons$ after a nuclear interaction. The second model, referred to as charge-suppressed, results in all $R-hadrons$ becoming neutral after a nuclear interaction as described in [11].

A third possible HSCP in SUSY is the production of long-lived staus $\tilde{\tau}$ in gauge mediated symmetry breaking (GMSB) SUSY [12]. In GMSB, the gravitino is very light and almost always the LSP. GMSB models are characterized by six parameters which determine the mass heirarchy and decays of SUSY particles. One of these parameters is the number N of SU(5) chiral multiplets added to the model which act as "messengers". As long as N is not too small the NLSP is likely to be the stau.

The lifetime of the stau is given by [8]

$$\tau_{Stau} = 0.1 \left(\frac{100 GeV}{m_{Stau}} \right)^5 \left(\frac{m_{\tilde{G}}}{2.4 eV} \right) mm/c \qquad (2.2)$$

with $m_{\tilde{G}}$, the gravitino mass, set by

$$m_{\tilde{G}} = 2.4 c_{Grav} \left(\frac{\sqrt{M\Lambda}}{100 TeV} \right)^2 eV \qquad (2.3)$$

with c_{Grav} being the ratio between the fundamental SUSY breaking scale and the effective one felt by the messenger particles, Λ the effective SUSY breaking scale, and M the mass of the messengers. The parameter C_{Grav} relates to how the

SUSY breaking is transmitted to the messengers, if the communication is done perturbatively then c_{Grav} will be very large giving the stau a long lifetime.

Other BSM theories besides SUSY can also contain HSCPs. An interesting scenario for HSCP is the production of particles with charge not equal to $1e$. One model that includes non-unit charged HSCP is the production of particles that are neutral under $SU(3)_C$ and $SU(2)_L$ but have electric charge meaning they only couple to the photon and Z boson through $U(1)_Y$ interactions [13]. The HSCP could be produced with fractional charge ($< 1e$) or multiple charge ($> 1e$).

CHAPTER 3

Experimental Apparatus

3.1 Introduction

The apparatus used for this paper is a combination of a large particle accelerator complex and a detector used to measure the results of particle collisions. Protons are accelerated and brought to a collision by the Large Hadron Collider (LHC) located outside Geneva, Switzerland spanning the Swiss-French border. The protons are accelerated in smaller linear and cyclical accelerators before being injected into the LHC. The protons are brought to a collision at four spots along the LHC. Surrounding one of these spots is the Compact Muon Solenoid (CMS) detector. The CMS detector consists of multiple subsystems which work together to identify signatures of different types of particles.

3.2 Large Hadron Collider

A full description of the LHC can be found in [2], a short summary is included here. The LHC is a two-ring superconducting synchotron designed to collide particles at high energy and high luminosity. It sits in a 26.7 km tunnel located 45-170m underneath the Swiss-French countryside outside of Geneva, Switzerland. The LHC can create collisions with either protons or heavier ions. This leads to three possible operational modes, proton-proton, ion-ion, and proton-ion. Only

in proton-proton operational mode is there a possibility to discover HSCPs and it is the only mode discussed in this paper.

The LHC was designed to accelerate protons to an energy of seven TeV and collide them at a center of mass energy($\sqrt{s}$) of fourteen TeV with an instantaneous luminosity of $10^{34}cm^{-2}s^{-1}$. The protons are brought to a collision at four points along the LHC beamline. Surrounding two of these interaction points sit the general purpose detectors of CMS and ATLAS. These detectors are meant to recieve the highest instantaneous luminosity the LHC can supply. The other interaction points are surrounded by the special purpose detectors LHCb and ALICE and are designed to have instantaneous luminosities of $2 \times 10^{29}cm^{-2}s^{-1}$ and $10^{27}cm^{-2}s^{-1}$, respectively. This paper considers data collected by the CMS detector.

The acceleration of protons to their final energy of 7 TeV is done in series of steps employing smaller accelerators located on the CERN campus. The protons originate in the linear accelerator Linac2 where they are passed through a series of synchotron accelerators, the Proton Synchotron Booster, the Proton Synchotron, and the Super Proton Synchotron, with their energy raised to 1.4 GeV, 25 GeV, and 450 GeV, respectively. After passing through the Super Proton Synchotron the protons are passed into the LHC. The LHC then accelerates the protons to their final design energy of 7 TeV.

The beams are designed to contain proton bunches spaced such that collisions at the interaction points occur every 25ns. The LHC can hold a total of 2,808 bunches, in some places it is designed to have are gaps larger than 25ns between bunches to allow for dumping of the beam without harming the LHC. Each 25ns time window is referred to as a bunch crossing window, whether there are proton bunches colliding in CMS or not. Each collision between the proton

bunches can result in more than one proton-proton collision. This results in the the detectors around the LHC interaction points seeing numerous proton-proton collisions overlayed on one another.

The commisioning of the LHC saw it run at a progression of lower energies building towards the design energy. In 2008 the LHC was run at $\sqrt{s} = 900$ GeV and for a short period at 2.36 TeV. Then after further work on the LHC, the energy was raised to 7 TeV for both 2010 and 2011 and then to 8 TeV in 2012. This paper only covers the data collected at 7 and 8 TeV in 2011 and 2012. It is planned to raise the energy to its design goal of 14 TeV through additional work on the LHC and the injector system.

Similarly, the instantaneous luminosity was ramped up during the commisioning phase. During the 2012 running, the machine ran with the proton bunches separated by 50ns. The instantaneous luminosity often reached $7 \times 10^{33} cm^{-2} s^{-1}$. With 50ns spacing this means that the per bunch luminosity actually exceeded the design value. It is planned to run with 25ns bunch spacing in future LHC running.

3.3 Compact Muon Solenoid

The CMS detector is built around one of the interaction points of the LHC. A full description of CMS be found in references [14, 15].

CMS was designed to be a general purpose detector that would have sensitivity to a wide range of physics. This is important for a search for HSCP as the detector is used in ways not typically done in most CMS analyses. The central feature of CMS is a superconducting solenoid magnet with a 6m diameter and 13m length that provides a 3.8T magnetic field. The return field from the solenoid is

powerful enough to saturate 1.5m of iron, this allows for a strong magnetic field to be present outside of the solenoid. CMS has a cylindrical shape with an onion like design where inner subdetectors are nested inside of outer ones. From inside out these subdetectors are an all silicon tracker, an electromagnetic and hadronic calorimeter, the magnet, and finally the muon system. The various subdetectors and their role in identifying SM particles can be seen in Figs 3.1 and 3.2.

CMS employs a right handed coordinate system with the x-axis pointing to the center of the LHC ring, the y-axis pointing vertically upward, and thus making the z-axis be along the beam line pointing in the clockwise direction if looking at the LHC from above. The azimuthal angle, θ, is defined relative to the z-axis. The variable psuedorapidity, η, is defined as $\eta = -\ln\left[\tan\left(\theta/2\right)\right]$. The polar angle, ϕ, is defined relative to the x-axis, meaning that vertically upward (downward) has a ϕ value of $\pi/2$ $(-\pi/2)$.

The possibility that a particle containing an HSCP can interact with the detector and change its charge means that it may not look like any of the particles in Figure 3.2. The particle may be produced neutral and only gain charge as it passes through the calorimeter. The only record of its hits will be in the muon system giving the signature shown in Figure 3.3. In addition, the particle may be produced charged charged but then become neutral after interacting with CMS giving the signature shown in Figure 3.4. To discover HSCP with these exotic signatures it is necessary to conduct dedicated searches. Searches of this type are presented in Chapter 5.

3.3.1   Subdetectors

The innermost part of CMS is an all silicon tracker. Closest to the interaction point are pixel detectors with three barrel layers and two endcap disks, totalling
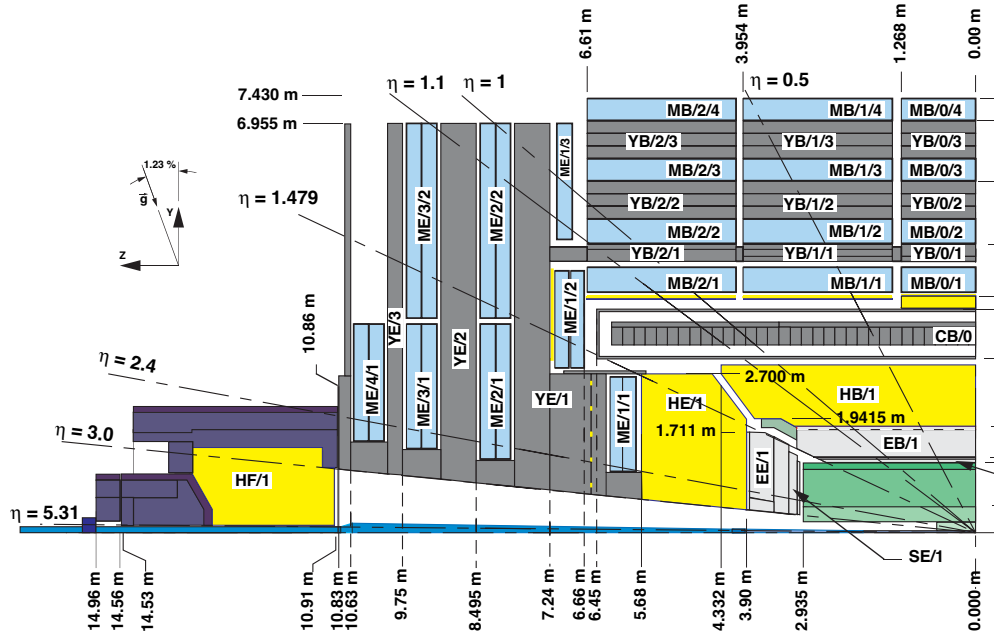
Figure 3.1: Cross section of CMS detector. Inner silicon track bottom right in green, electromagnetic and hadronic calorimeter in light gray and yellow, respectively. Muon detectors on the outside in blue.
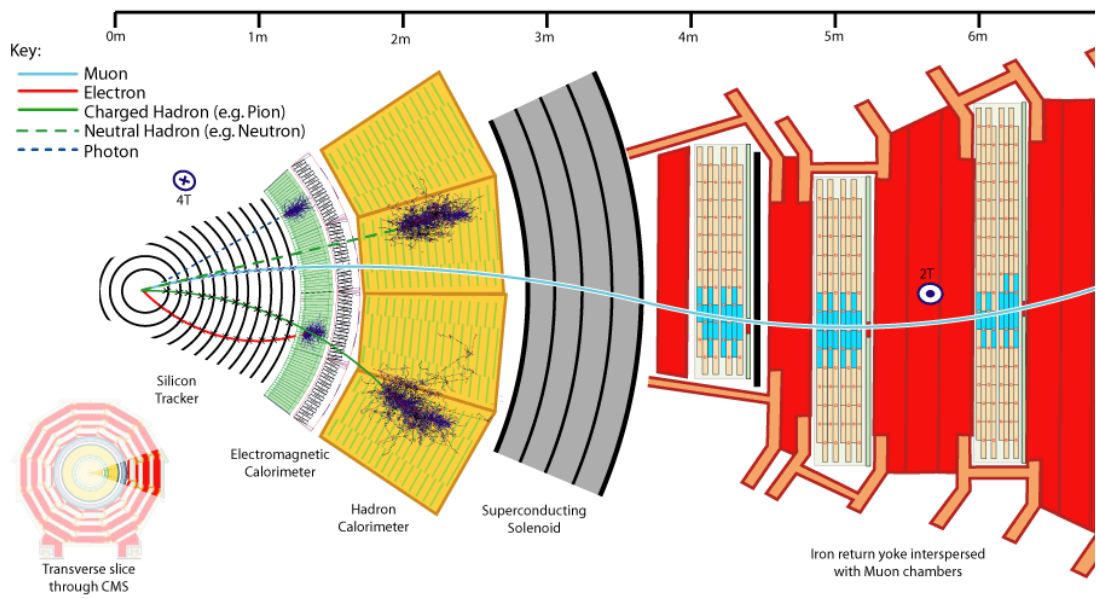
Figure 3.2: Expected interactions of SM particles as they propagate through CMS.
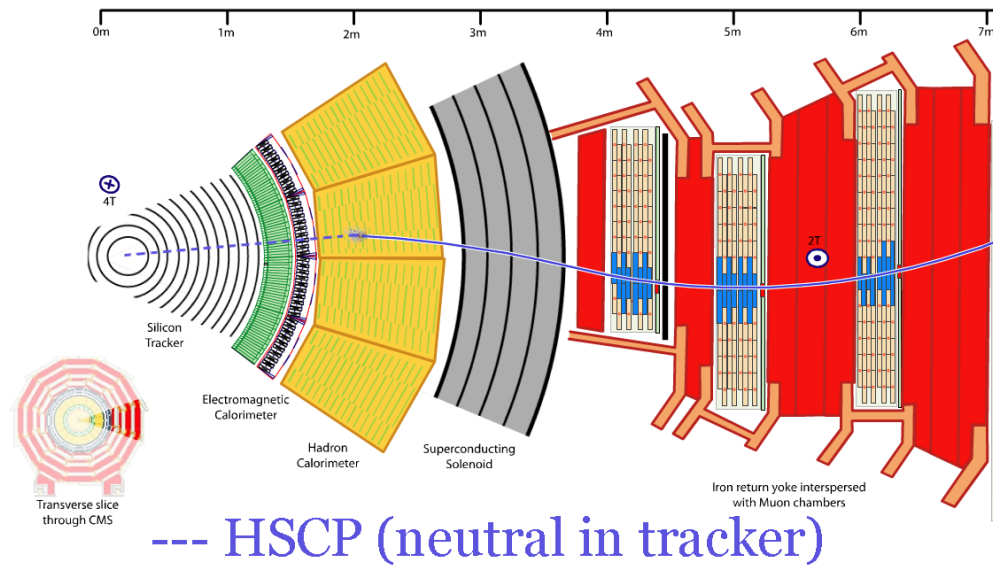
Figure 3.3: HSCP produced neutral and only becoming charged after interacting with the CMS detector.

18
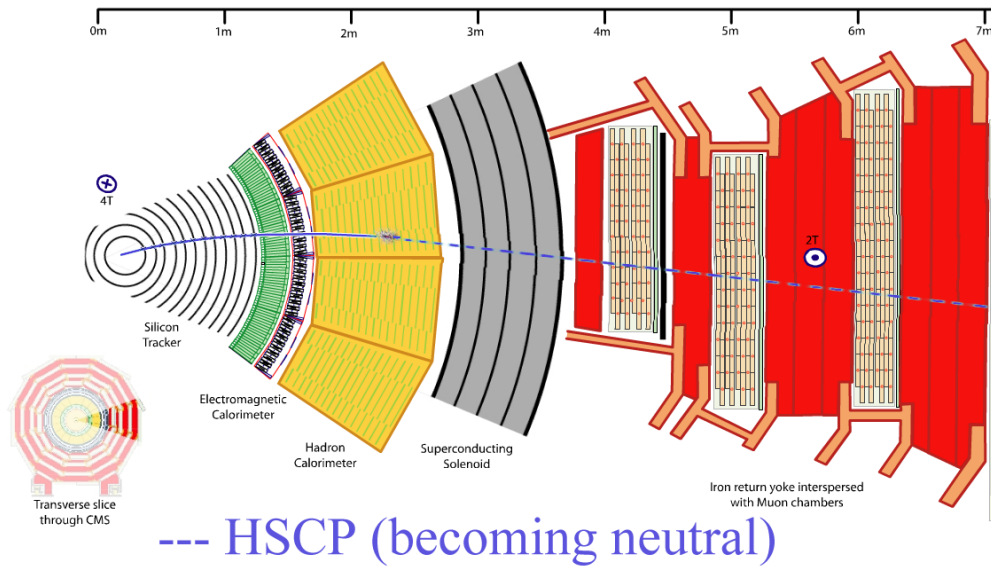
Figure 3.4: HSCP produced charged and only becoming neutral after interacting with the CMS detector.

1,440 modules. Outside of this are strip detectors with ten barrel layers and twelve endcap disks. It extends up to a psuedorapidity range of 2.5 with the resolution on track p_T being approxiamtely 1.5% for a 100 GeV/c particle at $|\eta| = 1.6$ and growing larger at high $|\eta|$ due to the decreased lever arm. Both the strips and the pixels have an analog readout of the deposited charge with a maximum readout of roughly three times the charge expected to be deposited by a muon. Charge from particles traversing the inner tracker is expected to be spread out among multiple modules in the same layer allowing the position of the particle to be calculated more precisely then simply the center of the module. The charge sharing also allows the possibility to identify hits where two particles have overlapped.

Outside of the inner tracker is the calorimeter. The purpose of the calorimeter is to measure the energy of particles and aid in their identification by stopping particles at different points in the calorimeter. The calorimeter is split into an inner electromagnetic calorimeter (ECAL) and an outer hadronic calorimeter (HCAL). The ECAL is made of 75,848 lead tungstate ($PBWO_4$) crystals split between the barrel and endcap. As particles lose energy in the ECAL the crystals emit scintillation light which is collected by photodetectors. The HCAL consists of plates of brass absorbers interleaved with scintillator detectors. Electrons and photons are likely to stop in the ECAL where they deposit all of their energies. Hadrons, electrically charged or neutral, will deposit some energy in the ECAL but will deposit most in the HCAL where they are very likely to come to a rest. Muons will deposit of the order of two GeV of energy in the calorimeter and are generally the only charged SM particles that are able to exit the calorimeter.

The outermost part of the detector is the muon system which is split into three parts, Cathode Strip Chambers(CSC), Drift Tubes(DT), and Resistive

Plate Chambers(RPC). The CSC cover the forward part of the detector with $|\eta| > 0.9$ while the DT and the RPC cover the barrel portion extending up to $|\eta|$ of 1.2 and 1.6, respectively. The muon system is comprised of four stations of chambers with the lead for the magnet return yoke located between the stations. The magnet return yoke provides a magnetic field in the muon system.

CSC chambers have a trapezoidal shape with six layers of cathode strips and anode wires arranged in a nearly orthogonal pattern. The strips run radially away from the beam line and measure the ϕ of hits while the wires measure the radial position of hits. Charge collected on the wires is passed to a constant fraction discriminator which outputs a 40ns pulse. The pulse is sampled every 25ns and this sampling is readout. The amount of charge on the strips is readout every 50ns. The charge is used offline to get a more precise estimate of the position and time of the hit. The CSCs are layed out with four stations with increasing z from the interaction point and rings of increasing radial distance from the beam line.

DT chambers have two or three superlayers which themselves are composed of four layers of drift cells which are staggered by half a cell. All of the DT chambers have two superlayers oriented parallel to the beam line, these superlayers measure the position of particles in the $r - \phi$ plane. The three inner stations additionally have a superlayer running perpendicular to the beamline to measure the position of particles in the $r - z$ plane.

RPC chambers are gaseous parallel plate detectors that can provide a time resolution of 2ns, which is much smaller than the design LHC bunch spacing of 25ns allowing for a very high efficiency to correctly tag hits with the correct event. The spatial resolution is sufficient to be able to associate RPC hits with hits from the other muon subdetectors.

3.3.2 Computing

The rate of proton-proton collisions inside of CMS is too large for all of them to be readout and stored offline. To deal with this CMS employs a two level trigger that selects interesting events online. The level one (L1) trigger must reduce the rate of events readout to less than 100 kHz in less than $3\mu s$ requiring a completely firmware based approach. Events are selected by a variety of algorithms but most of them look for a high momentum track in the muon system, large amount of energy in the ECAL or HCAL, or a combination of these. Signals from these systems trigger the readout of the rest of detector through the data acquisition system. As the LHC was designed to operate with 25 ns bunch spacing many of the subsystems, the tracker especially, only readout the data in the 25ns window associated with the event. This means that triggers that pre or post-fire will not contain much of the data from the event. This can be issue for HSCP that are travelling so slowly that they reach the muon system in the time window associated with the next bunch crossing window. However, a special configuration of the RPC trigger exploits the fact that current running of the LHC has been done with at least 50ns spacing

All hits in the RPC are sent to the trigger electronics twice, once for the bunch crossing window they are associated with and also for the one proceeding it. From there the trigger electronics treat the advanced RPC hits in the same manner as they do all other hits. This allows the RPCs to trigger the readout of the event preceeding the arrival of the particle in the RPCs. This means that HSCP which arrive to the muon system up to 37.5ns after a muon is expected could still trigger the readout of the correct data in the rest of the detector.

To ensure collision muons still maintain the correct behavior, accept signals sent for the bunch crossing window immediately preceeding a bunch crossing

window with protons passing through CMS are rejected. So signals from collision muons will attempt to pretrigger but this will be vetoed and the following event will be correctly readout. This configuration is only possible when proton collsions are spaced by at least 50ns so that accept signals from successive 25ns bunch crossing windows can be unambiguously classified.

The next step in the trigger is the High Level Trigger (HLT) which must reduce the number of events to a few hundred Hz on the order of a second. The HLT is software based and there are a wide variety of algorithms used to identify interesting events and store them for offline analysis. The HLT is split into two different phases, Level 2 (L2), and Level 3 (L3). The L2 step is mostly concerned with confirming the L1 decision and reducing the rate so that higher level objects can be built within the time restrictions. The L3 step builds these objects, often reconstructing tracks of particles in the inner tracker and matching them to objects in other parts of the detector, and then applies requirements on the objects selecting which events to pass for storage at computers located at CERN and throughout the world.

CMS maintains a software, CMSSW, which is responsible for taking the raw data readout from CMS and reconstructing what was happening in the event. This includes applying calibration constants, finding tracks, and indentifying particles. After this reconstruction, the data size is at the scale of petabytes which is too large for offline analyzers to run over frequently. To deal with this copies of the data are produced dropping lower level quantities and selecting only events that a particular analysis is interested in studying.

CMSSW is also tasked with simulating how particles, coming from both SM processes and new physics, would interact with the detector so that this can be used to compare against data. Two steps are performed before the simulation

has the same format as data readout from the detector, at that point it follows the same chain as data. The first step is the simulation of the proton-proton collision and the particles that are created from it, the detector is not used at all in this step. The next step is the simulation of the interaction of these particles with the detector and the behavior of the detector electronics, including the L1 trigger. After this point, the simulation is handled the same as data.

CHAPTER 4

Muon System Timing

4.1 Foreword

This chapter details the measurement of the arrival time of particles in the muon system of CMS. A particular focus is put on the measurement in the CSC system with a description of the measurements in the whole of the muon system given at the end.

4.2 Introduction

Muons coming from collisions in the LHC take approxiamtely 25-40ns to travel from the interaction point to the muon system. As CMS was designed to collect data with protons colliding every 25ns the time of flight (TOF) of muons is a significant time interval. The muon system must be able to associate tracks in the system to the correct bunch crossing window for the L1 trigger. This is required to trigger the readout of the data in the rest of the detector associated with the collsion that the track came from. The method to determine timing synchronization of the CSC subsystem is described below.

Additionally, the timing in the muon system can be used to separate out different sources of tracks. These sources include collision muons from the triggered bunch crossing wondow, muons from adjacent bunch crossing windows, muons

from cosmic rays, and possibly HSCPs predicted in theories of new physics. To do this the time of hits in the muon system is measured and a combined time for each track is calculated.

4.3 CSC Hit Timing

Hits in the CSCs are found from a combination of signals from the anode wires and cathode strips. Both of the signals can be used to estimate the time of the hits.

Time is measured by the cathode strips in two ways, one for online use in the L1 trigger and one for offline measurement. The online measurement finds the peak of the charge distribution and associates it with the particular bunch crossing window. For offline determination of the position and time of the hits, the charge on cathode strips is sampled every 50ns. The time of the hits is estimated with a fit to the charge distribution. Calibration constants are subtracted from the times during reconstruction to center the times at zero. The constants are found for each chamber and are derived from times associated with high quality, high momentum muons. Cathode times have a resolution of approxiamtely 7.0ns.

As stated in Section 3.3.1, signals from the anode wires are passed to a constant fraction discriminator which outputs a 40ns pulse that is then digitized every 25ns. Depending on when the pulse starts, the hit can have either one or two bits being high. Given the same first high bit, it can be inferred that hits with the next bit low arrived earlier than hits with the next bit high. Hits with only one high bit are estimated to have arrived at the time of that bit while those with two high are estiamted to be from the average of the two bits. Thus, it is possible to estimate the time of anode hits with a 12.5 ns quantization. The
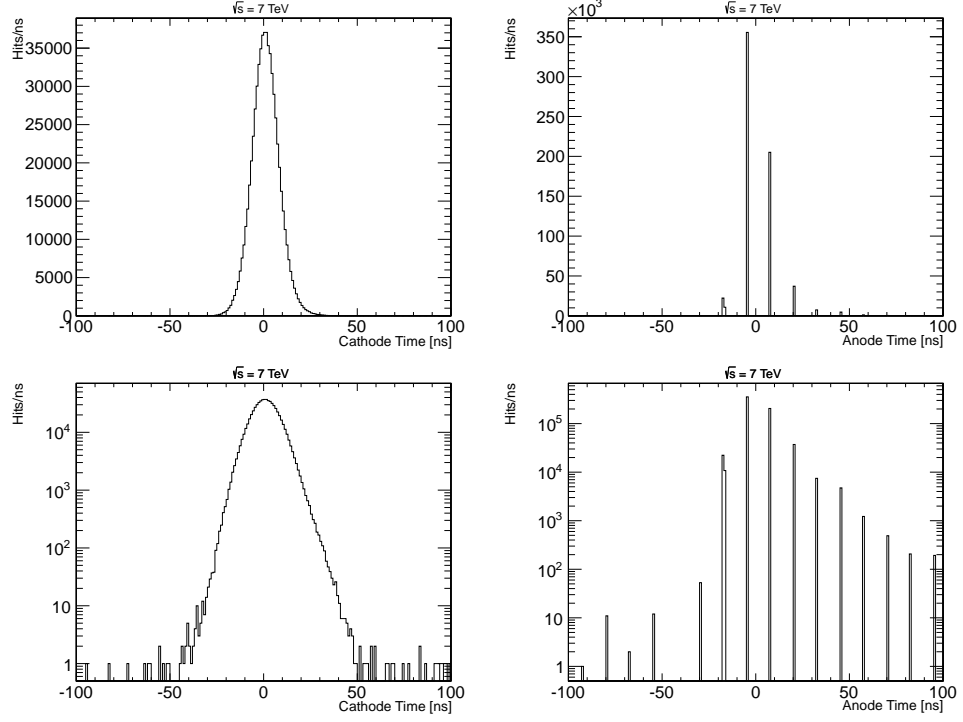
Figure 4.1: Left column: Distribution of cathode time of hits. Right column: Distribution of anode time of hits. Top row: Linear scale. Bottom row: Log scale.

anode times are calibrated to have a mean of zero in the same method as per the cathode times. The resolution of the anode hit timing is approximately 8.6 ns

The distribution of the time of anode and cathode hits associated with high quality, high momentum muons is shown in Fig 4.1. As can be seen in the right plot the anode time has a large tail of positive times. This is dealt with by a cleaning procedure defined below.

The anode and cathode hits in a chamber are used to reconstruct a segment which is meant to represent the passage of the particle through the chamber. A time is associated with the segments by averaging the anode and cathode times
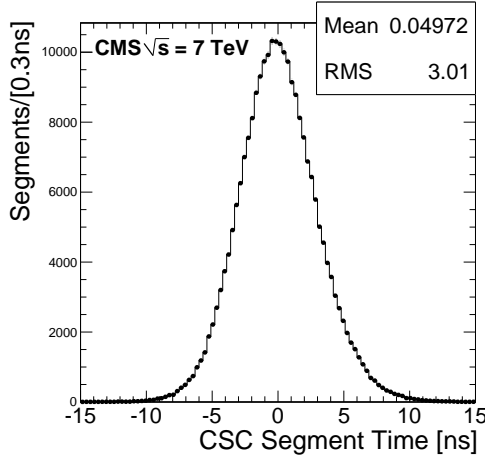
Figure 4.2: Times of segments associated with high quality muons.

associated with the segments. The times are weighted by one over their variance. To remove the large tail in the anode time measurement, a cleaning procedure is applied to the anode times to remove outlier hits. The procedure removes anode times more than three sigma different from the average. The times of segments associated with high quality muons is shown in Fig. 4.2. The resolution on the segment times is 3.0ns.

4.4   CSC Trigger Timing

The CSCs are a key component of the L1 trigger system and it is important that they associate tracks in the system with the correct LHC bunch crossing window. The CSCs build tracks for the L1 trigger with the CSC Track Finder (CSCTF) by combining track stubs coming from the CSC chambers. The stubs are associated with a particular bunch crossing window and the track finder uses majority logic of the stubs used to build the track to associate the track with a bunch crossing window. In cases where there are an equal number of stubs

from different bunch crossing windows, say two track stubs coming from adjacent bunch crossing windows, the CSCTF preferentially selects the later bunch crossing window.

As mentioned in Section 3.3.1, there are six layers of cathode strips and anode wires in a CSC chamber. Electronics on the chamber collect hits from the cathode strips and anode wires and separately create trigger primitives called Cathode Local Charged Track (CLCT) and Anode Local Charged Track (ALCT), respectively. The two separate trigger primitives are then combined to form a Local Charged Track (LCT). The trigger primitives must be associated with events within three bunch crossing windows of one another to be combined. The bunch crossing window that the LCT is associated with is set by the ALCT.

The timing of the ALCT is determined by the timing of the third anode hit, its first high bit, to arrive to the ALCT circuit board. A common offset per chamber can be applied to the anode hits to give the best timing synchronization of the ALCTs. To determine the offset the arrival time of the anode hits is studied offline using hits from high quality muons. The average time of the anode hits can be correlated with the probability for a chamber to produce an ALCT in the bunch crossing window before it should (pretrigger) and after it should (posttrigger). The offsets for each chamber can be tuned to give an expected pretrigger and posttrigger probability.

However, the CSCTF logic means that simply setting the offset to give an equal probability to pretrigger and posttrigger is not optimal. This can be seen by looking at the case where the CSCTF only receives two track stubs, this is also the case where the CSC online timing is most important. If the CSCTF receives one LCT in the bunch crossing window before the collision and one in the correct bunch crossing window, it will preferentially choose the later LCT and

associate the combined track with the correct bunch crossing window. In order to pretrigger the readout of the event more than one LCT must arrive early. On the other hand, if it recieves one LCT in the correct bunch crossing window and one in the proceeding bunch crossing window, the track will be associated with the bunch crossing window following the collision. Thus, the probability to pretrigger the event can be written as P_{LCTPre}^2 while the posttrigger probability can be written as $2 \times P_{LCTPost} - P_{LCTPost}^2$.

Figure 4.3 shows the probabilities to pretrigger and posttrigger both at the chamber level and the expected probability at the CSCTF versus the average anode time of a chamber. The chambers are split into three categories depending on which station and ring they belong to. One category is chambers in the first ring and station, another the chambers in the first ring not in the first station, and the last those not in the first ring. The design of these chambers are all slightly different so it is allowed for them to have different optimal times.

From these plots an optimal value of 204ns is chosen for the chambers in the first ring not in the first station and 205ns for all other chambers. The plot of the pretriggering and posttriggering in the track finder somewhat implies an earlier optimal but these are not used for two reasons. The first is that pretriggering grows as the square of the pretriggering probability and since, as described below, the offsets can not be set exactly, chambers that are slightly below optimal could lead to significant pretriggering in those chambers. Second, pretriggering prevents the readout of the collision event even by another portion of the detector, CMS can not readout two consecutive events, while posttriggering does not have this issue. For these reasons slightly later times that still have very low posttriggering are used.

The offsets can be moved in roughly 2 ns steps in the chamber firmware with
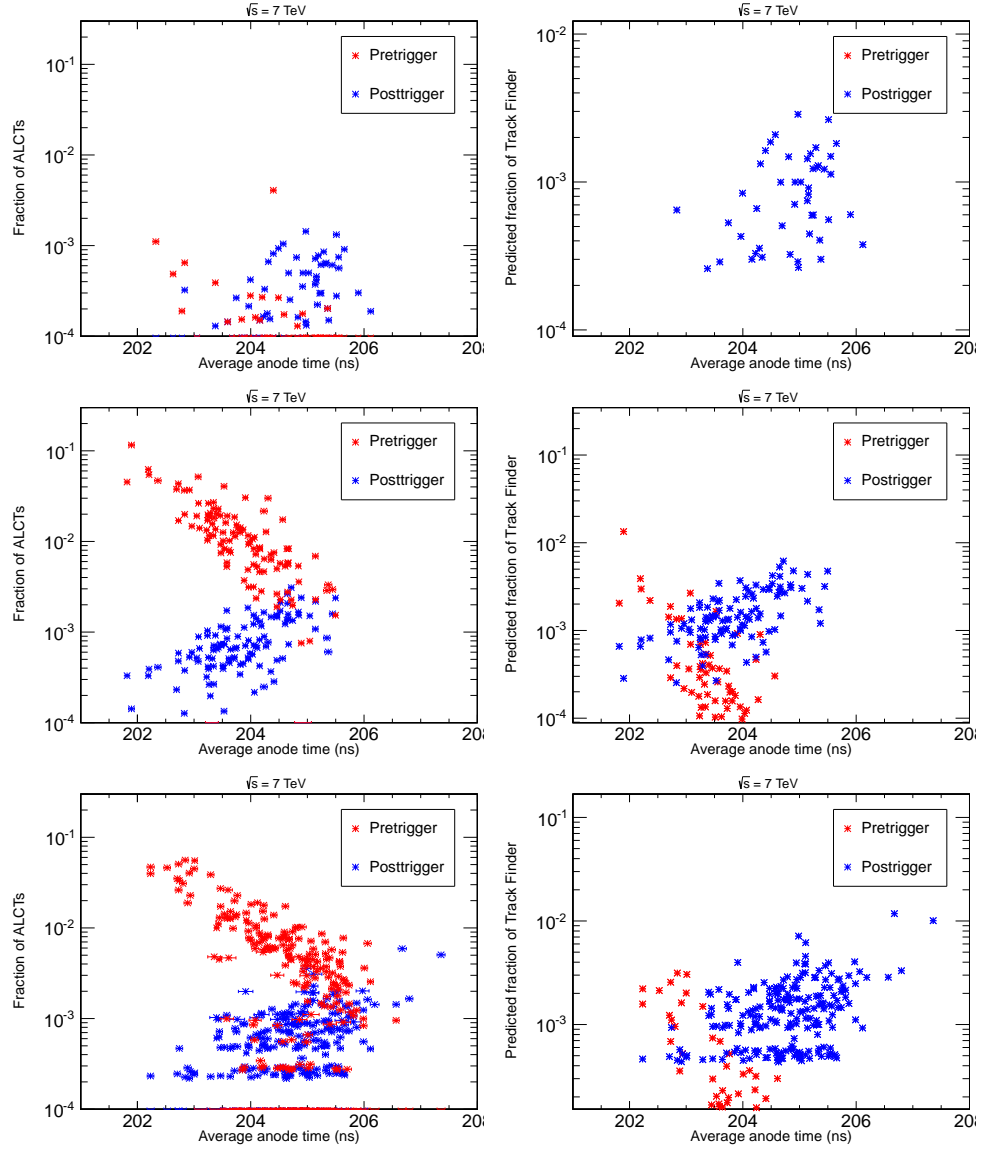
Figure 4.3: Pretriggering and posttriggering versus average anode time. Left column shows the pretriggering and posttriggering for LCTs. Right column shows what would be expected at the CSCTF. Top row for chambers in the innermost ring and station. Middle row is for all other chambers in the innermost ring. Last row is for all other chambers.
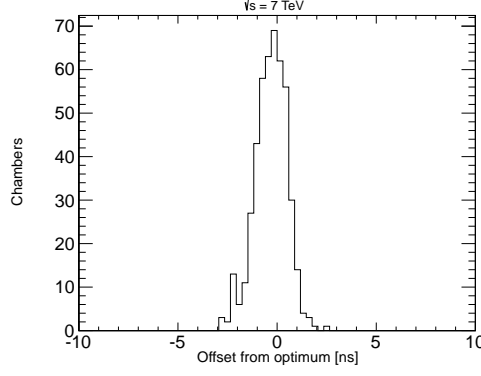
Figure 4.4: Average anode time of chambers relative to optimal values.

the actual number possibly being different chamber to chamber. Shifting the offsets is a somewhat complicated procedure and carries the risk of accidentally shifting the timing of a chamber by a large amount. Thus, the offsets are changed only when deemed necessary, numerous iterations to get a perfect synchronization are not done. The synchronization with respect to the optimal values for all chambers is shown in Fig. 4.4, most of the chambers are within one ns of the optimal time with none more than three ns off.

After this synchronization procedure is performed the timing of the LCTs is very good. This can be seen in Fig. 4.5 which shows the bunch crossing window assigned to LCT matched to high quality muons. The distribution is purposefully made asymmetric to account for the CSCTF logic used further downstream. The efficiency is 99%, better than the 92% design requirement.

4.5 Muon Track Timing

Tracks, meant to represent muons or other particles passing through the detector, are built in the muon system connecting together the hits in the different cham-
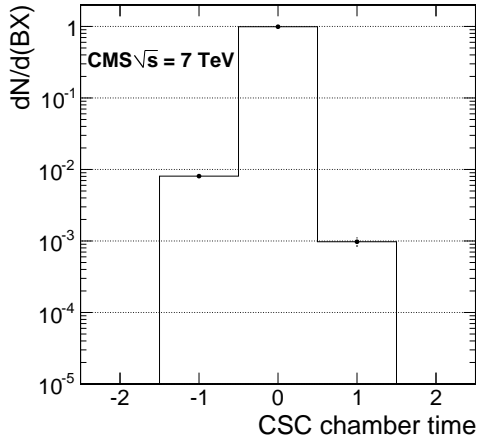
Figure 4.5: Fraction of LCTs versus LCT bunch cross assignment relative to collision event

bers of the CSCs, DTs, and RPCs. Numerous different timing quantities about the track are calculated under three different assumptions on how the particle travels between the interaction point and the muon system. Only time measurements from the CSCs and DTs are used to calculate the timing quantities.

A particle of speed, v, travelling from the interaction point, will arrive at a location d in the muon system at

$$t = d/v + t_0 \tag{4.1}$$

where t_0 is an overall offset. When the local timing variables were defined, they were calibrated such that a speed of light, c, particle would have an average time of zero. Thus d/c has already been subtracted from the times so the same quantity must be subtracted from the right hand side of 4.1. Additionally it is easier to work with β^{-1} ($\equiv c/v$) instead of v. With these two ideas taken into

33

mind Eq. 4.1 now becomes

$$t = d/v - d/c + t_0$$
$$t = d \times \beta^{-1}/c - d/c + t_0 \quad (4.2)$$
$$t = (d/c) \times (\beta^{-1} - 1) + t_0$$

The three assumptions relate to how the β^{-1} and t_0 parameters are fixed and produce three different variables. The formula has two pieces of input datum, time, t, and distance, d. The distance from the interaction point to the hit location is known to a much better degree than the time of the hit so the uncertainty on the variables comes almost entirely from the time measurement.

The first variable is the speed of the particle assuming it left the origin at $t_0 = 0$ reducing Eq. 4.1 to $t = (d/c) \times (\beta^{-1} - 1)$ or simpler $\beta^{-1} = tc/d + 1$. The measurement of β^{-1} comes from averaging this quantity for all the CSC and DT hits associated with the track weighted as one over their variance. Outlier hits from anode hits are again cleaned in the same manner as per the segment times. The weighting by one over variance and outlier cleaning is performed for all three measurements.

The motivation for using β^{-1} now becomes clear, the β^{-1} measurement is linear with t, the source of the largest uncertainty. This means that β^{-1} will have a much more normal shape than β which would be skewed. An important point here is that the distribution will be close to symmetrical for speed of light muons coming from the LHC.

The uncertainty on β^{-1} can be calculated according to the formula

$$\sigma_{1/\beta} = \sqrt{\sum_{i=1}^{N} \frac{(1/\beta_i - \overline{1/\beta})^2 \times w_i}{N-1}}, \quad (4.3)$$

where $\overline{1/\beta}$ is the average β^{-1} of the track, w_i is the weight of the ith hit, and N is the number of measurements associated with the track.
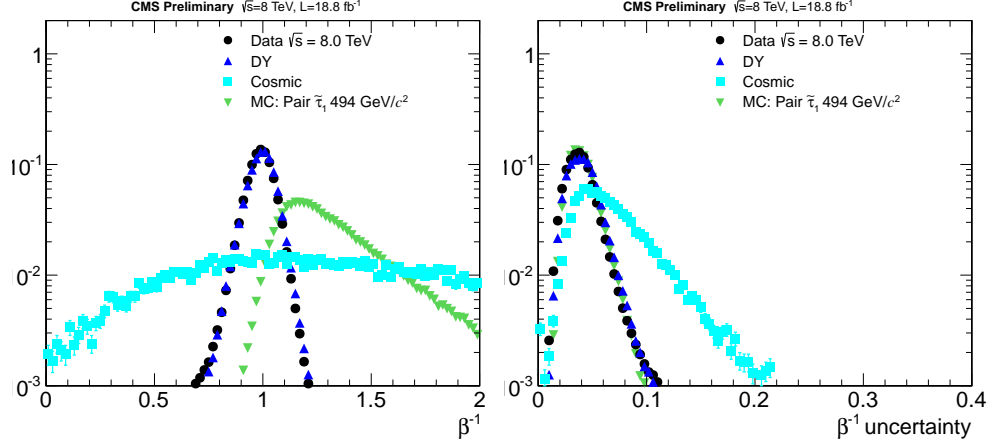
Figure 4.6: Distribution of β^{-1} and the uncertainty on β^{-1} for data, simulated Drell-Yan production of photons and Z boson decaying to muons (DY), muons from cosmic rays, and simulated HSCPs

The speed of the particle is very useful in separating standard model muons from HSCP produced in new physics as is shown in Section 5. Figure 4.6 shows the β^{-1} measurement and its uncertainty for: data, completely dominated by collision muons; muons from the simulated Drell-Yan production of Z bosons and photons; cosmic ray muons, the sample is defined in 5; and HSCPs, again the sample is defined in 5. It can be seen that the data is strongly peaked at one, the cosmic ray muons are roughly flat, while the HSCP have β^{-1} greater than one, indicating they are traveling slowly.

The next variable, time at vertex, is the estimated time the particle left the interaction point assuming it traveled at the speed of light. This means setting β^{-1} to be one in 4.1 reducing the equation to simply $t = t_0$. For muons with at least a modest amount of p_T that are produced in a collision in the triggered bunch crossing window this assumption is valid and thus the value should be centered at zero. Figure 4.7 shows the time at vertex for the same three samples
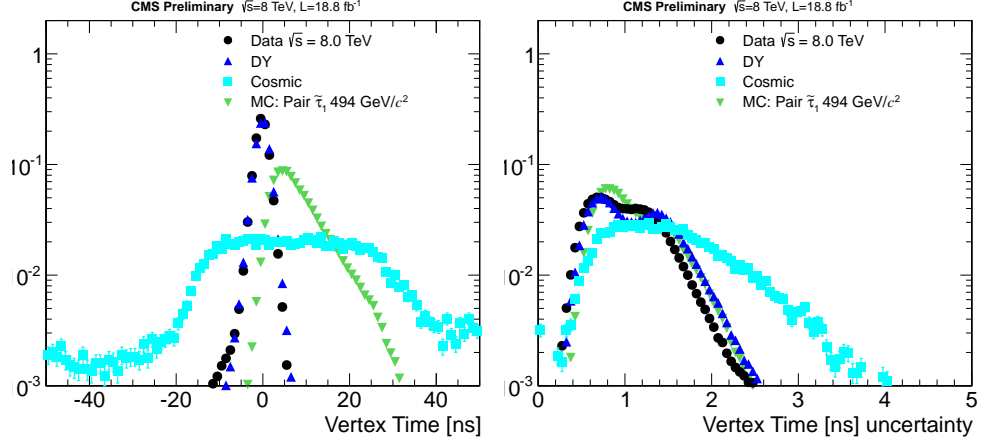
Figure 4.7: Distribution of time at vertex and the uncertainty on time at vertex for data, simulated Drell-Yan production of photons and Z boson decaying to muons (DY), muons from cosmic rays, and simulated HSCPs

as in 4.6.

The last variable, time at vertex out in, is similar but it assumes the particle is traveling into CMS, such that the parameter t_0 represents the time an incoming particle would have crossed the interaction point. This can be an interesting property because tracks can be found in the inner tracker within a small time window so an incoming cosmic reconstructed in the inner tracker would likely have a t_0 from this measurement near zero. The measurement assumes $\beta^{-1} = $ -1 reducing 4.1 to $t = -2(d/c) + t_0$ which can be written to $t_0 = -2(d/c) + t$ which makes it clear that t_0 can be found as the average of this quantity with weights like the previous measurement. Figure 4.8 shows the distribution of this time for the same three samples as above.

The question may be asked why not to make a measurement without making any assumptions on t_0 or β^{-1}. This was checked but it was found to have resolution worse by more than an order of magnitude and very little discrimanatory
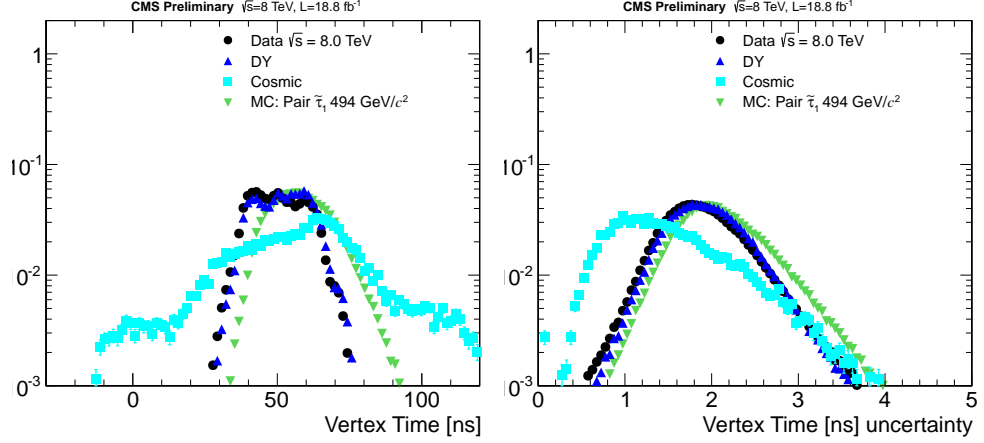
Figure 4.8: Distribution of time at vertex out in and the uncertainty on time at vertex out in for data, simulated Drell-Yan production of photons and Z boson decaying to muons (DY), muons from cosmic rays, and simulated HSCPs

power. This is because the assumptions in the previous measurements allowed all of them to use information related to the beam spot, which is approximately three times as far away from the innermost part of the muon system as the outermost part is to the innermost part. The last two measurements both assumed an error free propagation of the time in the muon system to the interaction point while the β^{-1} measurement added a new point at the interaction point with t = 0. This assumption free measurement is not used for any purpose in CMS.

CHAPTER 5

Searches for Heavy Stable Charged Particles

5.1 Foreword

The contents of this chapter are included in a paper authored by the CMS collaboration that is currently in the process of being submitted to a journal. The paper includes five searches for HSCPs in data collected by CMS during 2011 running at $\sqrt{s} = 7$ TeV and 2012 running at 8 TeV. Each search is designed to have sensitivity for various different signatures of HSCP. The work was done in a small group within the CMS collaboration with myself being one of the central analyzers. The five searches are all done in the same framework so most of my work was applied to all five analyses. The five searches are labelled *muon only*, *muon+track*, *track only*, *multiple charge*, and *fractional charge*.

For parts of the searches that were different between the five searches, I was essentially the only person to work on the *muon only* analysis and contributed largely to the *muon+track* analysis. I worked on the *track only* and *multiple charge* searches to a slightly smaller degree. My work on the *fractional charge* search was mostly limited to work that was applied across all five searches. Therefore this chapter mostly focuses on the *muon only* and *muon+track* searches, the *track only* and *multiple charge* searches are presented as well with the specific parts that I worked on highlighted. The *fractional charge* search is not presented here.

The journal paper includes both the 2011 and 2012 data taking periods for all

the analyses except for the *muon only* analysis which only uses the 2012 data. As the *muon only* analysis is the major focus of this chapter it was decided to focus on the data collected in 2012 for this chapter. Additionally, the 2012 data was taken at a higher energy and includes approximately four times the integrated luminosity so the sensitivity of the searches is to a large degree determined by the data collected in 2012. The procedure for analyzing the data from the two periods is identical. A statistical combination of the 2011 and 2012 data for all the analyses except for *muon only* is preseneted at the end of the chapter.

5.2 Introduction

As discussed in section 2.3 new heavy long-lived charged particles are predicted in many extensions to the SM. HSCPs with lifetimes $\gtrsim$ 40ns are likely to traverse the entire CMS detector before decaying and will thus be directly detectable. Some of the HSCP combine with SM particles to form composite objects that can be electrically charged or neutral. Interactions with the detector may change the SM constituents of the particles and through this their electric charge. The HSCPs will be produced with high momentum but their large mass means that a majority will have a velocity, $\beta \equiv v/c$, less than 0.9. As no heavy long-lived particles are present in the SM, HSCPs would be the only high momentum particles produced at the LHC with β not very close to one. Detector signatures unique to slow moving particles are exploited to search for HSCP. The backgrounds to the search are SM particles with detector mismeasurement and in some cases muons coming from cosmic rays.

Previous collider searches for HSCPs have been performed at LEP [16, 17, 18, 19], HERA [20], the Tevatron [21, 22, 23, 24], and the LHC [25, 26, 27, 28, 29, 30, 31, 32]. The results from such searches have placed important bounds on beyond

the standard model (BSM) theories [33, 34], such as lower limits on the mass of gluinos, scalar top quarks (stops), and pair produced scalar τ leptons (staus) at 1098, 737, and 223 GeV/c^2, respectively.

Four different searches are presented here, one requires only that a track be found in the muon system, this is referred to as the *muon only* analysis. This analysis is expected to still have sensitivity when all particles are produced electrically neutral. The second requires that the muon system track be matched to a track in the inner tracker, referred to as the *muon+track* analysis. This analysis is especially powerful for lepton like HSCP. The third is the *track only* analysis that only requires a track be found in the inner tracker so that it can be sensitive to particles becoming neutral in the calorimeter and leaving no hits in the muon system. The last analysis looks for particles with $Q > 1e$ reconstructed like in the *muon+track* analysis and is referred to as the *multiple charge* analysis.

For all plots in this chapter, the first and last bins contain the underflow and overflow, respectively.

5.3 Samples

Data collected with the CMS detector during 2012 running at an energy of $\sqrt{s} = 8$ TeV are searched. The data collection was split into four periods labeled A, B, C, and D. All data collected by CMS unundergo a prompt reconstruction as described in section 3.3.2. The first two run periods, A and B, underwent an additional rereconstruction so as to have the latest reconstruction improvements and calibration constants. The rereconstructed samples are used for the A and B periods while the promptly reconstructed samples are used for the C and D periods.

CMS has a Data Certification team which checks all data collected and certifies the data as good for analysis. The certification requires all detector subsystems to be operating at full ability, or at least close enough to full ability to not have a detrimental effect on offline analyses. Additionally, higher level objects such as muons and electrons are checked to make sure the data are good for physics analyses. For this particular analysis, the RPC trigger plays an important role, as discussed in section 5.4, and so the RPC is required to be included in the L1 trigger for all data searched. This leads to the searches using slightly less data than most other CMS analyses on 2012 data. The data sample used by this analysis corresponds to $18.8 fb^{-1}$.

Multiple different signal Monte Carlo (MC) simulation samples are produced to account for the multiple different signatures an HSCP could have, more detail on the signal models can be found in Sec. 2.3.

Pair production of gluino and stop samples are produced with masses in the range 300–1500 GeV and 100–1000 GeV, respectively. The gluinos are generated in the split SUSY scenario [35, 36]. under the assumption of high squark masses of 10 TeV. The samples are generated using PYTHIAv8.153 [37]. Samples are produced with the fraction f of gluinos forming glue ball $R - hadrons$ set to $f = 1.0, 0.5$, and 0.1. The value of $f = 1.0$ results in all gluino $R - hadrons$ being produced neutral. The samples are also produced with two different modellings of a nuclear interaction of R-hadrons with matter, the cloud interaction and charge suppressed models. The charge suppressed model results in all $R - hadrons$ being neutral after a nuclear interaction. The cloud interaction model should be assumed for samples unless explicitly stated otherwise. Most HSCP will not have a nuclear interaction while passing through the CMS tracker, however almost all of them will have an interaction in the calorimeter.

The above effects can lead to many interesting signatures in the CMS detector. R-hadrons neutral after hadronization will generally remain neutral through the tracker but may gain charge in the calorimeter under the cloud model and leave hits in the muon system. If the glue ball fraction is 1.0, then this would be the only way to detect gluino HSCP. The *muon only* analysis is designed to have sensitivity to HSCP of this type. On the other hand HSCP produced charged under the charge suppression model will likely be charged in the tracker but always neutral in the muon system. The *track only* analysis is designed to be sensitive to HSCP of this type. A third signature is an HSCP charged in both the muon and tracker systems which would have a signature similar to a muon. HSCP produced neutral under the charge suppression model would never be charged during their passage through CMS and thus are outside the scope of an HSCP search.

The p_T, β, and η distributions of gluino and stop particles at generation are shown in Figs. 5.1 and 5.2, respectively.

Additional samples are produced creating lepton-like HSCP. Pair production of stau samples are produced under the minimal gauge mediated symmetry breaking (mGMSB) scenario [12] using the SPS7 slope [38]. The ISASUGRA version 7.69 [39] program is used to set the particle mass scale and decay table. The program fixes a number of mGMSB parameters. The number of messenger particles is set to to three, $tan\beta = 10$ (β used differently than for speed above), $\mu > 0$, $C_{Grav} > 10000$, and $M_{Mes}/\Lambda = 2$. The high value of C_{Grav} results in the stau being long-lived while varying Λ from 31 to 160 TeV gives staus within a mass range of 100–494 GeV. The produced mass spectrum and decay table are passed to PYTHIAv6.426 [40]. Stau production proceeds either by direct electroweak production or from the cascade decay of other particles (usually through the pair production of gluinos and squarks). Cascade decay is dominant due to
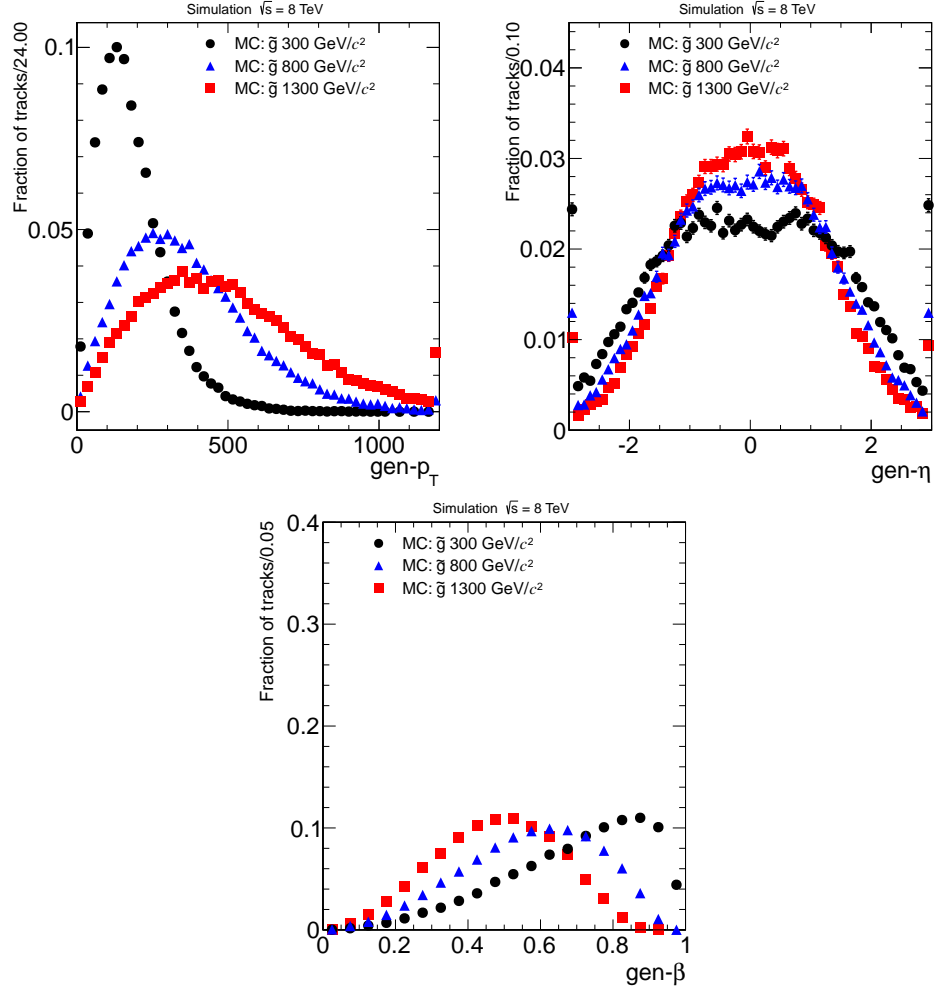
Figure 5.1: Distribution of various kinematic variables for various gluino samples at generation. Top: p_T (left) and η (right). Bottom: β
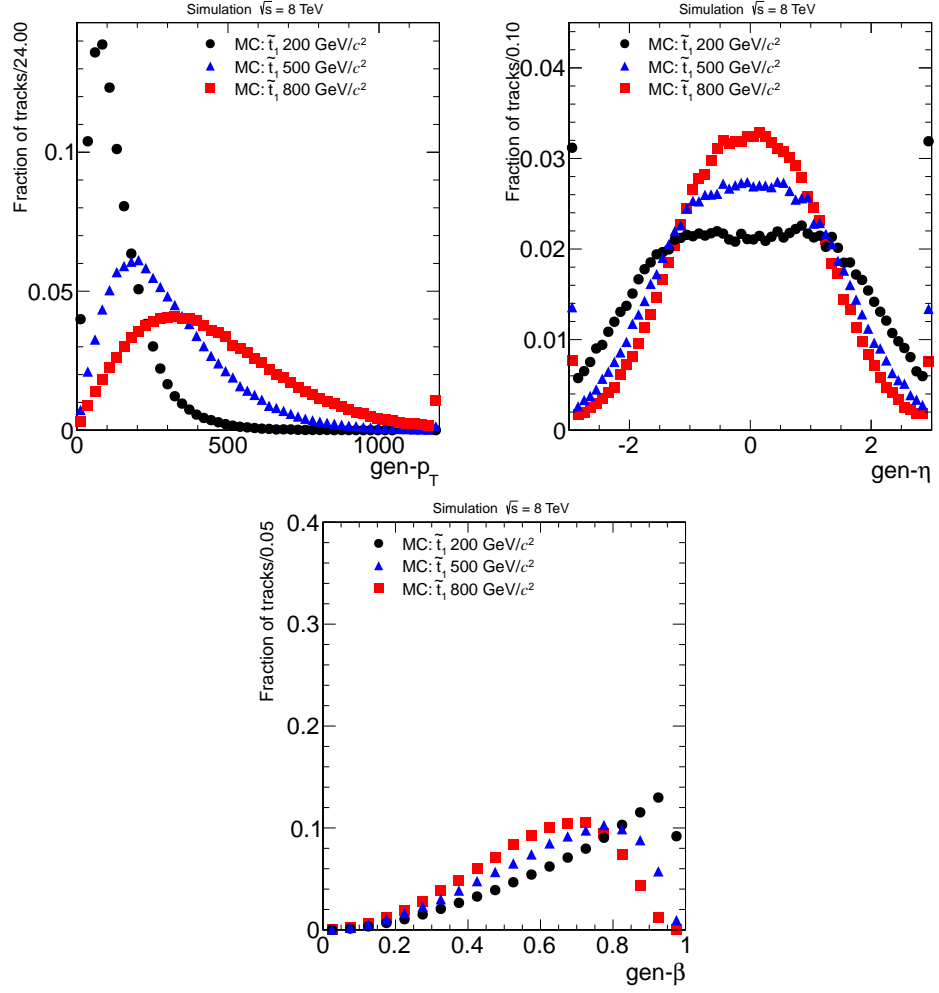
Figure 5.2: Distribution of various kinematic variables for various stop samples at generation. Top: p_T (left) and η (right). Bottom: β

the strong nature of the production mechanism. In order to give the best results while maintaining model independence two stau samples are used. One using all production mechanisms (GMSB) and one with staus only produced through direct production (PP). The second sample is less dependent on the model parameters. The distribution of p_T, η, and β at generation are shown in Figs 5.3 and 5.4 for various GMSB and PP stau samples, respectively.

The last of the signal samples used is modified Drell-Yan production of long-lived leptons with different electrical charges. As all SM particles that reach CMS have electrical charge, Q, equal to $\pm 1e$ or are neutral, the possbility of HSCPs with non-unit charge is interesting. The production of these particles is simulated with PYTHIAv6.426 [40]. Samples are produced with charge Q = 1e, 2e, 3e, 4e, 5e, 6e, 7e, and 8e for masses of 100-1000 GeV for $1e <= Q <= 5e$ and 200-1000 GeV for $Q > 5e$. The distribution of p_T, η, and β at generation for various charges and masses are shown in Fig. 5.5.

All MC simulation events are overlaid with additional proton-proton collisions, see Section 3.2. Weights are given to the events so that the distribution of additional collisions in the MC simulation samples matches what is observed in data. After this reweighting there is a good agreement in the number of primary vartices, a proxy for the number of collisions, between data and MC simulation as seen in Figure 5.3

5.4 Trigger

All events used in the analyses are required to be triggered by one of three algorithms. The algorithms require a high momentum track to be found online and/or missing transverse energy, PFMET, as calculated by the particle flow
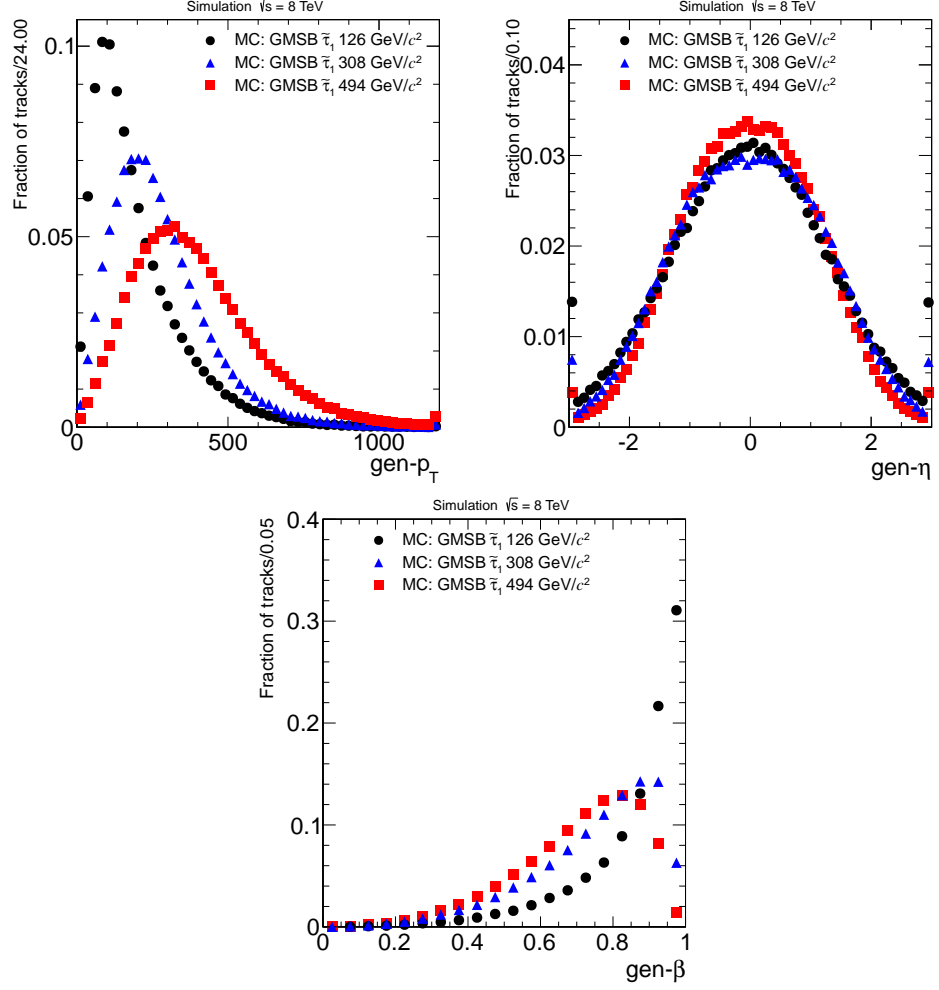
Figure 5.3: Distribution of various kinematic variables for various GMSB stau samples at generation. Top: p_T (left) and η (right). Bottom: β
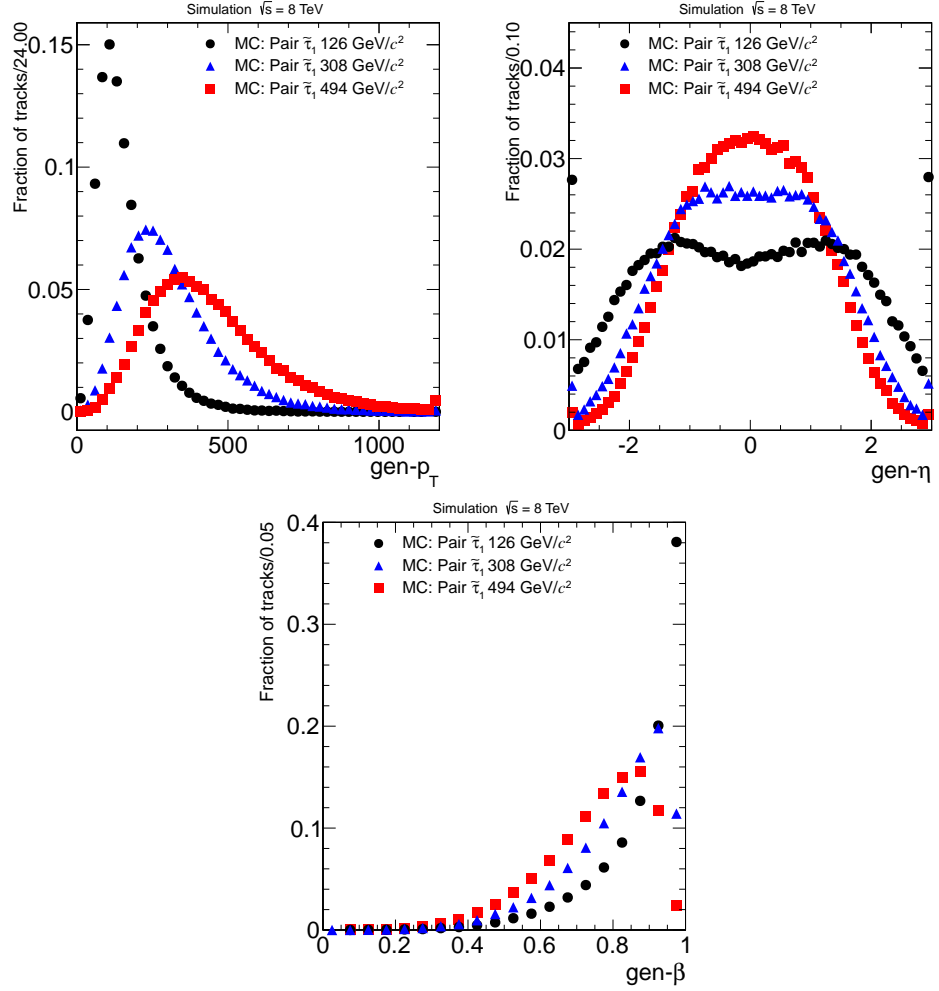
Figure 5.4: Distribution of various kinematic variables for various stau samples with only direct production at generation. Top: p_T (left) and η (right). Bottom: β
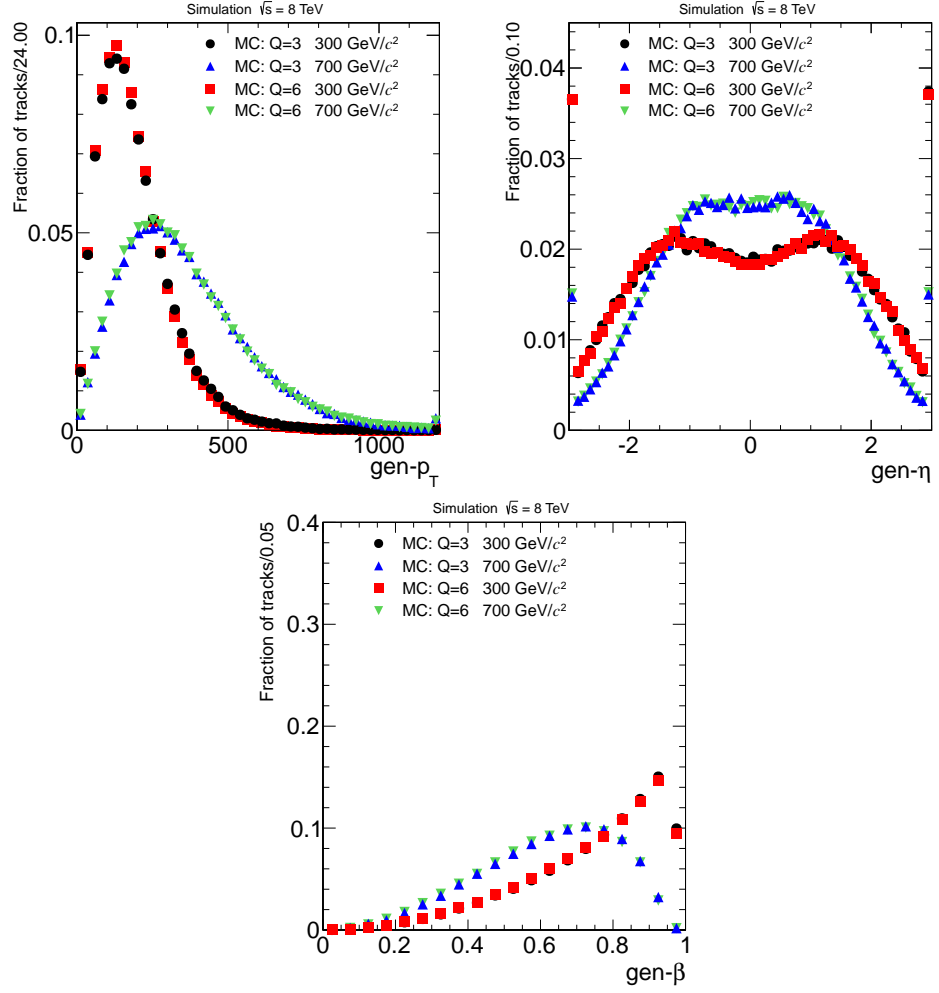
Figure 5.5: Distribution of various kinematic for modified DY samples with various charges and masses at generation. Top: p_T (left) and η (right). Bottom: β

Muon - Only $\sqrt{s} = 8$ TeV, L = 18.8 fb^{-1}

- ● Data $\sqrt{s} = 8.0$ TeV
- ▲ MC: $\tilde{g}$ 500 GeV/c^2
- ■ MC: $\tilde{t}_1$ 500 GeV/c^2
- ▼ MC: GMSB $\tilde{\tau}_1$ 494 GeV/c^2
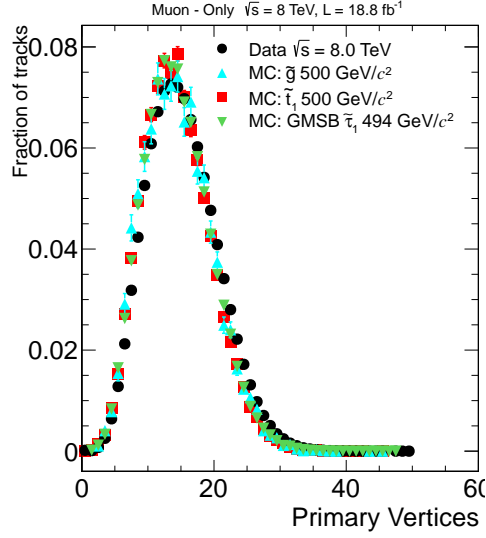
Distribution of number of primary vertices in data and various MC simulation samples

algorithm [41].

The particle flow algorithm attempts to reconstruct all particles in an event, then calculates PFMET as the magnitude of the negative vector sum of the transverse momentum of the particles. As the proton-proton collision occurs at rest in the transverse plane, PFMET is meant to represent the vector sum of all particles not found by the particle flow algorithm. For most CMS analyses, PFMET is created by either the limited detector response in finding all tracks in an event and determining their momentum or from neutral particles in the event which leave no signals in the detector. These neutral particles could be neutrinos from the SM or new neutral particles created in a BSM theory such as supersymmetry.

For HSCP, PFMET often arises because of details of the particle flow algorithm. The algorithm assumes SM particles and rejects tracks that do not conform to the properties expected of a SM particle. Two types of possible HSCP

49

tracks are rejected by the algorithm.

The first is tracks reconstructed only in the muon system. The only charged SM particles that are expected to reach the muon system are muons. As muons should have a matching track in the inner tracker, particle flow rejects tracks found only in the muon system. HSCP produced neutral then acquiring charge by interacting with the calorimeter would only have a track in the muon system and as such would not be included in the PFMET calculation.

The second is tracks produced charged but becoming neutral as they propagate through CMS. The particle flow algorithm rejects tracks reconstructed only in the inner tracker that have a track p_T much larger than the associated energy deposited in the calorimeter as this indicates the track has been misreconstructed. As an HSCP only deposits approximately 10 GeV of energy in the calorimeter and normally has > 100GeV of momentum, HSCP neutral in the muon system will likely be rejected.

These two effects lead to PFMET in HSCP events to be roughly equal to the vector sum of any HSCP neutral in either the muon system or the inner tracker, less however much energy they deposit in the calorimeter. This effect can be seen in Figures 5.6 and 5.7 which compare the di-HSCP system with online PFMET in events with at least 150 GeV of online PFMET.

One trigger issue unique to slow moving particles is the timing acceptance of the L1 trigger. If an HSCP arrives in the muon system too late it can trigger the readout of the wrong bunch crossing window. As most of the CMS subdetectors, though not the muon system, are designed to not readout data coming from adjacent bunch crossing windows, the data from the correct bunch crossing window would be lost. To help deal with this members of the CMS L1 trigger team developed a special configuration of the RPC L1 trigger to partially recover
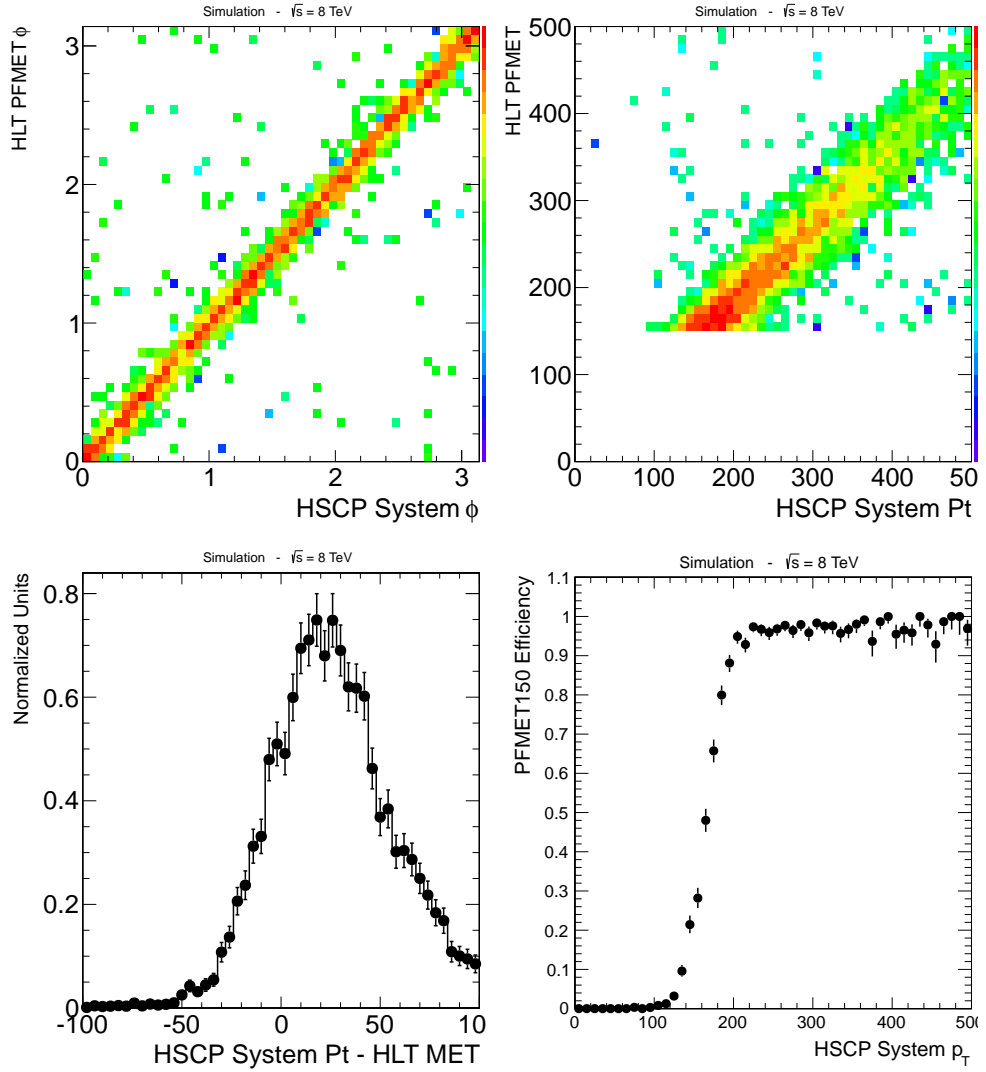
Figure 5.6: Comparison of di-HSCP system with online PFMET for a 1200 GeV Gluino $f = 1.0$ sample in events with at least 150 GeV of online PFMET. Top Left: Online PFMET ϕ versus di-HSCP system ϕ. Top Right: Online PFMET value versus di-HSCP system p_T. Bottom Left: Difference between di-HSCP system p_T and online PFMET value. Bottom Right: Probability to have online PFMET greater than 150 GeV versus di-HSCP system p_T.
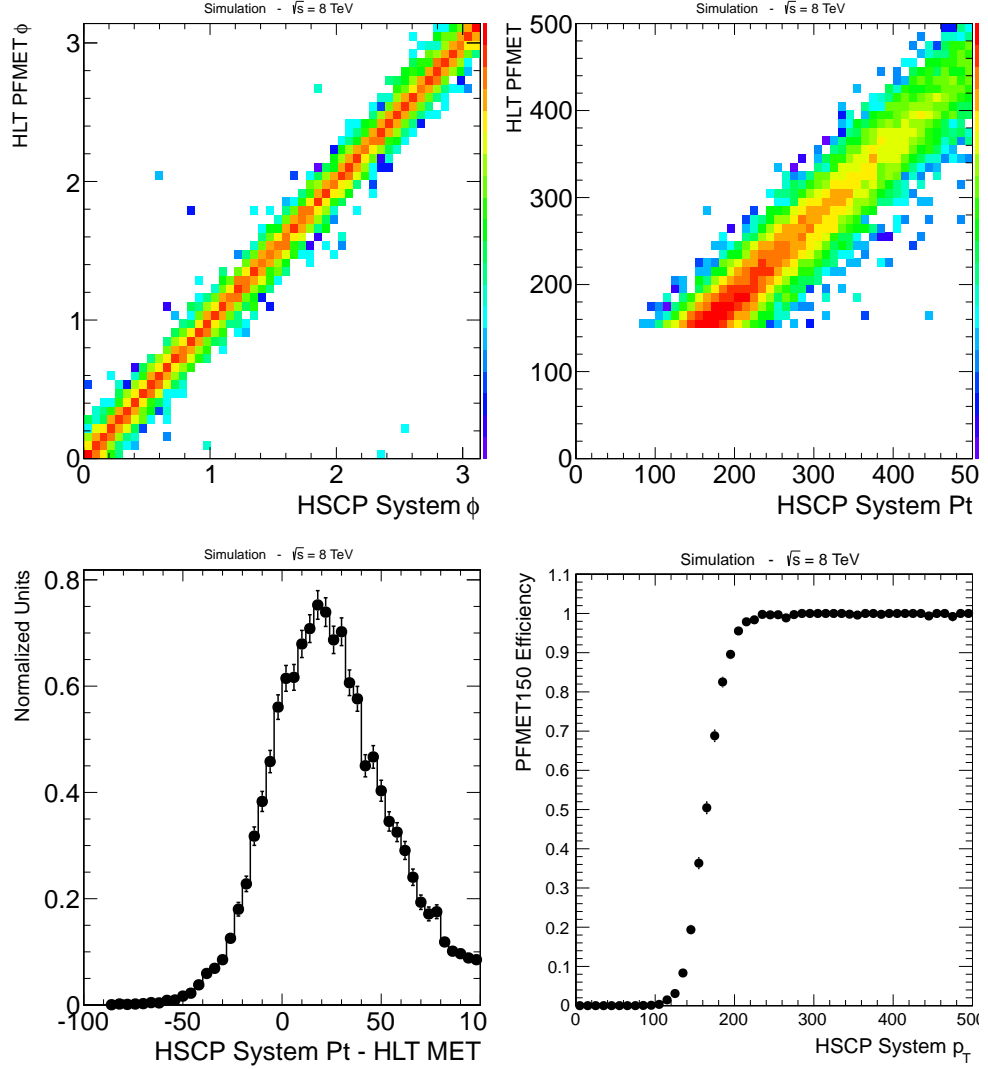
Figure 5.7: Same as Fig. 5.6 but the sample used is 1200 GeV $f = 0.1$ charge suppressed gluino.

HSCP that arrive in the muon system in the bunch crossing window following the crossing that produced them. This configuration is discussed in Sec. 3.3.2

The first of the three algorithms used requires both a track to be found in the muon system with $p_T > 70$ GeV, $|\eta| < 2.1$, with at least two muon stations associated with the track as well as PFMET > 55 GeV. For the first 700 pb^{-1} of 2012 running the threshold on PFMET was at 65 GeV. The signal samples are weighted to account for the amount of data taken at each threshold. Events collected with this trigger are only used in the *muon only* analysis. The second algorithm requires a track matched in both the inner tracker and muon system to be found by the HLT with $p_T > 40$ GeV and $|\eta| < 2.1$. The only requirement for the third algorithm is PFMET > 150 GeV. The second and third algorithms are used in all the analyses.

The decision to use the pure PFMET trigger even when a muon signature is required offline is prompted by the late arrival of the HSCPs in the muon system. Even with the RPC configuration described above, very slow moving HSCP can trigger the readout of the wrong event but still be reconstructed offline if the event has been triggered by the pure PFMET trigger. This can be seen in Figure 5.8 which shows the trigger efficiency versus β with and without the pure PFMET trigger. It can be seen that using the pure PFMET trigger allows the search to probe lower β particles.

When evaluating trigger efficiencies, it is important to only consider events that have a possibility of being selected offline. For the case of strongly charged HSCP this is made more difficult as some events may not have any $R - hadrons$ electrically charged while they pass through the detector. To deal with this, the trigger efficiencies are reported with respect to events where at least one HSCP is found offline. The efficiency for each trigger as well as the combined efficiency is
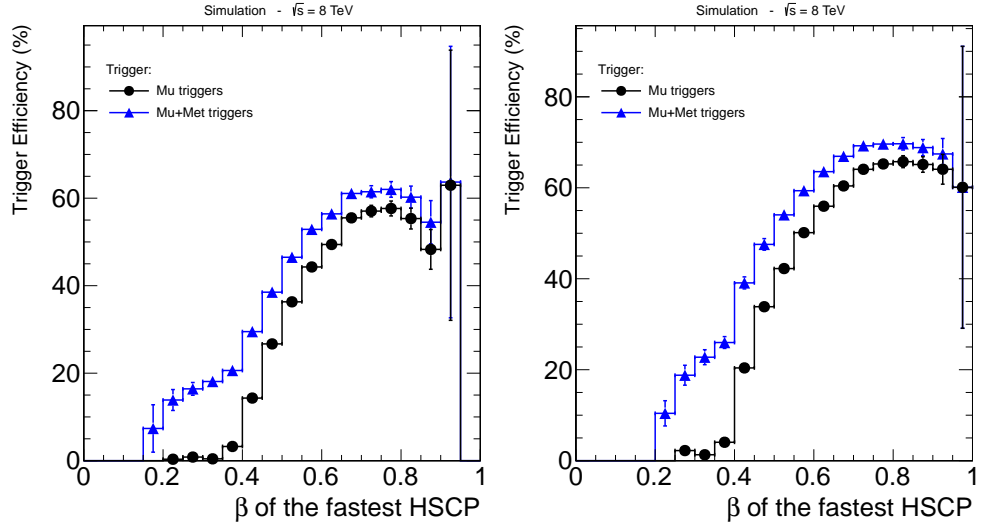
Figure 5.8: Trigger efficiency as a function of the β of the fastest HSCP reconstructed offline in the muon system with only the muon triggers and additionally including the PFMET trigger. Sample is 1200 GeV Gluino $f = 0.1$ (left) and 800 GeV stop (right)

Table 5.1: Trigger efficiency for various models considered using the SingleMu, PFMET, L2Mu+MET or a combination of the three. Efficiencies with respect to events with at least one HSCP reconstructed in the muon system.

Model	Mass (GeV)	Mu40	PFMET150	L2Mu+MET	Total
Gluino $f = 0.1$	400	35.55	19.41	34.28	58.56
Gluino $f = 0.1$	800	31.63	22.57	31.21	54.88
Gluino $f = 0.1$	1200	26.62	20.45	24.63	47.52
Gluino $f = 1.0$	400	5.55	23.22	36.63	46.07
Gluino $f = 1.0$	800	5.01	24.50	31.88	43.41
Gluino $f = 1.0$	1200	3.69	20.62	23.62	35.45
Stop	200	42.79	11.15	27.31	58.80
Stop	500	42.07	19.79	31.13	61.21
Stop	800	41.57	21.57	30.33	60.73

listed for various signals in Tables 5.1 and 5.2 in events with at least one HSCP reconstructed in the muon system and muon system plus tracker, respectively.

Muons from cosmic rays are an important background for the *muon only* analysis. To study and predict them a trigger that selects events when no beams are passing through CMS is used. The trigger requires the presence of a muon system track with $p_T > 20$GeV, no proton bunches passing through CMS within 50ns, and for the event not to be flagged as noise from the LHC beams. The muon system track reconstruction used for the cosmic ray muon trigger is slightly different than for the collision trigger as it is not updated at vertex, the meaning of this is discussed in section 5.6. However, both reconstructions are required offline so no bias is introduced.

Table 5.2: Trigger efficiency for various models considered using the SingleMu, PFMET, or a combination of the two. Efficiencies with respect to events with at least one HSCP reconstructed in both the muon system and inner tracker.

Model	Mass (GeV)	Mu40	PFMET150	Total
Gluino $f = 0.1$	400	51.87	16.06	59.09
Gluino $f = 0.1$	800	46.50	20.50	56.42
Gluino $f = 0.1$	1200	38.96	19.56	49.95
Gluino $f = 1.0$	400	41.81	19.36	51.76
Gluino $f = 1.0$	800	37.83	21.57	49.01
Gluino $f = 1.0$	1200	31.70	21.16	45.21
Stop	200	58.43	7.69	61.54
Stop	500	56.91	17.40	64.44
Stop	800	56.15	20.49	65.59
GMSB Stau	100	97.86	14.74	98.06
GMSB Stau	308	97.03	17.53	97.47
GMSB Stau	494	95.56	17.76	96.35
PP Stau	100	95.06	0.17	95.09
PP Stau	200	95.78	0.37	95.82
PP Stau	494	95.23	1.16	95.36

5.5 Selection Variables

The low velocity of HSCPs lead to two interesting detector signatures. The first is that the particles will arrive at the detector elements later than SM particles will. The muon system, being the furthest detector element from the interaction point, has the largest timing difference. The measurement of the arrival time of particles in the muon system is discussed in Ch. 4. The β^{-1} variable is used in the searches to discriminate between HSCPs and SM particles.

The second signature is the amount of ionization energy loss HSCP have in the inner tracker. The amount of the ionization energy lost per unit length, dE/dx, is dependent on both the velocity of the HSCP and its charge as described by the Bethe-Bloch formula [42]. The dependence of dE/dx on charge goes as Q^2, meaning that even a $Q = 2e$ HSCP will have four times as much energy loss as a SM particle. The dependence on speed for particles with $0.1 < \beta < 1$, goes as $\sim 1/\beta^2$. SM particles with momentum 10-1000 GeV will all have roughly the same dE/dx, ($\approx$ 3MeV/cm) and are often referred to as minimum ionizing particles (MIPs).

As in [30], two variables related to dE/dx are calculated for each track. The first is I_h which is an estimator of the dE/dx of the track. The second is I_{as} which is a modified version of the Smirnov-Cramer-von Mises [43, 44] discrimant that checks the probability that a MIP would produce a charge less than or equal to the charge of each of the hits along the track. The discrimant peaks at zero for MIPs and approaches one for high-ionizing particles.

An estimate of the mass m, assuming Q=1e, of a particle can be made from I_h and the momentum p of a track. This is done by using Eq. 5.1, also from Ref. [30],

$$I_h = K\frac{m^2}{p^2} + C. \tag{5.1}$$

with $K = 2.559 \pm 0.001$ MeV cm^{-1} c^2 and $C = 2.772 \pm 0.001$ MeV cm^{-1}.

The last selection variable used in the analyses is transverse momentum. HSCP would be produced by BSM theories that have a high energy scale, leading to the HSCP to be produced with much more momentum than is typical for SM particles.

The *muon only* analysis uses the p_T measurement coming from the muon system while the rest of the analyses use the measurement from the inner tracker. $R - hadrons$ are unlikely to undergo a nuclear interaction while traversing the tracker so they would have the same electric charge at all points in the tracker. While passing through the muon system however, R-hadrons will often undergo a nuclear interaction with the steel return yoke located between the muon stations possibly causing the electric charge to change in the middle of the muon system. This behavior affects the reconstruction of the HSCP track.

CMS measures the curvature of a track which can then be used to determine the Q/p_T of the track. A charge of $Q = 1e$ is assumed in order to determine the p_T of the track. For $R - hadrons$ that can change their charge inside of CMS it can be the case that the average value of Q during its passage through the muon system does not equal one. This effect has different consequences for the stop and gluino samples.

A stop particle, specifically not an anti-stop, has a charge of $+(2/3)e$ and forms a R-hadron with either an anti-quark ($\tilde{t}\bar{q}$) or two quarks ($\tilde{t}qq$). Anti-quarks have a charge of $-(2/3)e$ or $+(1/3)e$ leading to R-hadrons with a charge of either 0 or $+1e$. Quarks have a charge of either $+(2/3)e$ or $-(1/3)e$ which allows for

the creation of R-hadrons with a charge of 0, +1e, or +2e. Thus a stop R-hadron will always have a positive charge or be neutral. For an anti-stop, the effect is reversed and the R-hadron will always have a negative charge or be neutral.

For gluino $R - hadrons$ this statement does not hold true. Gluinos can hadronize into glue balls ($\tilde{g}g$), R-mesons ($\tilde{g}q\bar{q}$), or R-baryons with either quarks or anti-quarks ($\tilde{g}qqq$ or $\tilde{g}\bar{q}\bar{q}\bar{q}$), allowing the charge of the R-hadron to range from $-2e$ to $+2e$. This leads to the average charge of the R-hadron as it traverses the muon system to often be less than $1e$ and the p_T value to be overestimated.

To observe this effect the function $\Delta(Q/p_T)$ is defined in Equation 5.2

$$\Delta(Q/p_T) = ((Q/p_T)_{Muon} - (Q/p_T)_{Inner})/(Q/p_T)_{Inner} \qquad (5.2)$$

where Muon refers to muon system track qualities and Inner refers to inner track qualities. As the p_T resolution in the tracker is an order of magnitude better than in the muon system, it is a sufficiently good approximation of the true particle momentum. Figure 5.9 shows the distribution of $\Delta(Q/p_T)$ for tracks with inner track $p_T > 200$ GeV for data and various HSCP signal samples. A value of zero in this plot indicates the p_T was reconstructed correctly while negative one indicates the reconstructed p_T approaches infinity. The GMSB stau sample, which does not change charge, has a distribution similar to data, though slightly wider. The slight discontinuity at negative one is due to particularities of the reconstruction but only affects a small number of tracks. The stop sample, which is not able to flip charge but merely to switch between one sign and zero, is centered at zero but with a slightly wider width than data or GMSB stau. The gluino sample, which can flip charge, is centered closer to negative one meaning that their reconstructed p_T is normally larger than what is generated, sometimes to a very large degree. This effect causes further discrimination of gluino HSCP

59
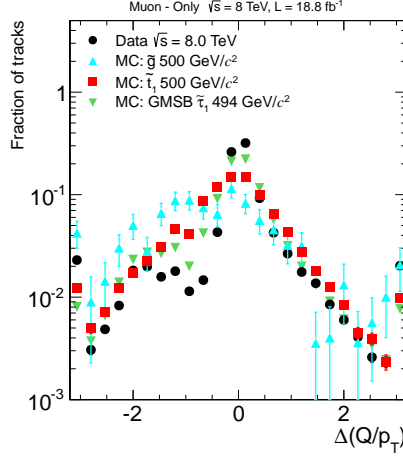
Figure 5.9: Distribution of $\Delta(Q/p_T)$ for data, 500 GeV gluino, 500 GeV stop, and 494 GeV GMSB stau.

from background Standard Model particles.

For the lepton like samples with non-unit charge, the p_T will be mismeasured by a factor of $1/Q$, meaning multiply charged particles will have their p_T underestimated This effect can be seen in Figure 5.10.

5.6   Preselection

Candidates for the *muon only* analysis are tracks reconstructed in the muon system. Candidates for the *muon+track* and *multiple charge* analyses are tracks found in both the muon system and the inner tracker. The *track only* analysis requires only that the tracks be found in the inner tracker. Various requirements are applied to the candidate in order to reduce tracks from background process while maintaining good efficiency for HSCP.
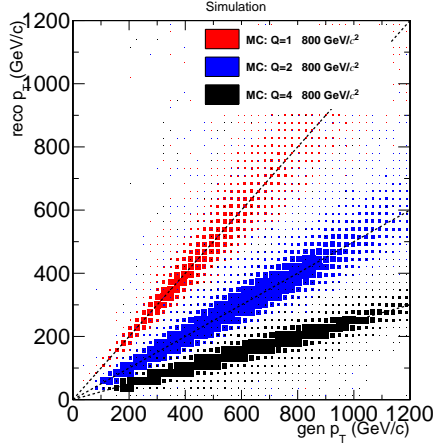
Figure 5.10: Distribution of reconstructed p_T versus generator p_T for Q=1e, 2e, and 4e samples.

5.6.1 Preselection for *muon only*

The *muon only* analysis requires the candidates to have $p_T > 80$, $|\eta| < 2.1$, and valid DT or CSC hits in at least two muon stations to reinforce the requirements applied at trigger level. The distributions of η and number of muon stations is shown in Fig. 5.11 for data, the cosmic ray muon control sample, and signal MC. The discontinuities in the η distribution are due to interfaces between the detector elements in the muon system.

Quality cuts on the β^{-1} measurement are applied. The measurement must have at least eight degrees of freedom and the uncertainty must be less than 0.07. Additionally the candidate must have β^{-1} greater than one. A potential background source is muons coming from bunch crossing windows in adjacent beam crossings. Candidates are required to have a measured time at vertex not be within 5ns of an expected adjacent collision. Figure 5.12 shows the distribution of these quantities for data, cosmic ray muon control sample, and signal MC.
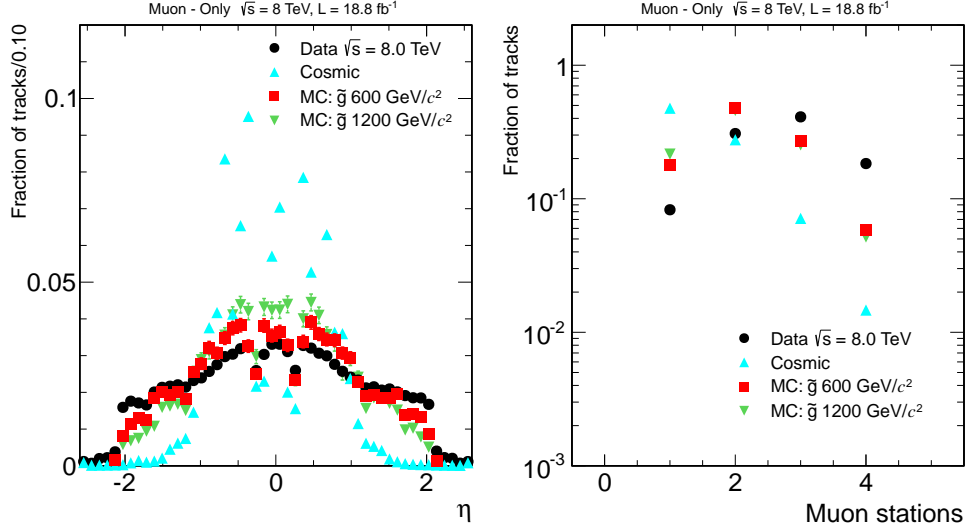
Figure 5.11: Distribution of η (left) and number of matched muon stations (right) for data, cosmic ray muon control sample, and signal MC in the *muon only* analysis.

Additional cuts are used to control the background from cosmic ray muons. The displacement of the track with respect to the beam spot is required to be less than 15cm in both the longitudinal and transverse direction relative to the beam line. The candidate $|\phi|$ must not be within 1.2–1.9 radians, this region represents tracks pointing in the vertical direction, as is expected of cosmic ray muons. Cosmic ray muons travel through the top and bottom halves of the detector leaving hits in the muon system opposite of the candidate. Thus, it is required that there be no muon segments with η within 0.1 of $-\eta_{candidate}$. Only segments separated from the candidate by at least 0.5 in ϕ are used to prevent candidates in the central portion of the detector to match to their own segments. Figure 5.13 shows the distribution of these quantities.
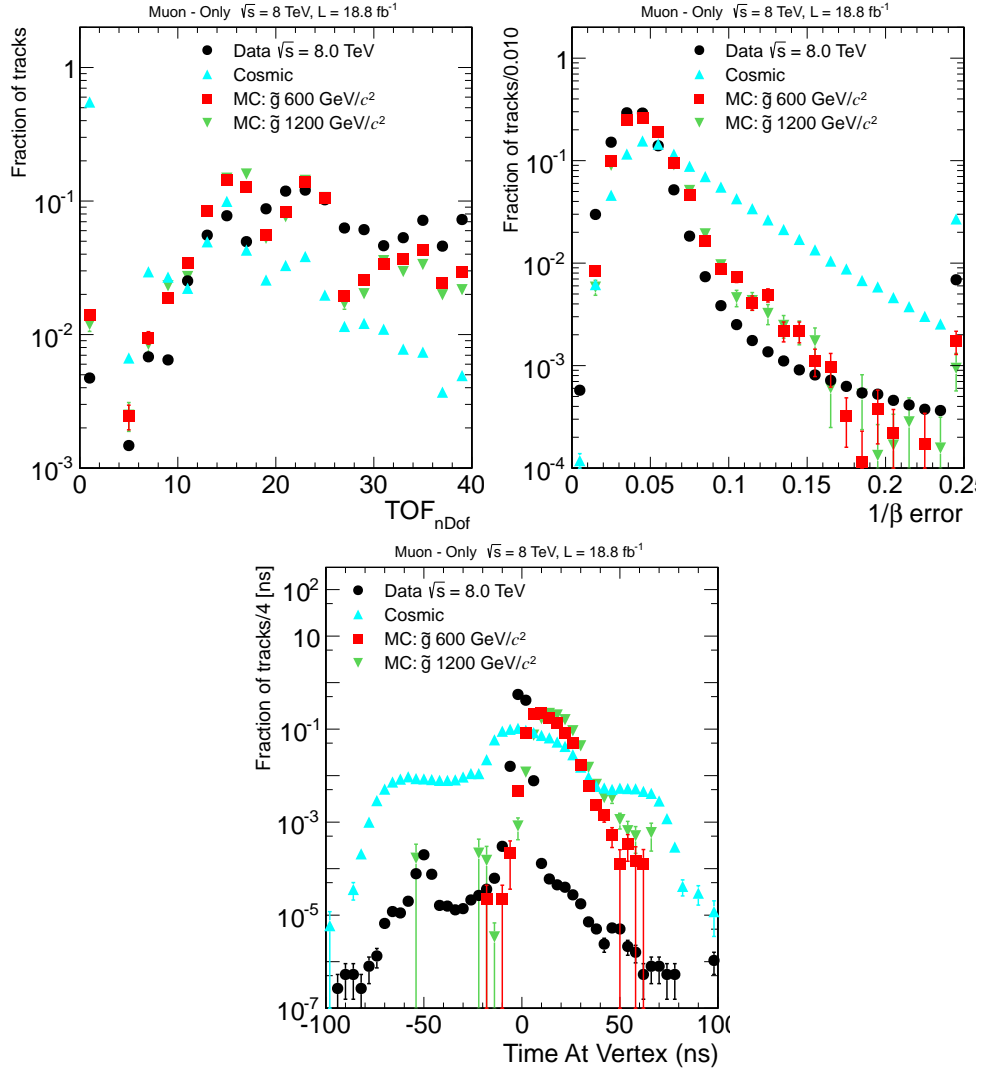
Figure 5.12: Distribution of various prelection variables in the *muon only* analysis for data, cosmic ray muon control sample, and signal MC. Top row: Number of degrees of freedom (left) and uncertainty (right) on the β^{-1} measurement. Bottom row: Time at vertex.
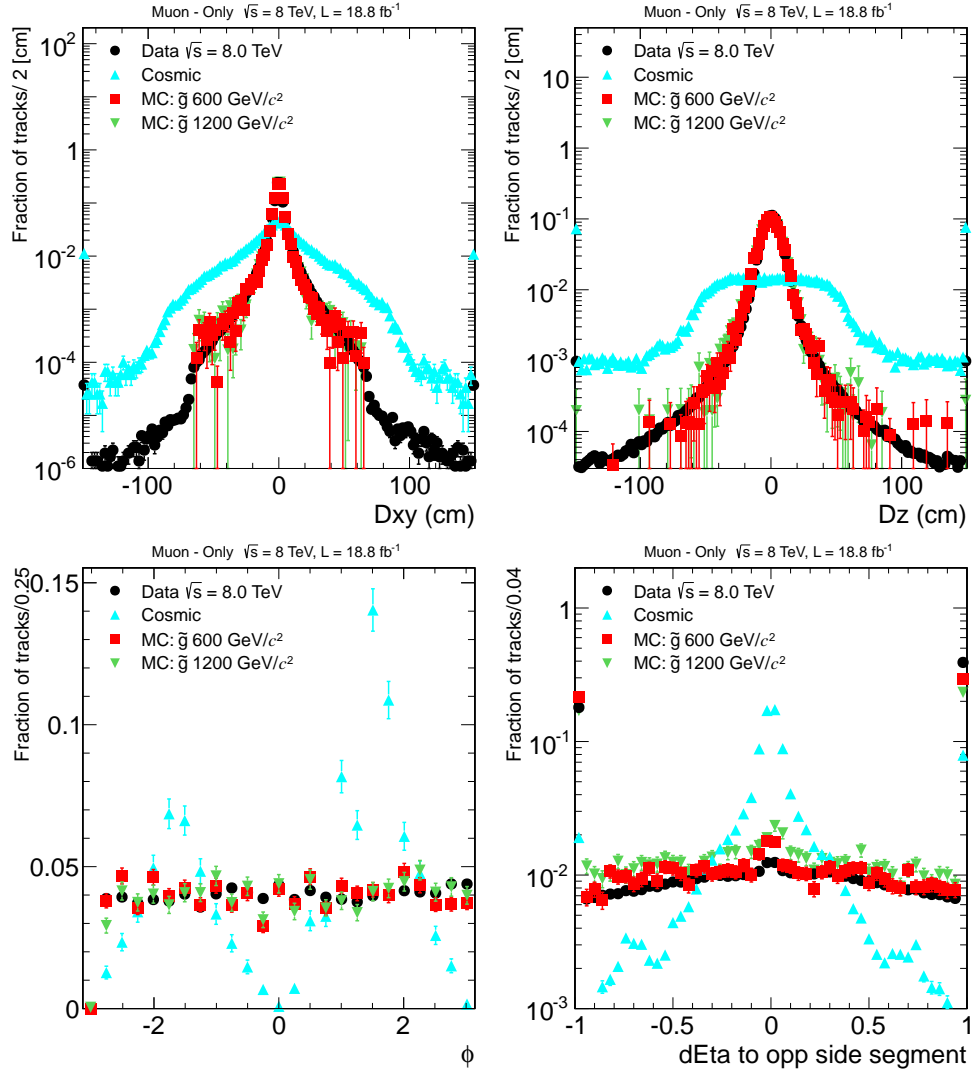
Figure 5.13: Distribution of various prelection variables in the *muon only* analysis for data, cosmic ray muon control sample, and signal MC. Top row: Disitribution of transverse (left) and longitudinal displacement (right). Bottom row: Distribution of the ϕ of the candidate (left) and the η separation of the candidate to muon segments (right). The rightmost bin in the η separation plot includes candidates where no segments were found.

5.6.2   Preselection for *muon+track*

The *muon+track* analysis applies cuts on the inner tracker track, which has a much better p_T and impact parameter resolution than the muon system track. The candidate is required to have $p_T > 45$ and $|\eta| < 2.1$ to match the trigger level requirements. Quality cuts are applied as low quality background tracks can have mismeasured momentum and potentially high fluctuations in dE/dx. The inner track is required to have at least eight hits in the inner tracker with at least two coming from the pixel detector. At least 80% of the hits associated with the track must be considered valid. A cleaning procedure is applied to the hits before calculating dE/dx and there must be at least six measurements passing this cleaning. Figure 5.14 shows these variables for data and signal MC.

The relative uncertainty on the candidate p_T (σ_{p_T}/p_T) must be less than 0.25 and the χ^2 per degree of freedom must be less than five. While cosmic ray muons are expected to be a negligible background in the *muon+track* analysis loose cuts are placed on the impact parameter of the track, these cuts are nearly 100% efficient for signal particles. The displacement of the track with respect to the primary vertex with the smallest longitudinal displament must be less than 0.5cm in both the transverse and longitudinal directions. Figure 5.15 shows p_T uncertainty, χ^2 per degree of freedom, and the d_z and d_{xy} displacement for data and signal MC.

Isolation cuts are also applied in the *muon+track* analysis. Isolated means that there not be many high energy particles near the candidate. This is required to reduce the background from jets where overlapping tracks could give anomolously high dE/dx values. The isolation cuts are kept very loose as the goal is not to find isolated particles but just to reject very high energy jets. The sum of the momentum of the tracks within 0.3 in $\eta - \phi$ space of the candidate

65
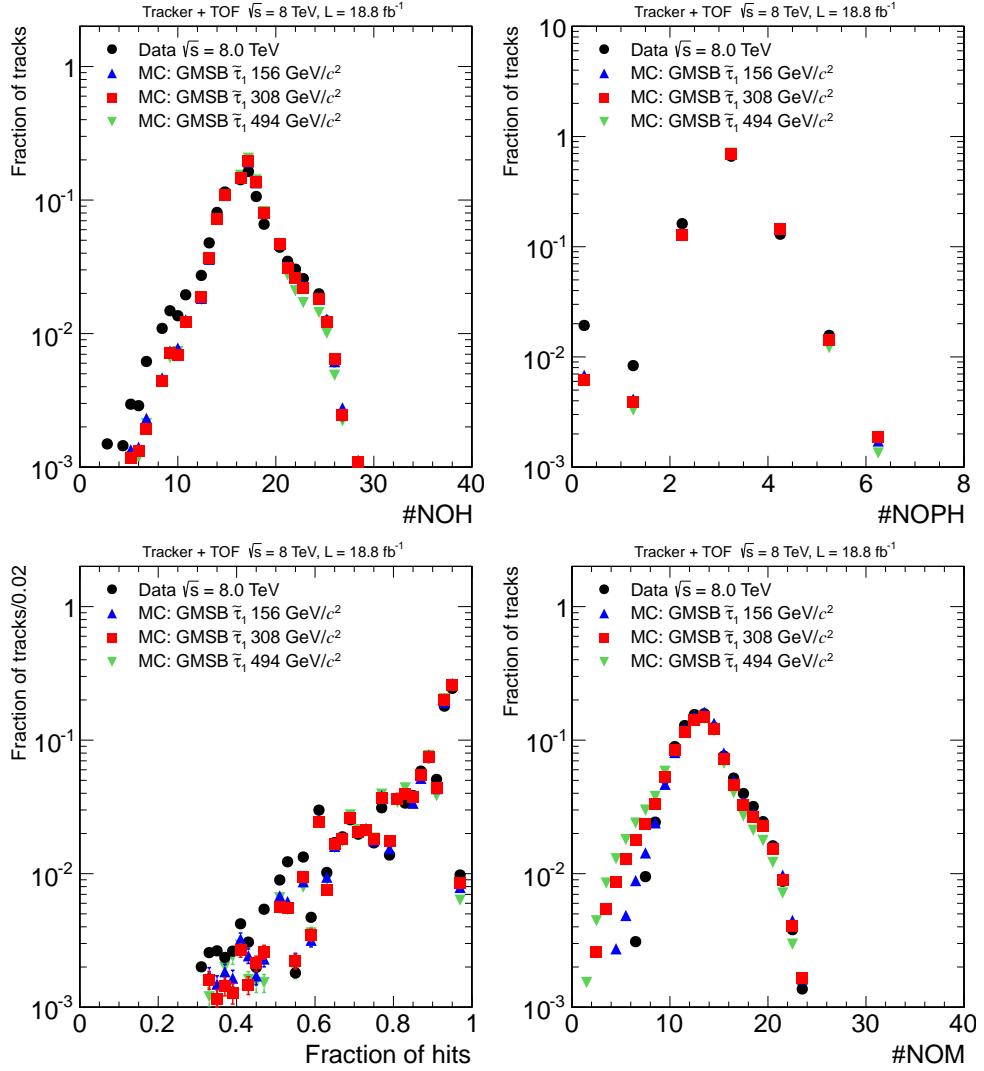
Figure 5.14: Distribution of various prelection variables in the *muon+track* analysis for data and signal MC. Top row: Number of tracker (left) and pixel (right) hits. Bottom row: Fraction of valid tracker hits (left) and number of measurements used for the *dE/dx* calculation (right).
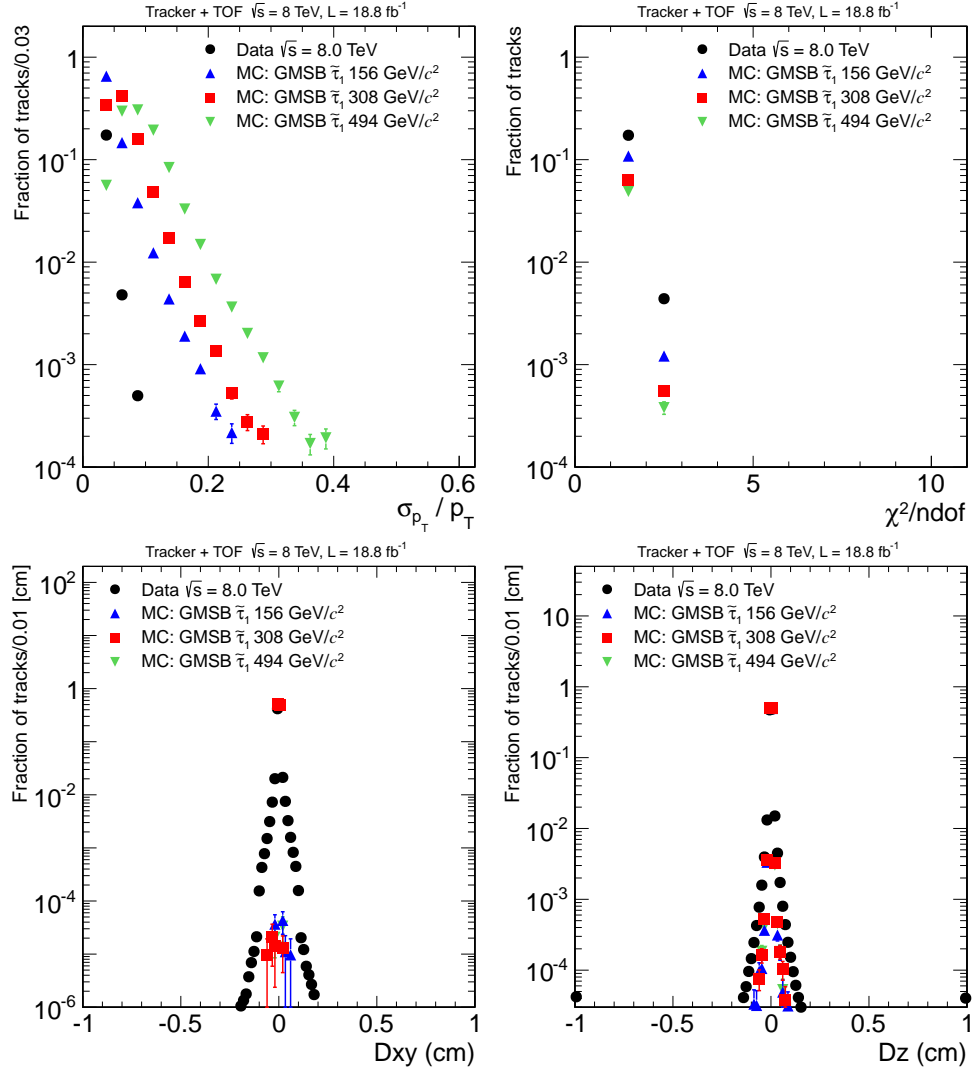
Figure 5.15: Distribution of various prelection variables in the *muon+track* analysis for data and signal MC. Top row: Relative p_T uncertainty (left) and χ^2 per degree of freedom (right). Bottom row: Displacement in the transverse (left) and longitudinal (right) directions.

(excluding the candidate itself) is required to be less than 50 GeV. Additionally the total amount of energy measured in the calorimeter within a radius of 0.3 in $\eta - \phi$ space to the candidate divided by the candidate momentum must be less than 0.3.

Additionally, the *muon+track* analysis uses the same cuts on the β^{-1} uncertainty and number of measurements as the *muon only* analysis. Figure 5.16 shows the isolation and β^{-1} variables for data and signal MC.

5.6.3 Preselection for *track only* and *multiple charge*

The *track only* analysis applies the same preselection as the *muon+track* analysis except the cuts on the timing measurement are not applied as the candidates are not required to be reconstructed in the muon system.

The *multiple charge* analysis applies the same selection criteria as the *muon+track* analysis except the cut on relative isolation less than 0.3 and the cleaning of the hits used for the dE/dx calculation is not done. The cleaning procedure is not applied because the amount of charge deposited is proportional to Q^2 meaning that even a $Q = 2e$ HSCP will deposit four times as much charge as a $Q = 1e$ HSCP. As the tracker saturates for a charge approximately three times that expected for a MIP many of the hits from $Q > 1e$ HSCP will be saturated and this can confuse the cleaning procedure. Additionally, as the high charge samples deposit so much charge, there will still be good signal/background separation even with longer tails in the dE/dx distribution. Figure 5.17 shows the number of measurements passing the cleaning for multiply charged samples.
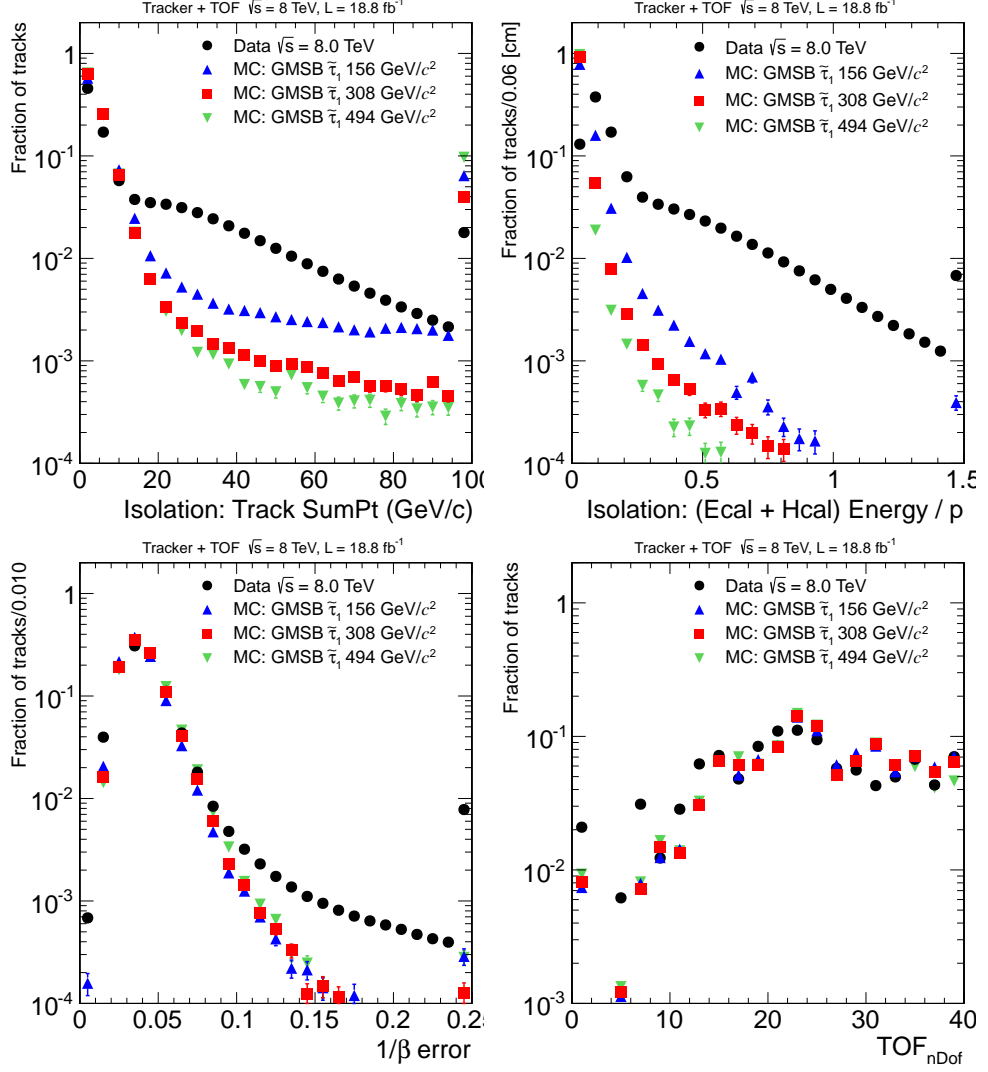
Figure 5.16: Distribution of various prelection variables in the *muon+track* analysis for data and signal MC. Top row: Sum momentum of tracks within 0.3 (left) and calorimeter energy within 0.3 divided by track momentum (right). Bottom row: Distribution of the β^{-1} measurement uncertainty (left) and the number of degrees of freedom (right).
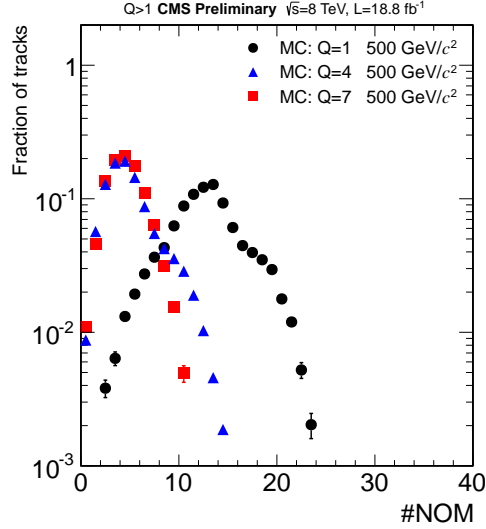
Figure 5.17: Distribution of number of dE/dx measurements passing cleaning for samples of three different charges

5.6.4 Summary of Preselection

The preselection criteria applied on the track in the muon system used in the *muon only*, *muon+track*, and *multiple charge* analyses are summarized in Table 5.3. The preselection criteria applied on the track in the inner tracker used in the *muon+track*, *track only*, and *multiple charge* analyses are summarized in Table 5.4.

The total preselection efficiency is shown in Tables 5.5 and 5.6 for the SUSY and modified DY samples, respectively. The efficiencies are presented with respect to HSCP reconstructed as a track in CMS. The inefficiency for the *muon only* analysis mostly arises from the cuts used to suppress the background from cosmic ray muons. The other analyses lose efficiency due to quality requirements on the inner track and dE/dx measurement which are necessary to constrain the background from misreconstructed tracks. Additionally, as CMS reconstruction generally assumes signatures of SM particles, HSCP tracks can have a lower qual-

Table 5.3: Preselection criteria on the muon system track used in the various analyses as defined in the text.

	muon only	*muon+track*	$\|Q\| > 1e$
# TOF measurements		> 7	
$\sigma_{1/\beta}$		< 0.07	
$1/\beta$		> 1	
$\|\eta\|$	< 2.1		$-$
p_T (GeV/c)	> 80		$-$
d_z and d_{xy} (cm)	< 15		$-$
# DT or CSC stations	> 1		$-$
Opp. segment $\|\eta\|$ difference	> 0.1		$-$
$\|\phi\|$	< 1.2 OR > 1.9		$-$
$\|\delta t\|$ to other beam crossing (ns)	> 5		$-$

Table 5.4: Preselection criteria on the inner tracker track used in the various analyses as defined in the text.

	muon+track	track only	$|Q| > 1e$
$|\eta|$		< 2.1	
p_T (GeV/c)		> 45	
d_z and d_{xy} (cm)		< 0.5	
σ_{p_T}/p_T		< 0.25	
Track χ^2/n_d		< 5	
# Pixel hits		> 1	
# Tracker hits		> 7	
Frac. Valid hits		> 0.8	
$\Sigma p_T^{trk}(\Delta R < 0.3)$ (GeV/c)		< 50	
# dE/dx measurements		> 5	
dE/dx strip shape test	yes		no
$E_{cal}(\Delta R < 0.3)/p$	< 0.3		$-$

Table 5.5: Preselection efficiency for a few benchmark SUSY samples in each analysis. This efficiency is with respect to the reconstructed HSCP candidate (i.e. muon system track for the *muon only* analysis and muon system plus inner tracker for the *muon+track* analysis). The fraction of glueballs assumed for the gluino samples is given in parantheses at the end of the signal name.

Model	*muon only*	*muon+track*	*track only*
Gluino 500 GeV (1.0)	44%	-	-
Guino 1000 GeV (1.0)	40%	-	-
Gluino 500 GeV (0.1)	44%	60%	70%
Gluino 1000 GeV (0.1)	43%	42%	51%
Gluino(CS) 500 GeV (0.1)	-	-	64%
Gluino(CS) 1000 GeV (0.1)	-	-	47%
Stop 600 GeV	48%	53%	61%
Stop (CS) GeV	56%	-	56%
GMSB Stau 370 GeV	-	76%	78%

ity than a SM particle would. The requirements are set trying to balance keeping the signal efficiency high while maintaining a low background contamination of the signal region.

The distributions of p_T and β^{-1} for the *muon only* analysis for data, cosmic ray muon control sample, and various signal models is shown in Figure 5.18 after applying the preselection requirements. Figure 5.19 shows the p_T, β^{-1}, and dE/dx distributions after applying the *muon+track* preselection cuts for data and various signal models.

Table 5.6: Preselection efficiency for a few benchmark modified DY samples in each analysis. This efficiency is with respect to the reconstructed HSCP candidate (i.e. muon system plus inner track for the *multiple charge* analysis and inner track for the *track only* analysis).

Model	*muon+track*	*track only*	*multiple charge*
DY $Q = 1e$ 600 GeV	72%	76%	75%
DY $Q = 3e$ 600 GeV	-	-	71%
DY $Q = 5e$ 600 GeV	-	-	50%
DY $Q = 7e$ 600 GeV	-	-	37%
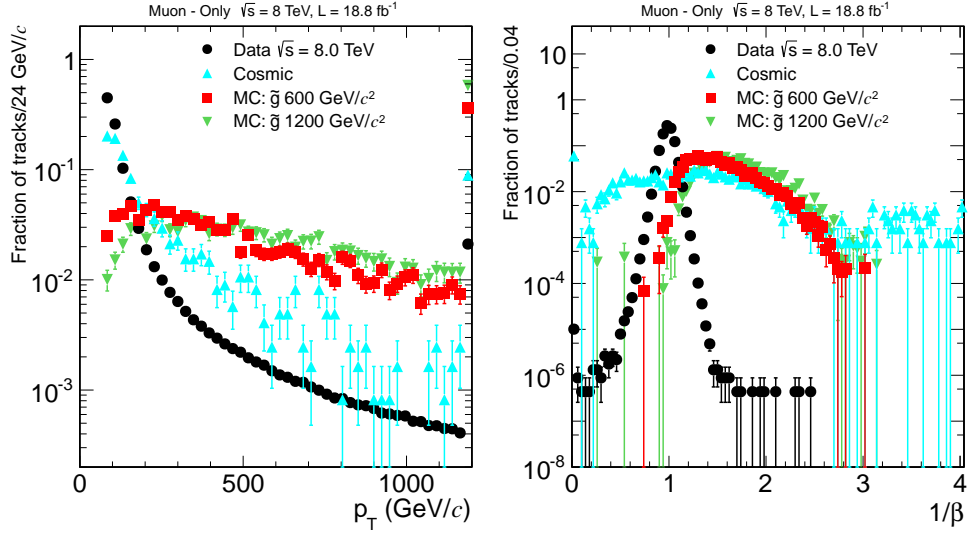
Figure 5.18: Distribution of selection variables for data, cosmic ray muon control sample, and signal MC. Left: Distribution of p_T. Right: Distribution of β^{-1}.
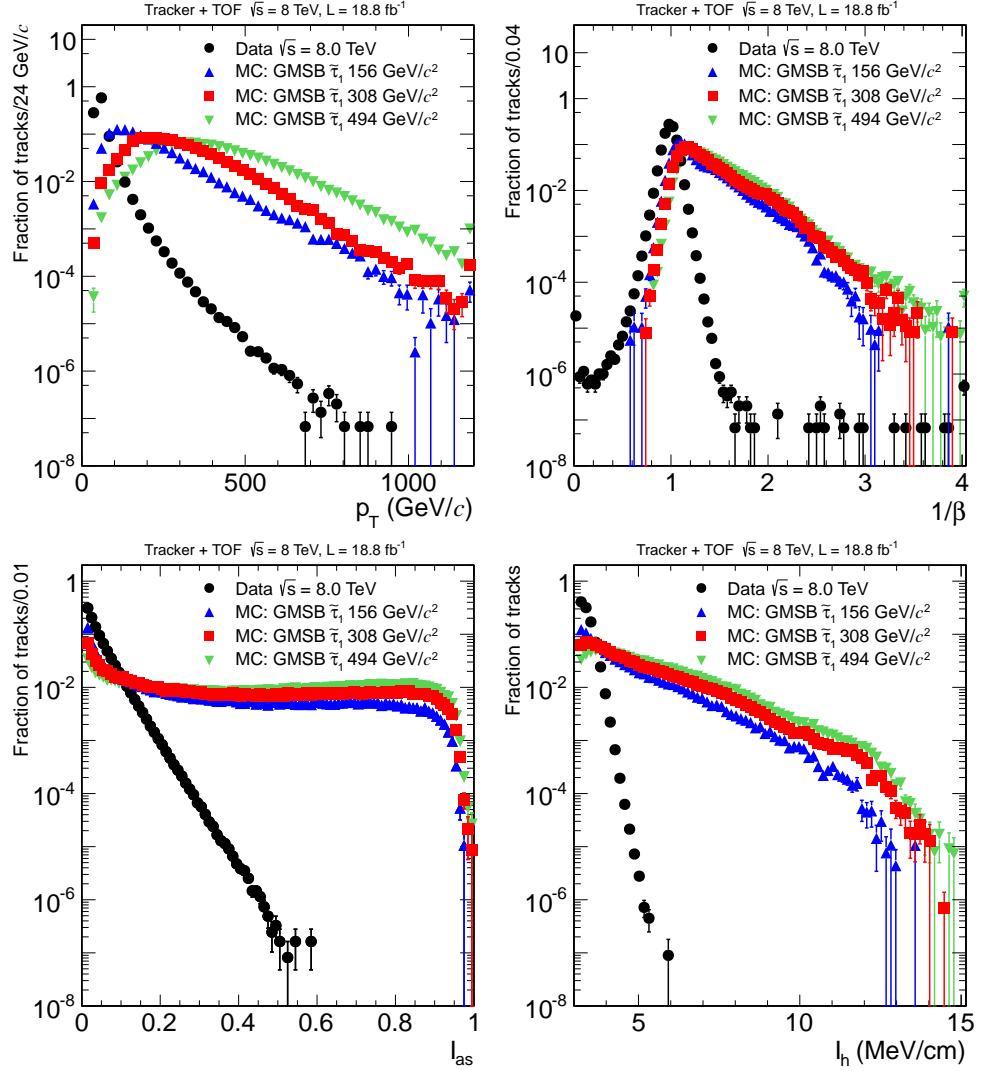
Figure 5.19: Distribution of section variables for data and signal MC. Top row: Distribution of p_T (left) and β^{-1} (right). Bottom row: Distribution of I_{as} (left) and I_h (right).

5.6.5 Tag and Probe Studies

The study of the agreement between data and MC for numerous muon qualities is done by the Muon Physics Object Group (POG) inside of CMS. The group provides scale factors for correcting MC to match data. For all of the analyses except for *muon only* it is sufficient to use results obtained from this group as the muon qualities they use are common within CMS. However, as the *muon only* analysis uses numerous variables which are unique to it, the results from the muon POG are not applicable.

For this reason, additional studies were performed to test the agreement of MC with data. The efficiency of the selections was checked with a tag and probe procedure (from the Muon POG) using muons from the decay of the Z boson. Z bosons decay to a particle and its anti-particle with the invariant mass of the particle–anti-particle pair equal to the mass of the Z boson they were created from.

The tag and probe procedure proceeds by requiring one muon, the tag muon, be found with a very stringent selection trying to assure that this is a good muon. The tag muon is required to pass a tight selection recommended by the Muon POG and to match to an object that triggered the readout of CMS. The last requirement assures that no bias is introduced by the need for the event to readout. Additionally, the tag must pass the requirements of a skim that was used to reduce the data size to a level making processing reasonable. The skim requirements are at least three dE/dx measurements and $I_h > 3.0$ or $I_h < 2.8$.

Then a set of probe candidates are defined as tracks reconstructed in the inner tracker with no requirement of muon system activity. The probes are required to have $p_T > 40$ GeV, $|\eta| < 2.1$, and the opposite charge of the tag muon. The invariant mass of the tag and probe is then required to be within 10 GeV of the

mass of the Z boson, 91 GeV.

There are few processes other than Z boson decay that will lead to tag and probe pairs having an invariant mass around the mass of the Z boson. Thus it is likely that the probe is a muon. The efficiency that a muon passes the preselection in the *muon only* analysis can then be found by looking at the efficiency that the probe passes the preselection. The efficiencies in data and MC can be compared and any possible scale factors calculated. The residual background from non Z boson decay in the mass window is accounted for by a fit described below. The MC sample used only contains the creation of Z bosons, background processes are not included.

A simultaneous fit to pairs originating from Z bosons and pairs from background is performed using the sum of two Voigtians to represent Z bosons and an exponential for the background. Figures 5.20 and 5.21 show sample fits to data and MC, respectively. It can be seen that the fits match well. The efficiency is extracted from these fits using a procedure from the muon POG.

Figure 5.22 shows the efficiency for the probes to pass the preselection, except for the selection on p_T, against the probe p_T, η, and the number of vertices in the event. Overall the efficiency is approximately 75% in data and 80% in MC. The efficiency is mostly flat versus p_T and number of vertices but does depend on η. MC is scaled by an η dependent scale factor to correct for the discrepancy.

5.7 Background Prediction

All of the analyses count the number of events with a candidate passing threshold values on some grouping of the p_T, β^{-1}, and I_{as} variables. The *muon+track* and *track only* analyses also place a requirement on the mass of the candidate as

Passing Probes

Failing Probes

Events / (0.4 GeV/c²)

Tag-Probe Mass (GeV/c²)

All Probes

Events / (0.4 GeV/c²)

Tag-Probe Mass (GeV/c²)

efficiency = 0.760 ± 0.001
lf = -0.148 ± 0.05
lp = -0.115 ± 0.01
mean1 = 90.73 ± 0.01
mean2 = 86.9 ± 0.3
numBackgroundFail = 120 ± 39
numBackgroundPass = 731 ± 91
numSignalAll = 99965 ± 331
sigma1 = 1.34 ± 0.02
sigma2 = 3.1 ± 0.1
vFrac = 0.87 ± 0.01
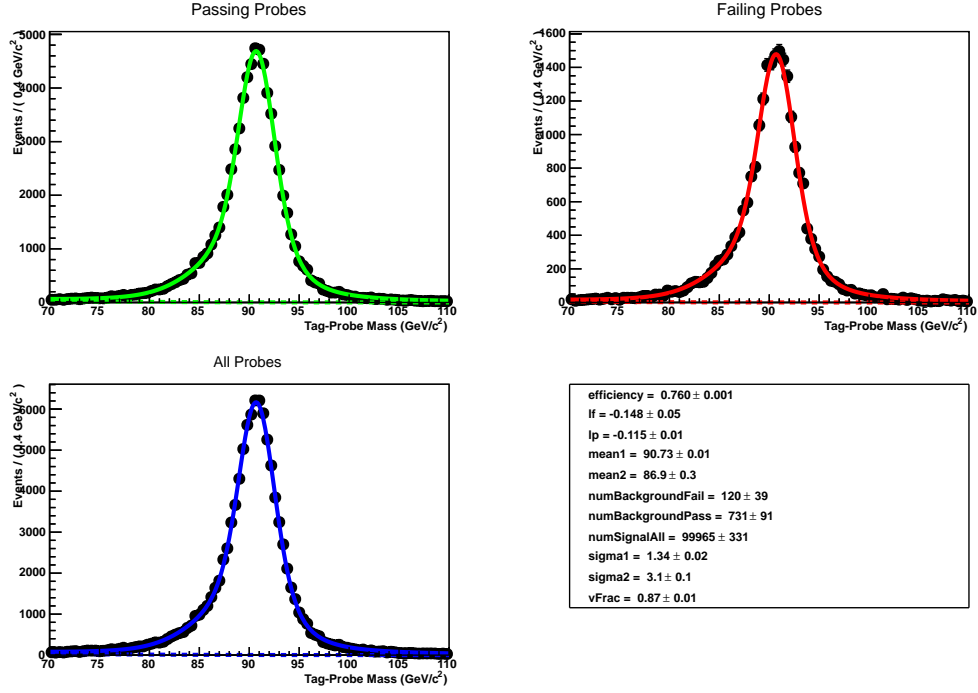
Figure 5.20: Example fits to invariant mass distributions in the tag and probe procedure for the *muon only* analysis for data. Top left: Mass distribution and fit for probes passing the preselection. Top right: Mass distribution and fit for probes failing the preselection. Bottom left: Mass distribution and fit for all probes. Bottom right: Parameters extracted from the fit.
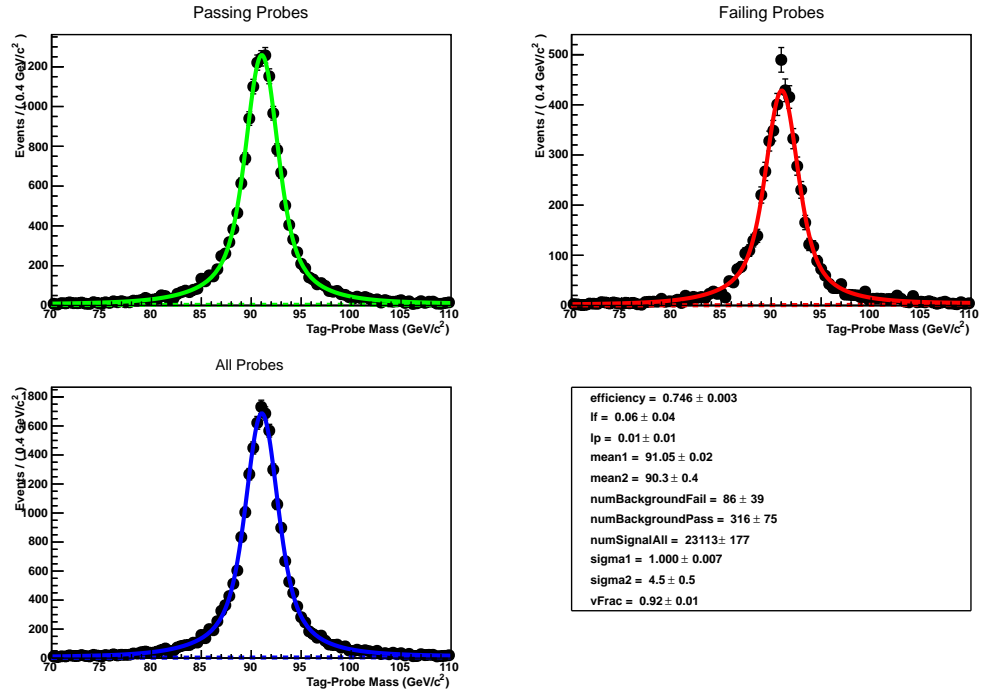
Figure 5.21: Same as Fig. 5.20 but for MC.
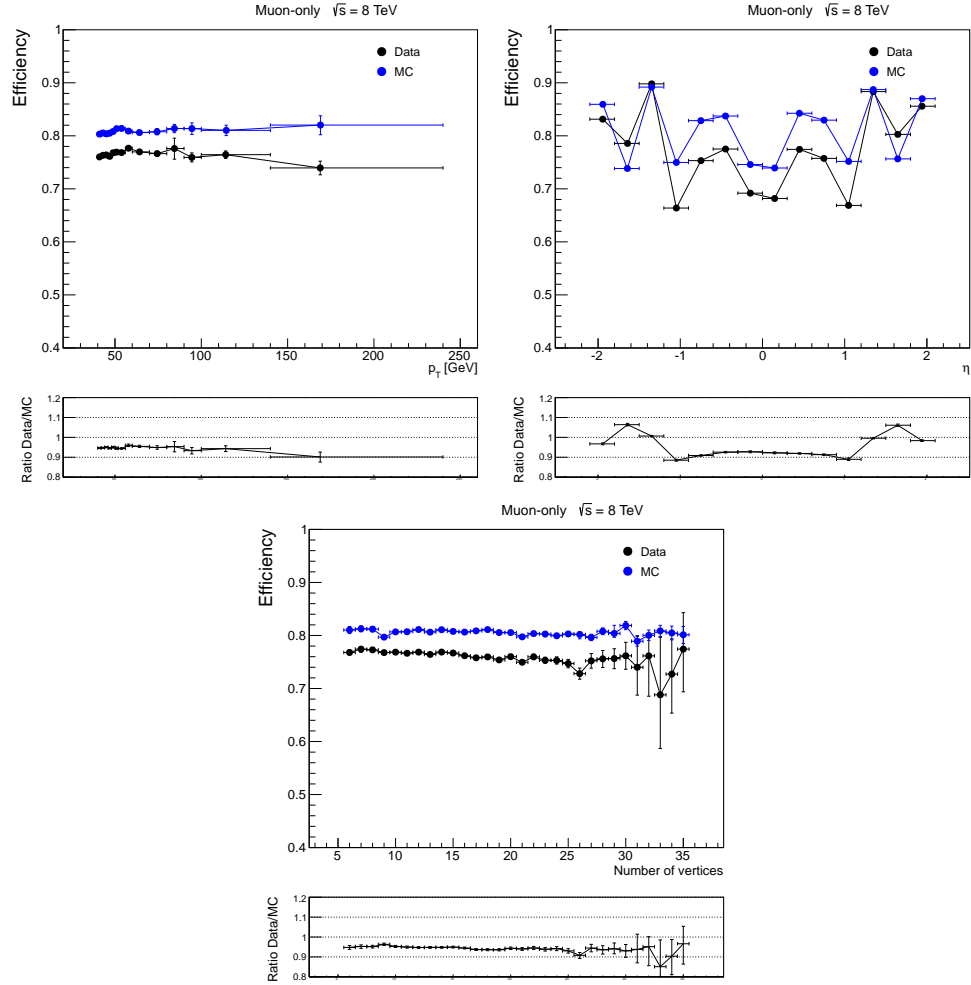
Figure 5.22: Efficiency to pass preselection cuts for the *muon only* analysis. Top row: Versus p_T (left) and η (right) Bottom row: Versus number of primary vertices (right).

described below. There are two sources of background considered in the analyses.

The first is muons, or for the *track only* analysis any charged SM particle, from the collisions in the LHC. Muons can pass the thresholds on the selection variables for a variety of reasons. All muons at the LHC will be travelling at very nearly the speed of light, but finite detector resolution results in a smearing of the measured time of hits. This can cause muons to have a high measured β^{-1}. While muons in the momentum region of interest all deposit approximately the same amount of energy in the tracker on average, the amount deposited in each interaction is subject to large variations. This can lead to muons with a high dE/dx value. Detector resolution can also contribute to muons with high dE/dx. Additionally, collision muons can have large reconstructed momentum, either due to true high momentum or detector mismeasurement promoting a low momentum muon to a high reconstructed momentum. Detector mismeasurement is especially important for the momentum measured in the muon system.

Collision muons are predicted exploiting the lack of correlation between the selection variables for muons through the $ABCD$ method. In the $ABCD$ method, multiple bins are defined by whether the candidate passes thresholds on the selection variables. In the normal two dimensional version of the $ABCD$ method, two selection variables are used and four regions are defined. The A region has candidates failing both of the thresholds on the selection variables, B (C) fails only the threshold on the first (second) of the selection variables. The signal region, D, passes the threshold on both selection variables. The number of background muons in the D region can be predicted as $B \times C/A$, where the letters represent the number of candidates in the regions. This prediction holds as long as the probablity for a background muon to pass the threshold on one of the variables is independent of whether it passes the threshold of the other.

Table 5.7: Bin naming convention. The signal region is always the D region.

Name	p_T	β^{-1}	dE/dx
A	Fail	Fail	Pass
B	Fail	Pass	Pass
C	Pass	Fail	Pass
D	Pass	Pass	Pass
E	Fail	Fail	Fail
F	Fail	Pass	Fail
G	Pass	Fail	Fail
H	Pass	Pass	Fail

Tests of the correlation between the selection variables is given below.

The four different analyses use different combinations of the selection variables defined in Sec. 5.5. In order to simplify the nomenclature in this section, Table 5.7 defines the names of bins and whether they pass or fail the thresholds on the selection variables. For all the selection variables passing means having a value above the threshold. If a selection variable is not used in an analysis then it is taken to have passed. For all the analyses the D region is the signal region.

In order to perform systematic studies, the analyses that use β^{-1} reverse the preselection requirement on β^{-1} greater than one. This creates a group of candidates measured as going faster than the speed of light, making it signal free. As the β^{-1} distribution is close to symmetrical for background muons this makes the region very good for testing the background prediction. New bins are defined as in Table 5.7 but now β^{-1} is said to have passed if the value is below the threshold. The bins are referred to with a prime to denote that they are from the control region, so the new "signal" region would be referred to as D'.

The second source of background, important only for the *muon only* analysis, is muons from cosmic rays. As discussed in Section 2.2 muons from cosmic rays are constantly passing through CMS. Cosmic ray muons will arrive to the muon system asynchronously with collisions in the LHC. Depending on exactly when the cosmic ray muon arrives in the muon system relative to collisions in the LHC this can give rise to a particle with a large β^{-1} measurement. Out of time particles are not centered in the tracker's charge collection window giving them lower dE/dx. This combined with the impact parameter requirements applied at preselection makes cosmic ray muons negligible for the analyses looking for high dE/dx in the tracker. The distribution of p_T for cosmic ray muons falls off at high momentum slower than for collision muons, as evidenced in Figure 5.18 (left). As cosmic ray muons have different β^{-1} and p_T distributions than collision muons they will not be accurately predicted with the same method used to predict the collision muon background in the *muon only* analysis. A dedicated method using the cosmic ray muon control sample is described below.

For all the analyses the systematic uncertainty on the expected background in the signal region is estimated from the spread of various background estimations.

The following variables are defined:

$$V_N^{syst+stat} = \sqrt{\sum_i \left(x_i - <x>\right)^2 / (N-1)}$$

$$V_N^{stat} = \sqrt{\sum_i \left(\sigma_i\right)^2 / N} \tag{5.3}$$

$$V^{syst} = \sqrt{V_{syst+stat}^2 - V_{stat}^2}$$

where N is the number of estimates considered, the sum is over N, x_i is the value of the ith background estimate, and σ_i is the statistical uncertainty on the ith background estimate. The first quantity is an estimator of the variance of the background estimates, which takes both statistical and systematic contributions.

The second quantity is adopted as an estimator of the contribution of the statistical uncertainties to the variance. Finally, the contribution of the systematic uncertainty to the background estimates is taken assuming that the latter adds in quadrature to the statistical uncertainty and is therefore obtained from the last expression.

5.7.1 Prediction for *muon only* analysis

The collision muon background in the *muon only* analysis is predicted with the selection criteria of β^{-1} and p_T in the $ABCD$ method. The expected number of background candidates in the signal region D (see Table 5.7) is predicted as $B \times C/A$.

The $ABCD$ method only works if the probability to pass one of the thresholds is independent of the other variable. However, it has been observed that a correlation exists between the p_T and β^{-1} measurements based on whether the candidate is in the barrel or forward region of the detector as well as the number of DT or CSC stations containing valid hits. Six bins are created defined by the η of the candidate, greater or less than 0.9, and the number of stations, 2, 3, or 4. The distributions of p_T and β^{-1} in the six regions is shown in Figure 5.23. The predicted number of events in each bin is predicted separately and the total number of predicted background events is the sum of the six predictions.

After the binning the correlation is small enough not to bias the background prediction as can be seen in Figs. 5.24 and 5.25

To predict the cosmic ray muon background sidebands in the $|\delta_z|$ distribution and the pure cosmic ray muon sample are used. The number of candidates, N, in a sideband region of $|\delta_z|$ are counted. The candidates are required to pass the full selection except the $|\delta_z|$ requirement is changed to $70 < |\delta_z| < 120$cm
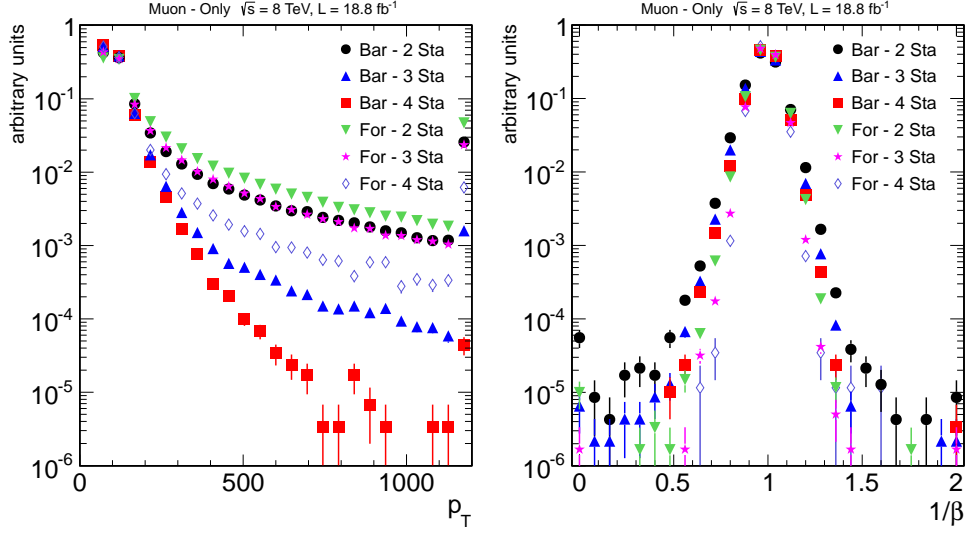
Figure 5.23: Distribution of p_T and β^{-1} for data for six different regions depending on whether the candidate is in the barrel (Bar) or forward (For) region of CMS and number of muon stations used in the fit.

and the requirements on $|\delta_{xy}|$, ϕ, segment η separation, and p_T are removed to increase the number of cosmic ray muons in the sideband region. Additionally the candidates are required not to be reconstructed in the inner tracker to decrease the contamination from collision muons. The ratio, R, of candidates in the $|\delta_z|$ sideband region relative to the signal region is calculated using the pure cosmic ray muon sample with the same offline requirements as in the main data sample. The number of cosmic ray muons passing the final selection is then predicted as

$$P_{Cosmic} = N \times R \tag{5.4}$$

Numerous effects cancel in this ratio making the prediction robust. The number of cosmic ray muons in any of the regions can be expressed as $C = F \times T \times \epsilon$, where C is the number of cosmic ray muons observed, F is the flux of cosmic ray
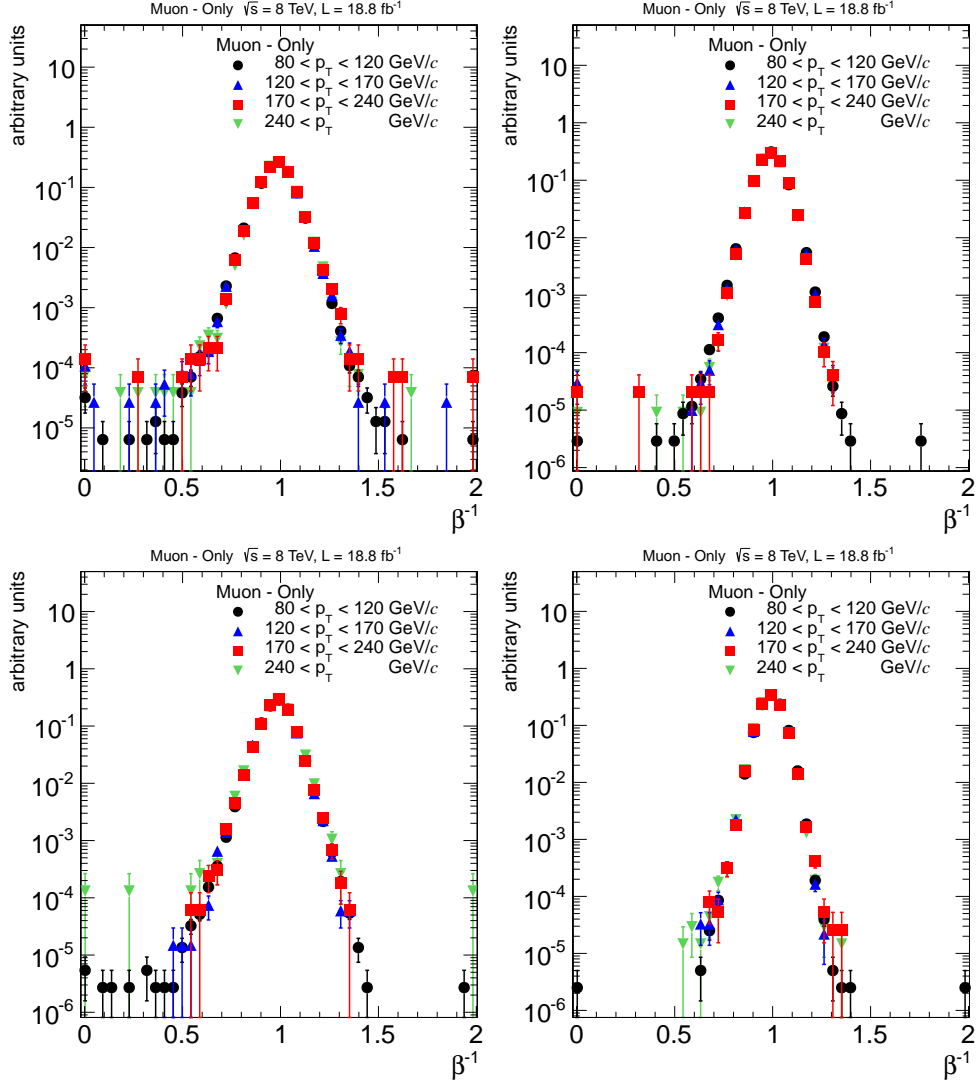
Figure 5.24: Distribution of β^{-1} for different momentum regions for four of the six different bins that are used to make the prediction. The left column shows the barrel region while the right column shows the forward region. The top (bottom) row are for 2 (3) stations.
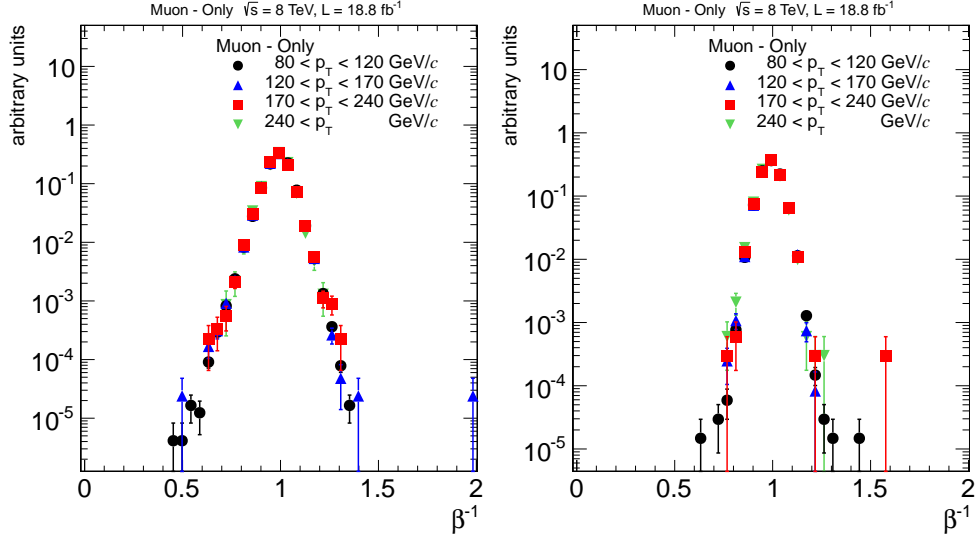
Figure 5.25: Distribution of β^{-1} for different momentum regions for four station tracks. The left column shows the barrel region while the right column shows the forward region.

muons per second, T is the amount of time that CMS was collecting data, and ϵ is the efficiency of the detector to reconstruct and select cosmic ray muons in the region including detector acceptance effects. The ratio R can then be written as

$$R = F \times T_{Control} \times \epsilon_{Control}^{Signal} / (F \times T_{Control} \times \epsilon_{Control}^{Sideband}) \qquad (5.5)$$

where Control refers to the cosmic ray muon control trigger and signal and sideband represent the $|d_z|$ signal and sideband regions, respectively.

The number N in the sideband region is written as

$$N = F \times T_{Main} \times \epsilon_{Main}^{Sideband} \qquad (5.6)$$

87

and the number of cosmic ray muons expected in the signal region as

$$P_{Cosmic} = F \times T_{Main} \times \epsilon_{Main}^{Signal} \tag{5.7}$$

with Main referring to the samples gathered with the main analysis triggers. Then Eq. 5.4 can be restated as

$$F \times T_{Main} \times \epsilon_{Main}^{Signal} = F \times T_{Main} \times \epsilon_{Main}^{Sideband} \times$$
$$F \times T_{Control} \times \epsilon_{Control}^{Signal}/(F \times T_{Control} \times \epsilon_{Control}^{Sideband}) \tag{5.8}$$

After the cancellation of numerous factors this equation reduces to

$$\epsilon_{Main}^{Signal} = \epsilon_{Main}^{Sideband} \times \epsilon_{Control}^{Signal}/\epsilon_{Control}^{Sideband} \tag{5.9}$$

It is clear that as long as the relationship

$$\epsilon_{Main}^{Signal}/\epsilon_{Main}^{Sideband} = \epsilon_{Control}^{Signal}/\epsilon_{Control}^{Sideband} \tag{5.10}$$

holds the prediction will be accurate. The only difference between the two ratios is that one is using events collected with the main triggers while the other is using the cosmic ray muon control trigger. As the two triggers are essentially the same and were collected during the same run period it is likely the relationship holds. Thus the prediction of the number of cosmic ray muons in the signal region is likely good. Note that the relationship does not require the efficiency in the cosmic ray muon control sample to be the same as in the main sample. Only that the ratio of the efficiencies in the signal and sideband regions be the same in the two samples.
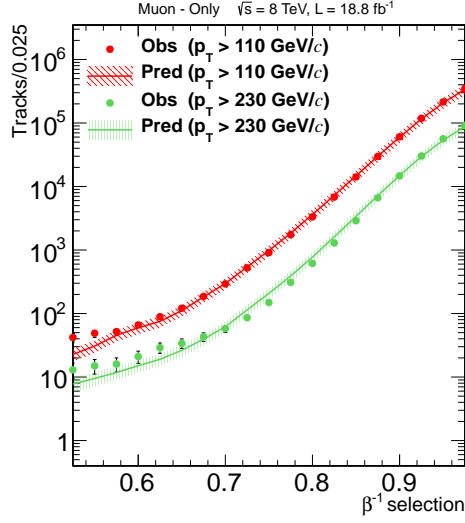
Figure 5.26: Number of predicted and observed events in the $\beta^{-1} < 1$ region for two different p_T thresholds. Threshold for β^{-1} set by X-axis.

As previously mentioned, the background prediction is checked using candidates with β^{-1} less than one. This region is useful as it is background dominated and it provides a good approximation of background candidates in the signal region as the β^{-1} distribution is roughly symmetrical about one for background candidates. The background prediction procedure described above is repeated but instead looking for candidates with high p_T and β^{-1} below some threshold. This is the same procedure that would be taken if looking for particles that travel faster than the speed of light. As described above, the bins in the low β^{-1} region are given a prime so the number of candidates in the "signal" region D' can be predicted as $C' \times B'/A'$. Figure 5.26 shows the number of predicted and observed number of candidates in D' for different p_T and β^{-1} thresholds. Good agreement is seen between observed and predicted.

To determine the systematic uncertainty on the predicted collision background the β^{-1} less than one region is used once again. The predicted number of events
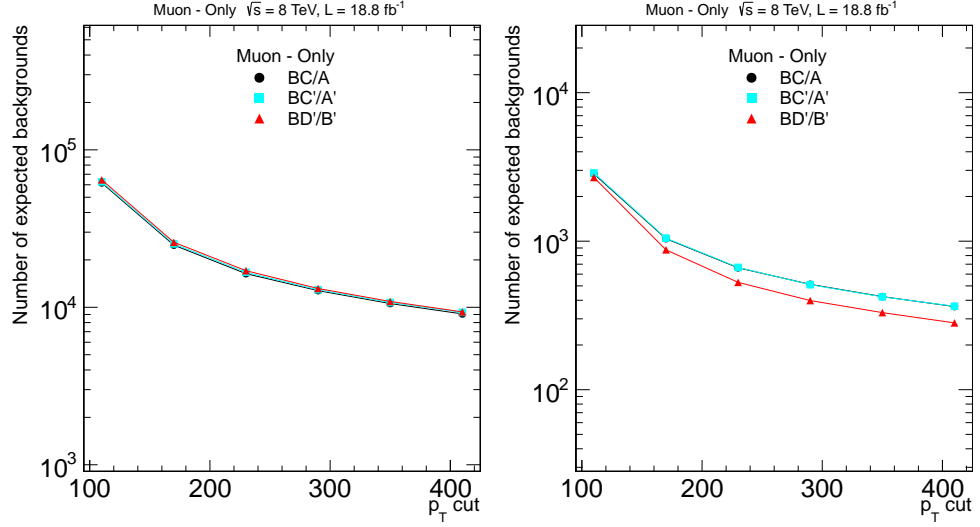
Figure 5.27: Distributions of the number of predicted events and their statistical uncertainty with different prediction formulae for different set of thresholds. The p_T threshold is defined by the x-axis. Left column: $1/\beta > 1.1$ (< 0.9 for low $1/\beta$ regions). Right column: $1/\beta > 1.2$ (< 0.8 for low $1/\beta$ regions).

in the signal region D can be predicted by three different formulae, the main one of $B \times C/A$ as well as $B \times C'/A'$ and $B \times D'/B'$. The first of these additional predictions would be sensitive to any shift in the β^{-1} distribution due to the p_T requirement while the second would be sensitive to any effect on the resolution due to the p_T requirement. Figure 5.27 shows the number of predicted events from the three predictions for different β^{-1} and p_T thresholds.

The systematic error is extracted from the three predictions through Eq. 5.3 with N=3. Fig. 5.28 shows the variation of $V_{syst+stat}/ < x >$, $V_{stat}/ < x >$ and $V_{syst}/ < x >$ as a function of the p_T threshold. The statistical uncertainty due to the number of candidates in the B group is not subtracted as it is completely correlated between the three predictions. From the last plot the systematic un-

Table 5.8: Predicted numbers of cosmic ray muon events for the *muon only* analysis.

Dz Region	Prediction
$30 < |dz| < 50$ cm	3.1 ± 0.5
$50 < |dz| < 70$ cm	2.6 ± 0.7
$70 < |dz| < 120$ cm	3.2 ± 1.0
120 cm $< |dz|$	3.8 ± 0.7

certainty on the expected background in the signal region is estimated to be 20%.

The systematic uncertainty on the cosmic ray muon background is determined by modifying the d_z range used to define the control sample. Predictions can also be made from candidates with $30 < |d_z| < 50$ cm, $50 < |d_z| < 70$ cm, and 120 cm $< |d_z|$. Table 5.8 shows the number of predicted cosmic ray muons for each $|d_z|$ region using the final selection defined in Section 5.9 The statistical uncertainty from the number of candidates in the signal region in the pure cosmic ray muon sample is not included in the uncertainties listed as it is correlated between the three predictions. Equation 5.3 with N=4 is used to calculate the systematic uncertainty. The relative systematic uncertainty is found to be 80%.

5.7.2 Prediction for *muon+track* analysis

The *muon+track* analysis uses three selection variables, p_T, β^{-1}, and I_{as}. With three selection variables an extended three dimensional version of the $ABCD$ method is used to predict the collision muon background. An additional requirement on the reconstructed mass of the candidate is also applied and the prediction of the background mass spectrum is described below. For each signal point, the
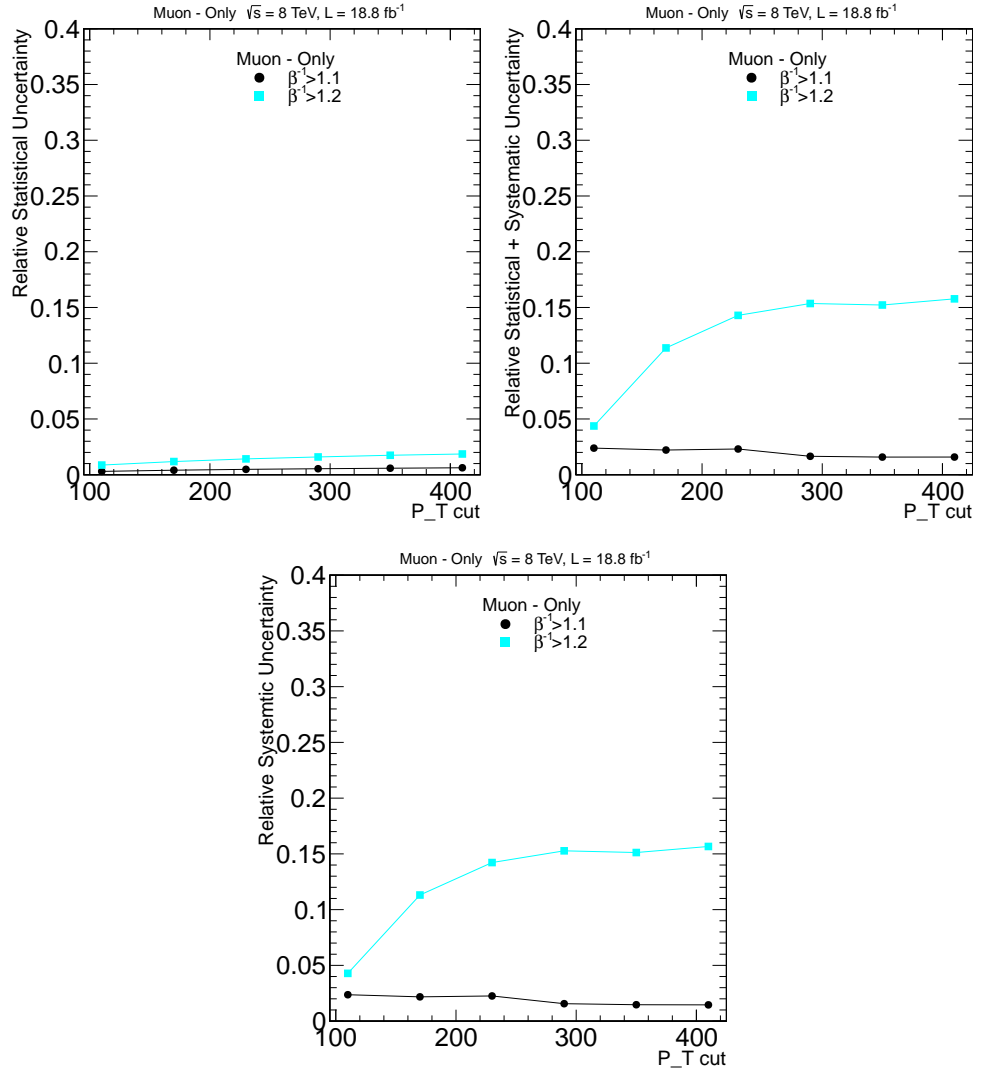
Figure 5.28: Calculation of uncertainty in the *muon only* analysis. Left: Ratio of the quadratic mean of the statistical uncertainties of the three possible background estimations to the mean of these estimations vs the p_T threshold. Middle: Ratio of the variance to the mean of the three background estimations vs p_T. Right: Ratio of the square root of the difference between the variance and the quadratic mean of the statistical uncertainties of the three possible background estimations and the mean vs p_T.

reconstructed mass of candidates must be above the average reconstructed mass of the signal minus two sigma of the mass distribution (both determined from MC) and below 2 TeV. As discussed above, the cosmic ray muon background is negligible for the *muon+track* analysis.

To test if the selection variables are uncorrelated, the distribution of one of the variables is plotted for numerous ranges of one of the other variables. If the variables are uncorrelated then the distributions should all be the same. The distributions are shown in Fig. 5.29 and the variables are found to be sufficiently uncorrelated.

Since the *muon+track* analysis employs three selection variables it uses all eight bins defined in Table 5.7. With eight bins, the number of predicted events in the signal region, D, can be found via seven different equations utilizing the various bins. The one with the smallest statisitical uncertainty, $A \times F \times G/E^2$, is chosen. The other equations are used to determine the systematic uncertainty on the prediction.

As with the *muon only* analysis the prediction is checked with candidates in the β^{-1} less than one region. Again the predicted number of events in D' is predicted following the same procedure as for the signal region except changing the β^{-1} requirement to be lower than some threshold. Figure 5.30 shows the predicted and observed number of candidates in the D' region for various thresholds. Good agreement is seen even with a tight selection.

Number of observed and predicted events In addition to the requirements on the selection variables, the *muon+track* analysis also applies a requirement on the estimated mass of the candidate as determined from Equation 5.1. In order to do this the mass spectrum of background candidates in the signal region must be predicted. The background mass spectrum is predicted using the dE/dx and
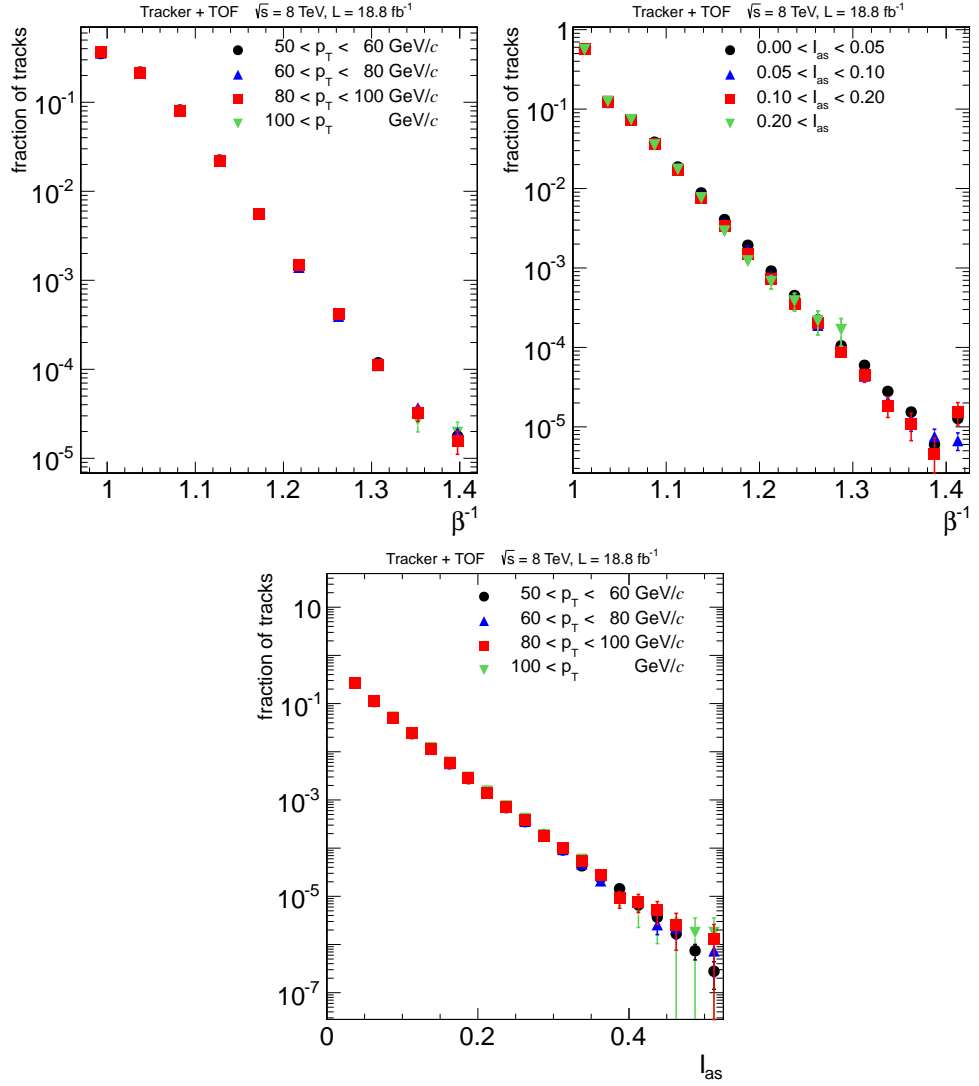
Figure 5.29: Top row: Measured I_{as} distributions for several momentum ranges (left) and β^{-1} distributions for several momentum ranges (right). Bottom row: Measured β^{-1} distributions for several I_{as} ranges. Results are for the *muon+track* selection.
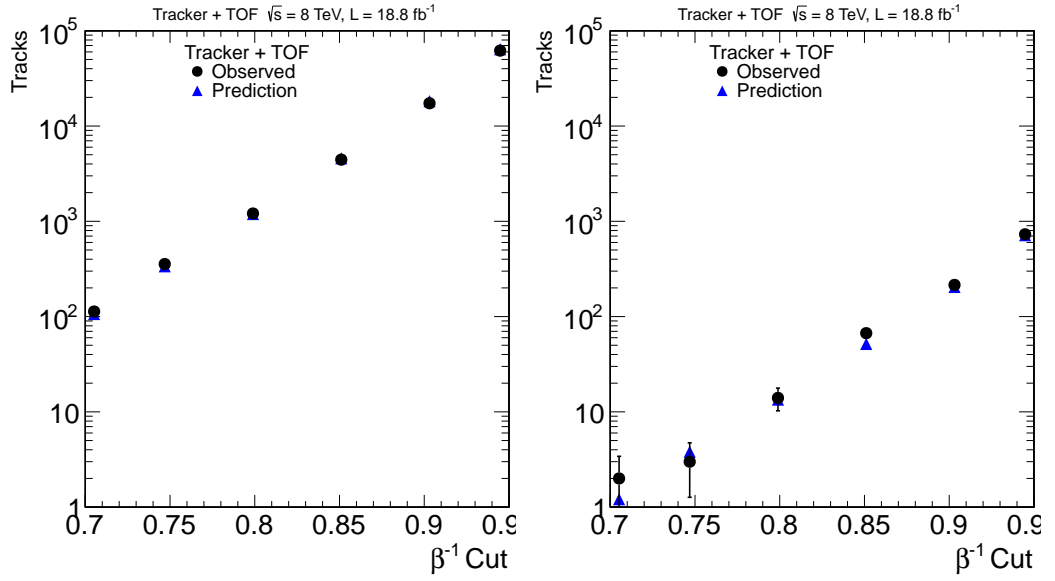
Figure 5.30: Number of observed and predicted events and their statistical error in the D' region for $p_T > 55, I_{as} > 0.1$ (left) and $p_T > 85, I_{as} > 0.2$ (right). Threshold on $1/\beta$ defined by the x-axis in the *muon+track* analysis.

momentum distributions taken from control regions. While the signal region is defined by thresholds on I_{as} and p_T (as well as β^{-1}), the mass prediction uses I_h and p so it is these distributions that must be taken from the control regions.

It has been found that the probability for background candidates to pass the threshold on I_{as} is dependent on the η of the candidate. The probability to pass the β^{-1} threshold has a small η dependence while the probability to pass the p_T threshold has almost no η dependence. These effects can be seen in Figure 5.31 which shows the η distribution of candidates which pass or fail the various thresholds.

This is found to have only a small effect on the total number of predicted events but does bias the predicted mass spectrum which uses p instead of p_T. The p_T distribution of background candidates is roughly the same versus η however this implies that the p distribution does vary, as momentum can be written as a function of only p_T and η. To correct for this a reweighting procedure is done such that the candidates used to determine the p distribution match the η distribution of candidates used to obtain the I_h distribution.

The p (I_h) distribution is taken from the G (A) region where only the p_T (I_{as}), value is above threshold and the other two are below. The mass distribution is then predicted by performing approximately 100 pseudo-experiments. The ith pseudo-experiment is done through multiple steps. First a value of E_i, F_i, is drawn from a poisson distribution with a mean equal to the observed number of candidates in the E, F, regions in data. Next, a binned distribution of the p of candidates in the G region is employed. A value of n_{ij}, where j represents the bin of the p distribution, is drawn for each p bin from a poisson distribution with mean equal to the number of candidates observed in that bin in data. A value of G_i is then found as the sum over j of the n_{ij}. A similar procedure is done in the
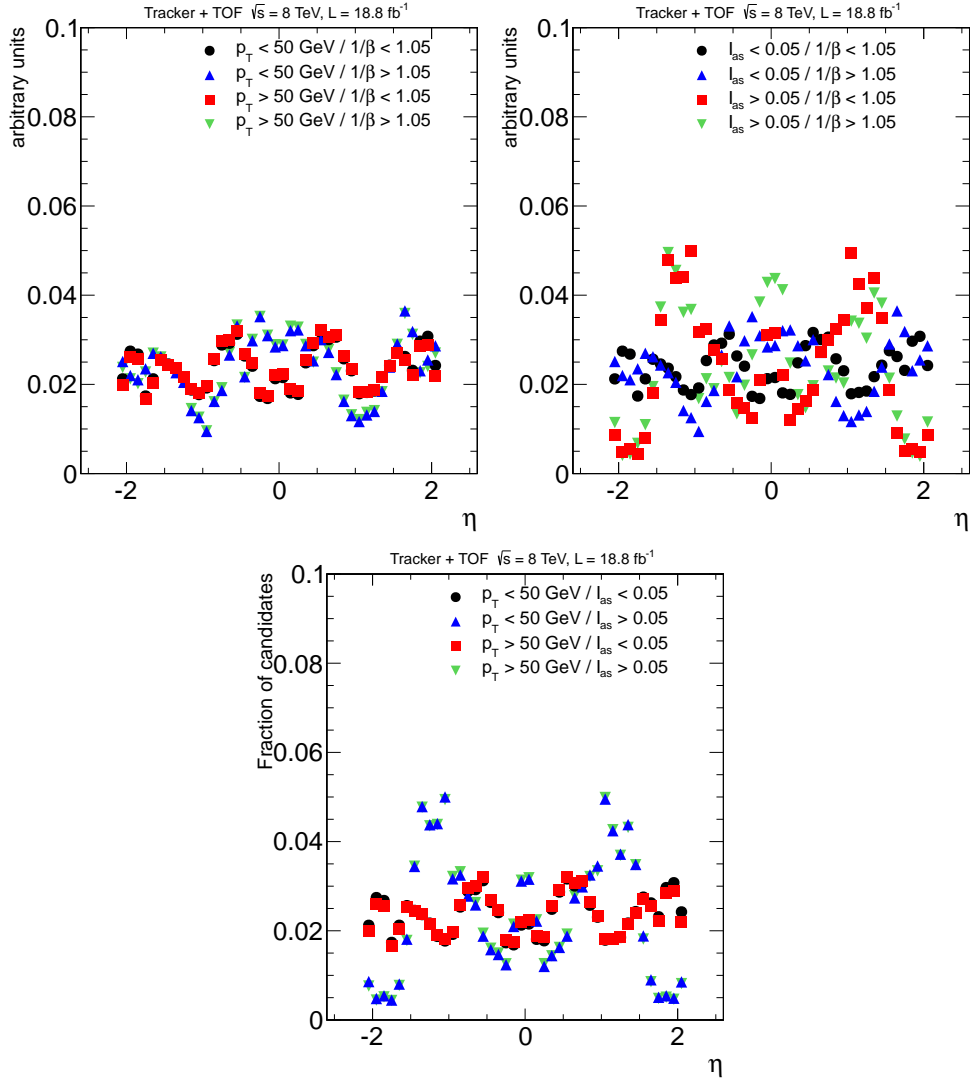
Figure 5.31: Distribution for data of the candidate η for various combinations of being above or below selection thresholds of 50 GeV for p_T, 1.05 for β^{-1}, and 0.05 for I_{as}. Top left: Combinations of flipping p_T and β^{-1} thresholds. Top Right: Combinations of flipping β^{-1} and I_{as} thresholds. Bottom: Combinations of flipping p_T and I_{as} thresholds. For all plots the variable not flipped is required to be below the threshold.

A region for determining the I_h distribution. Before the distribution is found, weight factors are attached to all of the candidates in the A region so that the η distribution of candidates in the A region matches that observed in the G region as necessitated by the conversation above. Next, a value of m_{ik} is found for each bin of the reweighted I_h distribution. A value of A_i is then found by summing m_{ik} over k. The predicted number of background candidates in the signal region for a given j–k bin in the $p - dE/dx$ plane, D_{ijk}, is then found via the relation

$$D_{ijk} = (A_i \times F_i \times G_i/E_i^2) \times (n_{ij}/G_i) \times (m_{ik}/A_i) = F_i \times n_{ij} \times m_{ik}/E_i^2 \quad (5.11)$$

The predicted candidates in D_{ijk} are taken to have a mass equal to the mass coming from Equation 5.1 with the p and I_h values determined by the bin that j and k represent in the p and I_h distributions, respectively. The mass distribution for the ith pseudo-experiment is then found by summing D_{ijk}, with its representative mass, over j and k.

The value in each mass bin is then found as the average of the value in all the pseudo-experiments. The statistical error is taken as the standard deviation of the values from the pseudo-experiments. The prescription for determining the predicted background mass shape was done by another scientist working on CMS and is simply reproduced here.

As the β^{-1} value of candidates is not currently used in the mass estimation the predicted and observed mass spectrums in the $\beta^{-1} < 1$ region can be found by only changing the groups that the candidates be drawn from be the regions with a prime (e.g. A'). Using the $\beta^{-1} < 1$ region allows for checking the predicted mass distribution in a background dominated region even when applying tight thresholds. The predicted and observed mass distributions are shown in Figure 5.32 with both loose and tight thresholds on the selection variables.
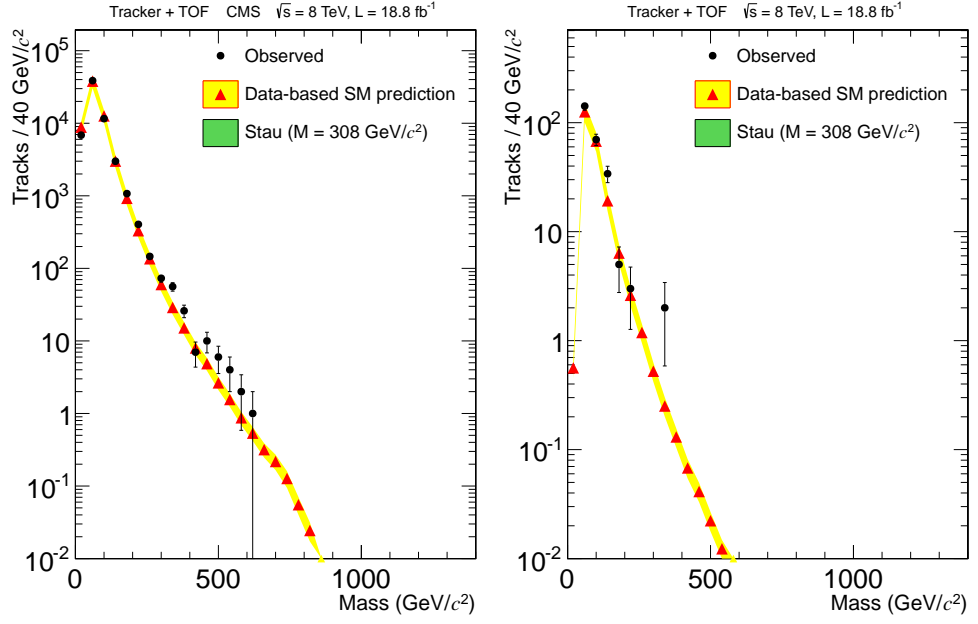
Figure 5.32: Observed and predicted mass spectrum for candidates in the D' region in the *muon+track* subanalysis. Left: Thresholds of $p_T > 55$ GeV, $I_{as} > 0.1$ and $1/\beta < 0.95$. Right: Thresholds of $p_T > 85$ GeV, $I_{as} > 0.1$ and $1/\beta < 0.8$. The error bands are only statistical.

The systematic uncertainty on the background prediction for the $muon+track$ analysis is evaluated by using the multiple different predictions possible when using the three dimensional variation of the $ABCD$ method. As mentioned above, in addition to the chosen prediction of $A \times F \times G/E^2$, there are six more equations that can be used to predict the amount of background in the signal region. Of the six, three have small statistical uncertainty. Those three are $A \times H/E$, $B \times G/E$, and $F \times C/E$. The chosen prediction includes the bin where all the variables are below the threshold and the three where exactly one threshold is passed. The three additional predictions include the group where all the thresholds are failed, one of the bins where exactly one threshold is passed, and one of the bins where exactly two of the thresholds are passed.

The three additional background predictions each test the correlation between two of the three selection variables. Here the prediction $A \times H/E$ is used as an example but the argument is the same for the other predictions. Comparing $A \times H/E$ with the chosen background prediction of $A \times F \times G/E^2$ it can be seen that the difference is replacing $F \times G/E$ with H. The E group fails all three thresholds, the F and G groups pass only the β^{-1} and p_T thresholds, respectively, and the H group passes the β^{-1} and p_T thresholds but not dE/dx. If β^{-1} and p_T are uncorrelated then the equation $F \times G/E$ should predict the number of candidates in the H region. So a comparison of the two predictions will test how well the assumption that the variables are uncorrelated works. Likewise, the prediction $B \times G/E$ ($F \times C/E$) tests for possible correlation between p_T and dE/dx (β^{-1} and dE/dx).

The number of predicted events coming from the four predictions is shown in Figure 5.33. The spread of the four predictions is used to extract the systematic through the Equation 5.3 with N=4. The statistical and systematic uncertainties

are shown in Figure 5.34. From the last plot and the agreement in the predicted mass spectrum a conservative systematic uncertainty of 20% is taken.

5.7.3   Prediction for *track only* analysis

The prediction for the *track only* analysis is the same as the *muon+track* analysis except only the variables p_T and I_{as} are used in a traditional two dimensional ABCD method. The signal region, D, is predicted as $H \times B/F$ (see Table 5.7). The systematic uncertainty on the background prediction for the *track only* analysis is taken as the same as in the *muon+track* analysis.

5.7.4   Prediction for *multiple charge* analysis

The *multiple charge* analysis employs a two dimensional ABCD method using the variables β^{-1} and I_{as} without a mass requirement. No mass requirement is applied as the mass estimation assumes Q=1e and the large amount of saturation of the tracker readout prevents correcting for the charge. No p_T requirement above the one applied at preselection is used in the *multiple charge* analysis becuase the reconstructed p_T of multiply charged particles is underestimated by a factor of 1/Q. This makes the separation between signal and background in the p_T spectrum small and a higher threshold would remove similar fractions of signal and background.

The signal region, D, is predicted as $H \times C/G$ (see Table 5.7). The background prediction is checked by using the control region with $\beta^{-1} < 1$ as was done for the *muon only* analysis. Figure 5.35 shows the predicted and observed number of tracks for various β^{-1} and I_{as} thresholds in the D' region, good agreement is observed.
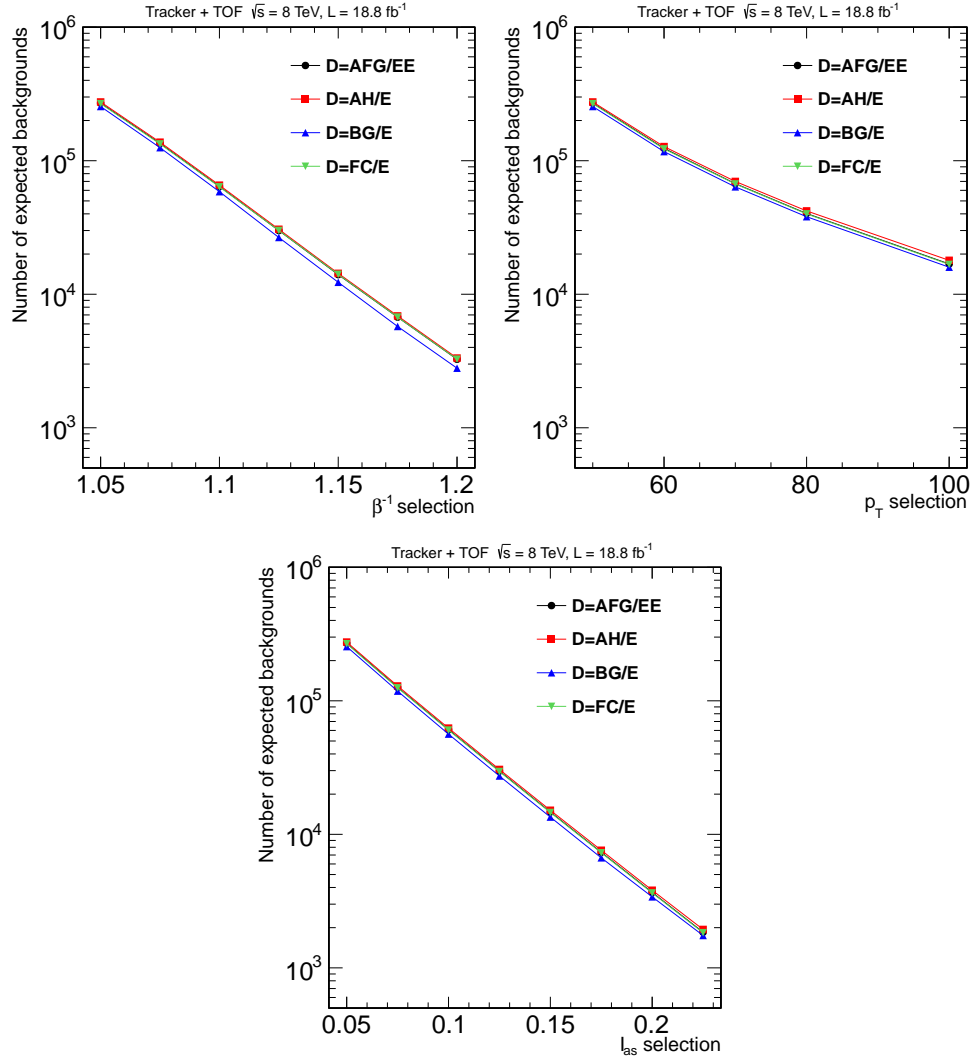
Figure 5.33: Number of predicted candidates from four different background predictions. Top Left: p_T and I_{as} threshold of 50 GeV and 0.05, respectively. Threshold on β^{-1} set by X-axis. Top Right: Threshold on β^{-1} and I_{as} of 1.05 and 0.05, respectively. Threshold on p_T set by X-axis. Bottom: Threshold on β^{-1} and p_T of 1.05 and 50 GeV, respectively. Threshold on I_{as} set by X-axis.
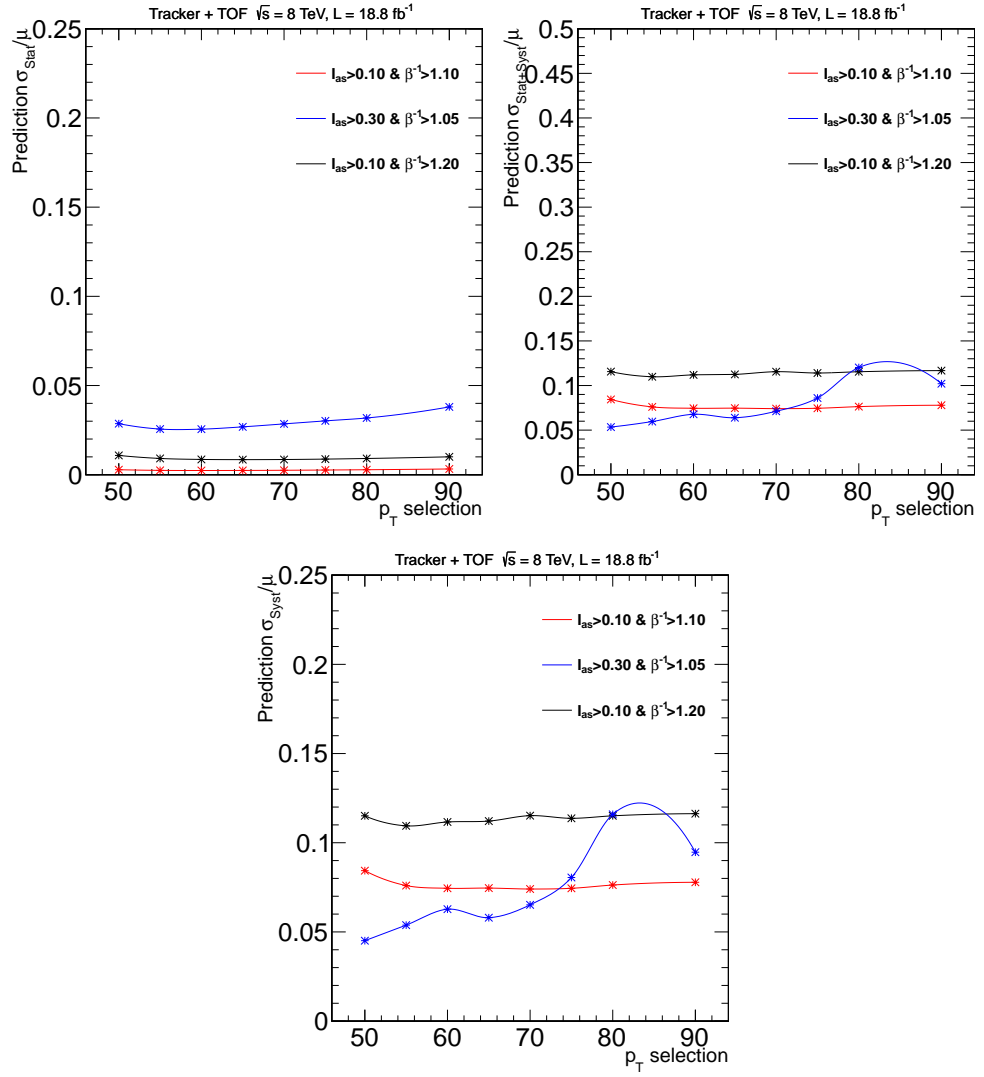
Figure 5.34: Calculation of uncertainty in the *muon+track* analysis. Left: Ratio of the quadratic mean of the statistical uncertainties of the four background estimations to the mean of these estimations vs the p_T threshold. Middle: ratio of the variance to the mean of the four background estimations vs p_T. Right: ratio of the square root of the difference between the variance and the quadratic mean of the statistical uncertainties of the four possible background estimations and the mean vs p_T.
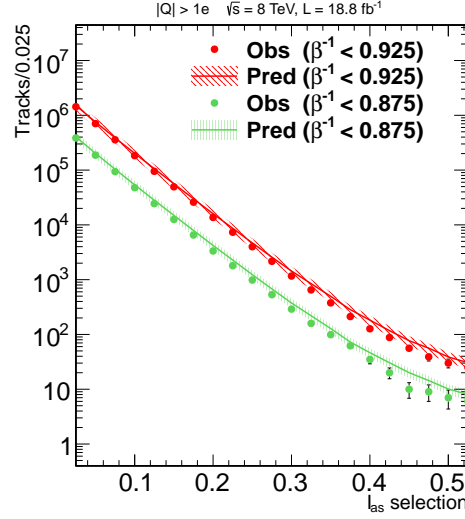
Figure 5.35: Predicted and observed number of events in the D' region for different β^{-1} thresholds with the X-axis indicating the I_{as} threshold.

The systematic uncertainty for the *multiple charge* analysis is determined by the same method as the *muon only* analysis replacing p_T for I_{as}. Two additional predictions are made using the tracks in the $\beta^{-1} < 1$ region. Figure 5.36 shows the predicted number of tracks for various β^{-1} and dE/dx thresholds for the three predictions.

The spread in the three predictions is then used to determine the systematic uncertainty through Equation 5.3 with N=3. Fig. 5.37 shows the variation of the statistical and systematic uncertainties as a function of the I_{as} threshold. From the last plot a 20% systematic uncertainty is taken on the background estimate for the *multiple charge* analysis.
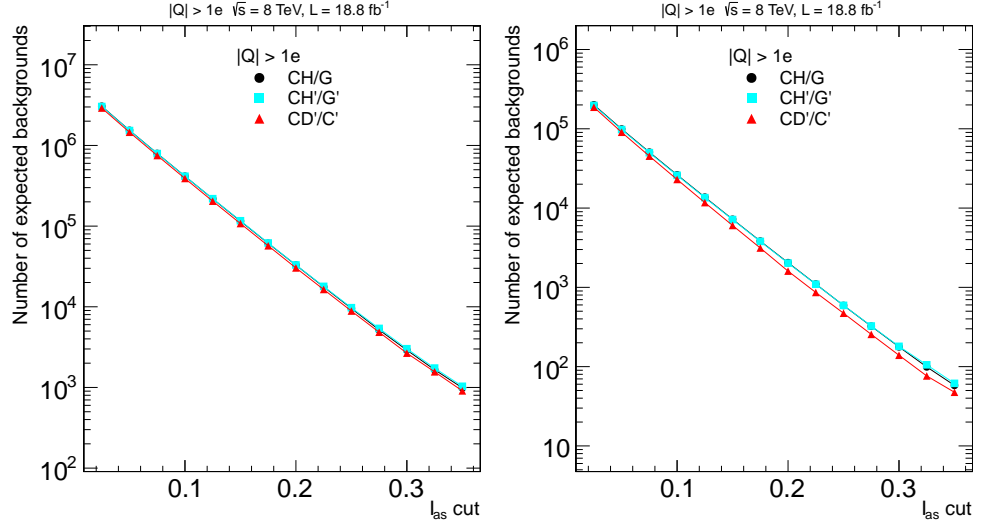
Figure 5.36: Distribution of the number of predicted events and their statistical error computed for the *multiple charge* analysis using different regions for two values of the $1/\beta$ threshold. The I_{as} threshold is defined by the x-axis. Left column: $1/\beta > 1.05$ (< 0.95 for low $1/\beta$ regions). Right column: $1/\beta > 1.15$ (< 0.85 for low $1/\beta$ regions).
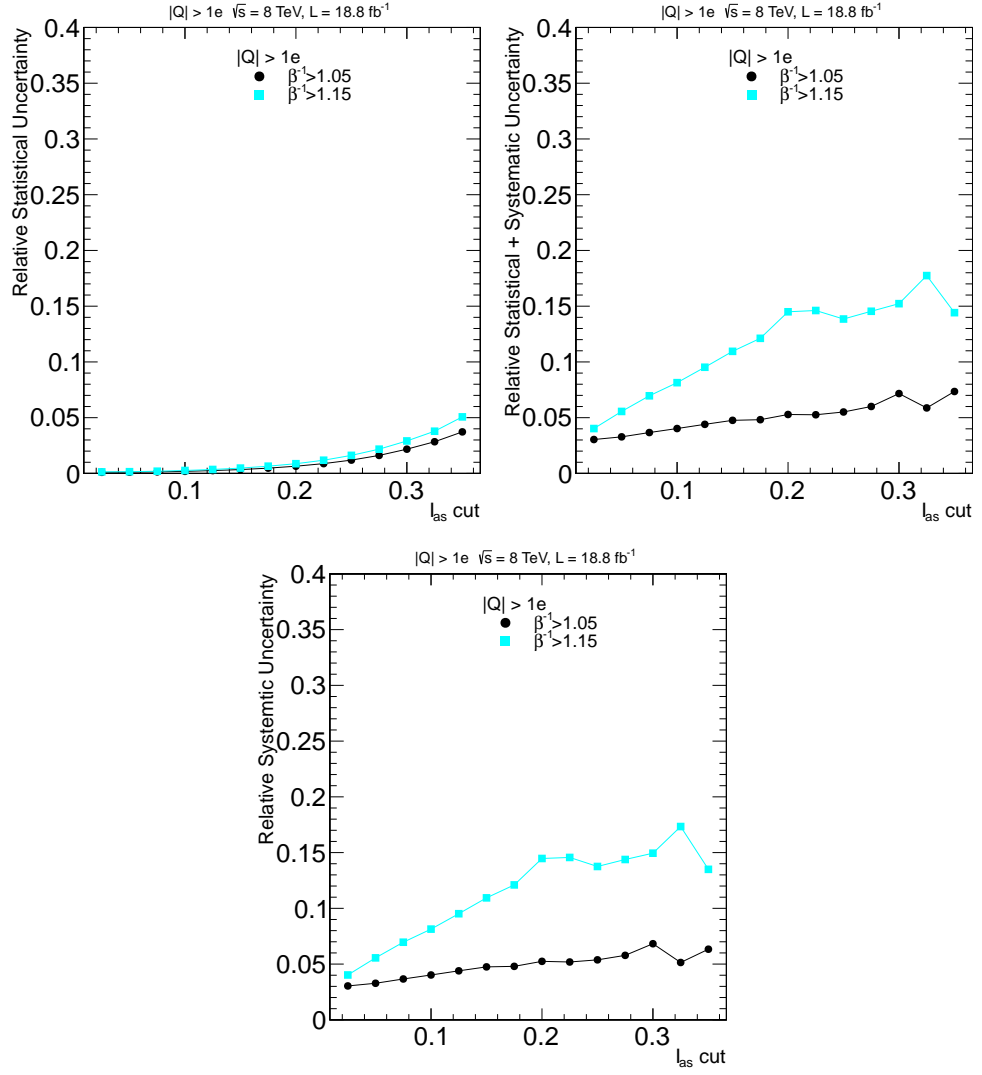
Figure 5.37: Calculation of uncertainty in the *multiple charge* analysis. Left: Ratio of the quadratic mean of the statistical uncertainties of the three background estimations to the mean of these estimations vs the I_{as} threshold. Middle: ratio of the variance to the mean of the three background estimations vs I_{as}. Right: ratio of the square root of the difference between the variance and the quadratic mean of the statistical uncertainties of the three possible background estimations and the mean vs I_{as}.

5.8 Statistical Technique

CMS has a Statistics Committee which provides advice on statistics issues as well tools which can be used to perform statistical calculations. Tools developed in the search for the Higgs Boson were used in this analysis to get the significance of any observed excess and if no excess is observed to place bounds on the signal cross-section. More information about the tools and statistical technique can be found in [3].

One of the tools calculates the significance of a signal by taking in the predicted background with its uncertainty and the observed data. The tool calculates a test statistic, q_0 comparing the likelihood that observed data came from background only or signal plus background. Then the probability of observing a test statistic at least as large as q_0 is found. The smaller the probability the less likely the observed data came from background only. The probability is returned in the form of a one-sided Gaussian sigma. For a given sigma, x, the probability p is found from Equation 5.12,

$$p = \int_x^\infty \frac{1}{\sqrt{2\pi}} e^{\frac{-x^2}{2}} \mathrm{dx}. \tag{5.12}$$

the function being integrated over is a normalized gaussian with unit variance. Particle physics has a convention that one claims a discovery when the significance is greater than five sigma and evidence when it is greater than three. A five sigma discovers means that there is a one in 3.5 million probability that observed data come from background only.

This tool can also be used find the expected reach of the analysis. The expected reach of the analysis is defined as the signal cross-section for which there is a 50% chance of being able to claim a discovery. This is of particular interest when designing the analysis to determine optimum thresholds on the

selection variables.

Another tool returns the expected and observed limits on the signal cross-section. The tool is passed the different sources of background with their uncertainties, the signal efficiency with its uncertainty, and finally the integrated luminosity with its uncertainty. The tool then proceeds to calculate the cross section limits with a hybrid CLs approach [45] using a profile likelihood technique [46] with the predicted background, signal efficieny, and integrated luminosity as nuisance parameters using lognormal pdfs [43, 44]. The uncertainty on the predicted background is discussed in Section 5.7 and the signal efficiency uncertainty is discussed in Section 5.10. The uncertainty on integrated luminosity is 4.4% [47].

5.9   Cut Optimization

All of the analyses calculate the predicted and observed number of tracks for numerous different sets of thresholds on the selection variables. Some of the sets of thresholds have only a small number of candidates in the control regions which are used to make the background prediction. Low statistics in the control region can make the background prediction unreliable and potentially biased if signal candidates make up a large portion of the control region. To prevent this, only thresholds that have at least 25 candidates in all control regions are considered.

The number of predicted and observed events for a few sets of thresholds for the *muon only* and *muon+track* analyses are shown in Figure 5.38. Similar plots are shown for the *track only* and *multiple charge* analyses in Figure 5.39. The observed and predicted mass spectrum with loose thresholds is shown in Figure 5.40 for the *muon+track* and *track only* analyses.
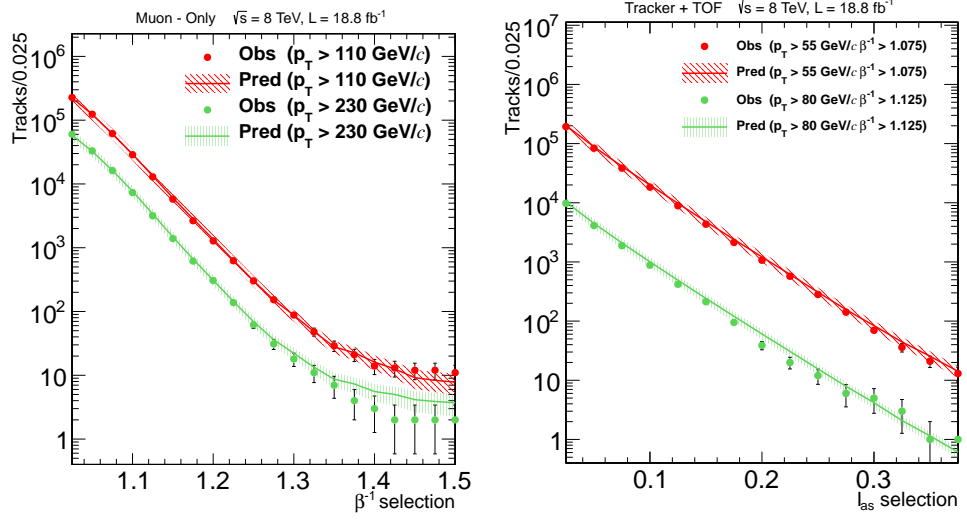
Figure 5.38: Number of predicted and observed events for two different thresholds. Left: For the *muon only* analysis. Threshold for β^{-1} set by X-axis. Right: For the *track only* analysis. Threshold for I_{as} set by X-axis.
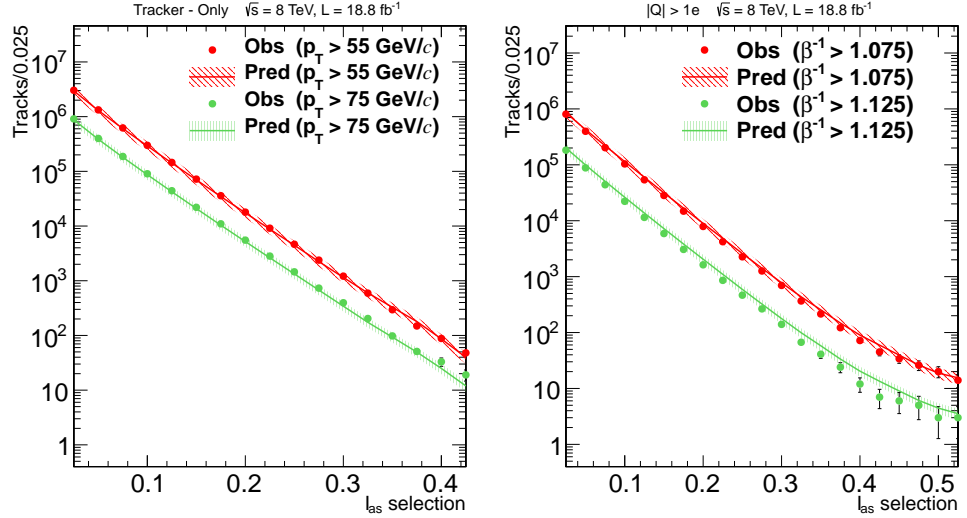
Figure 5.39: Number of predicted and observed events for two different p_T thresholds. Threshold for I_{as} set by X-axis. Left: For the *multiple charge* analysis. Right: For the *track only* analysis.
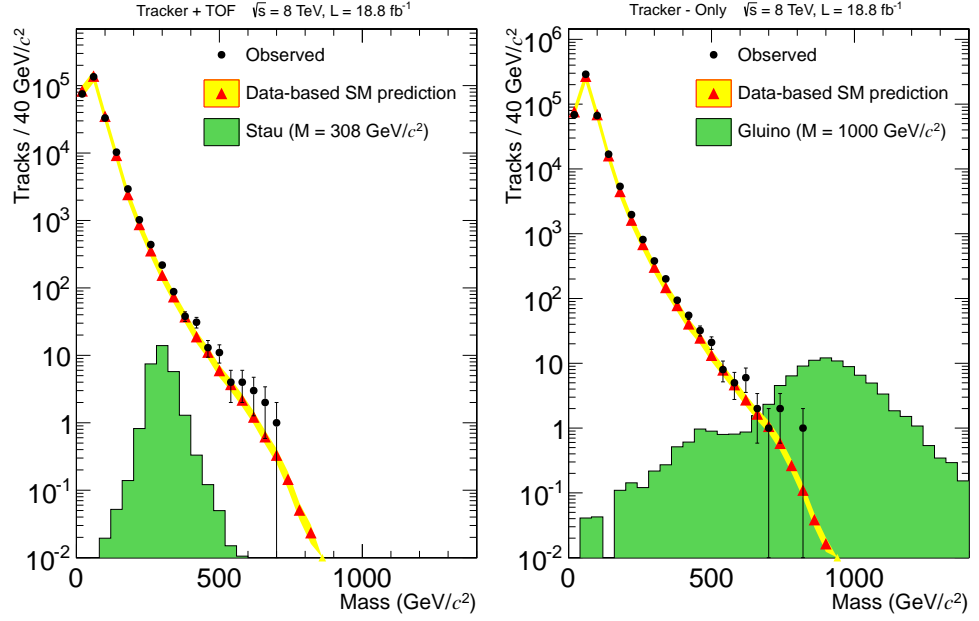
Figure 5.40: Observed and predicted mass spectrum for candidates in the *D* region with loose thresholds. Left: For the *muon+track* analysis with thresholds of $p_T^{cut} > 55$ GeV, $I_{as} > 0.05$ and $1/\beta > 1.05$. Right: For the *track only* analysis with thresholds of $p_T^{cut} > 55$ GeV and $I_{as} > 0.1$ The error bands are only statistical.

The thresholds on the selection variables are set trying to optimize two quantities, the expected reach and cross-section limit. The two variables give the power of the analysis for two different hypotheses. Expected reach is concerned with the likelihood of finding a signal if it does exist while the expected limit is concerned with excluding the signal if it does not exist.

When optimizing the expected reach it is necessary to be careful not to optimize to a region with very small predicted background at the expense of signal efficiency. The reason is that for very small predicted background it is possible to have a five sigma significance with only one or two observed events. For example, one observed event will give a five sigma significance for a predicted background of 2.87×10^{-7}. However, a single event is not enough to claim discovery of new physics. To protect against this, the definition of the expected reach is modified to be at least as large as the cross-section which is expected to give at least five events, as recommended by the CMS statistics committee.

Most of the time, the two variables agree which of two sets of thresholds is better however in some conditions the variables will disagree. One such case is analyses that have little predicted background and high efficiency for the signal to pass the thresholds on the selection variables. This is the case for high mass samples in the *muon+track* and *track only* analyses.

Once the expected cross-section limit falls below the point where more than 50% of the time zero events would be observed in the background only hypothesis, the expected cross-section limit no longer improves by decreasing the expected background. Any loss of efficiency caused by raising the threshold on the selection variables will cause the expected cross-section limit to be optimized at this cross over point. The cross over occurs at approximately 0.6 predicted events with the uncertainties used in the analyses.

The expected reach continues to improve by making the predicted background smaller until a five sigma significance would be found with fewer than five events. At this point the requirement that at least five events be found for a discovery sets the expected reach. This occurs at approximately 0.1 predicted events.

Thus how low the predicted background can be is set differently when optimizing for one versus the other. When the optimization for the best expected reach is used for these cases, the effect on the expected cross-section limit is usually small as the signal efficiency does not decrease much when raising the thresholds. However when the optimization from the expected limit is used, the expected reach can get noticably worse as more events are needed to claim a discovery. For this reason, combined with the fact that the main goal of these analyses is to discover new physics, priority is given to the expected reach when trying to optimize the threshold values.

The thresholds are optimized in a two step process. First the set of thresholds which give the best expected reach for each mass/model point is determined. However, this leads to numerous different selections being used which are often very similar and give about the same discriminating power. This is troublesome for two reasons.

The first is that using multiple different selections increases the risk of a statistical fluctuation of the background causing a spurious signal. To account for this a correction must be applied to the obtained local significance such that the value is correctly set to the probability of finding the signal in any of the used sets of thresholds. This means that the global expected reach could be improved by using fewer sets of thresholds even if it comes with the price of making the local expected reach worse.

The second reason is that the analysis becomes much more difficult to un-

derstand as there are multiple different sets of thresholds being used as well as multiple predicted and observed events. This complexity brings with it little additional gain in the expected reach or cross section limit and unnecessary complexity is not something that is desired in an analysis. No matter how robust an analysis is, if it can not be understood by others then it can not have an impact on the scientific community at large.

For these reasons a second step is taken attempting to make the thresholds the same for the various mass/model points. If the harm to mass/model points in having the same thresholds is too large then using more than one set of thresholds is possible. However this was found not to be necessary and a single cut value is used in all analyses. The final thresholds used as well as the number of observed and predicted events is shown in Table 5.9. The predicted and observed mass distributions for the *track only* and *muon+track* analyses with the final thresholds are shown in Figure 5.41.

5.10   Signal Efficiency Systematic Uncertainties

The signal efficiency for all the analyses is determined from MC. To assess how well MC matches data, numerous studies were performed using control samples.

5.10.1   Trigger Efficiency Uncertainty

The uncertainty on the muon trigger efficiency can come from numerous different effects. A 5% difference in the muon trigger efficiency has been observed between data and MC [48]. An additional uncertainty important to slow moving particles is the timing synchronization in the muon system. As an HSCP arrives in the muon system closer to the switching of the assigned bunch crossing window, a

Table 5.9: Results of the final selections for predicted background and observed number of events. Results for representative mass cuts are given for the *track only* and *muon+track* analyses. Uncertainties are statistical and systematic.

	Selection criteria				Numbers of events $\sqrt{s} = 8$ TeV	
	p_T (GeV/c)	I_{as}	β^{-1}	Mass GeV/c^2	Pred.	Obs.
muon only	> 230	-	> 1.40	-	5.6 ± 2.9	3
muon+track	> 70	> 0.125	> 1.225	> 0	43.5 ± 8.7	42
				> 100	5.6 ± 1.1	7
				> 200	0.56 ± 0.11	0
				> 300	0.090 ± 0.02	0
track only	> 70	> 0.4	—	> 0	32.5 ± 6.5	41
				> 100	26.0 ± 5.2	29
				> 200	3.1 ± 0.6	3
				> 300	0.55 ± 0.11	1
				> 400	0.15 ± 0.03	0
$|Q| > 1e$	—	> 0.500	> 1.200	—	0.52 ± 0.11	1
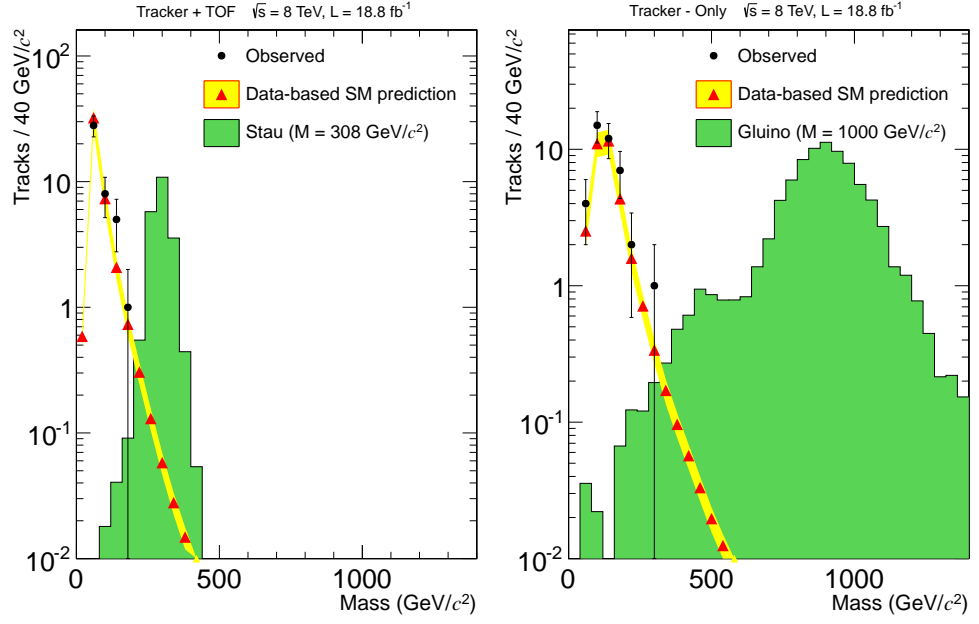
Figure 5.41: Observed and predicted mass spectrum for candidates in the D region in the *muon+track* analysis with the tight selection. The error bands are only statistical. Left: For the *muon+track* analysis. Right: For the *track only* analysis.

discrepancy in the modeling of the timing synchronization in MC would have a larger effect than for SM particles. The timing of the trigger system is set at the local system level with the exact segmentation differing between the three muon subsystems.

To determine the size of the effect, the average and RMS of the synchronization of the trigger timing components with respect to the LHC clock for each subsystem was measured. A normalized guassian distribution was then created for each subsystem with the mean and width equal to the measured values. Then, each trigger timing component was assigned a shift value drawn from the gaussian representing the muon subsystem to which it belongs. The simulation of the detector electronics was then repeated for signal MC samples, with the time of the simulated hits in the detector shifted by the value associated with the portion of the detector the hit is in. Then the reconstruction and trigger simulation steps were redone. Multiple samples were evaluated including the highest mass samples which would have the largest effect. The largest efficiency change was 4% and this is taken as the uncertainty for all samples that use the muon trigger.

Also contributing to the trigger uncertainty is the accuracy of PFMET in the trigger in MC. The uncertainty on the PFMET is dominated by the uncertainty on the measurement of jet energies. A group within CMS studies the agreement between data and MC for jets. For both data and MC, the group releases corrections to the energy scale of jets (JEC) which can be applied after reconstruction to give the best measurement of the energy of the jet. The corrections come with corresponding uncertainties (JEU). The jets used for calculating the PFMET at trigger level are not corrected.

To determine the systematic uncertainty, the jets in the signal MC are adjusted by both the JEC and JEU and the MET is recalculated. The jets are

corrected by the MC JEC and then by the inverse of the data JEC. This results in the MC jets having the same properties as uncorrected jets in data. The JEU are applied by decreasing the energy of each jet by its uncertainty. The JEC are found to increase the efficiency slightly while the JEU decrease it by approximately 1%. Conservatively, no scale factor is applied on the trigger efficiency and a 1% uncertainty is taken on the MET trigger for all samples.

The total systematic uncertainty on trigger efficiency is found by combining the above effects. The muon trigger is dominant for all samples except for the charge suppressed samples where the muon trigger does not have any efficiency. For those samples, the trigger efficiency uncertainty comes only from the MET uncertainty.

5.10.2 Uncertainty on Selection Variables

The uncertainty on the β^{-1} measurement is studied using muons from the decay of Z bosons. Muons are required to pass a tight selection provided by the muon POG to give a pure muon sample. Additionally the event must have a pair of oppositely charged muons with an invariant mass of $M_Z \pm 10\text{GeV}$. Only the two muons forming the combination are used. If more than one such pair exists, the pair with invariant mass closest to M_Z is used. An uncertainty of 0.005 is taken on the β^{-1} measurement from the disagreement between data and MC. This uncertainty is evaluated separately for all samples and is found to be less than 7% for all considered signals.

The uncertainty due to the p_T measurement is determined by varying the $1/p_T$ value by a prescription from the muon POG [48]. For the *muon only* analysis the $1/p_T$ of the muon system track is shifted up by 10%, this means that the p_T will decrease. For the other analyses the $1/p_T$ of the inner track is adjusted by the

Equation

$$\frac{1}{p_T'} = \frac{1}{p_T} + \delta_{K_T}(q, \phi, \eta) \tag{5.13}$$

$$\delta_{K_T}(q, \phi, \eta) = A + B\eta^2 + qC\sin(\phi - \phi_0) \tag{5.14}$$

where A = 0.236 TeV^{-1}, B = -0.135 TeV^{-1}, C = 0.282 TeV^{-1}, and ϕ_0 = 1.337. The shifts were found to have a less than 10% effect on the efficiency to pass the final selection for all signals.

The effect of the uncertainty on dE/dx was evaluated with low momentum protons. Protons with p less than about 2 GeV will have speed appreciably lower than the speed of light and thus will appear similar to signal candidates. A comparison of data and MC yields an uncertainty of 0.05 on I_{as} and 5% on I_h. When propagated to the final selection for singly charged particles, these uncertainties give efficiency changes of less than 13% for low mass samples and less than 7% for masses above 200 GeV/c^2. Multiply charged particles have sufficient separation between signal and background that the uncertainty is negligible.

5.10.3 Other Uncertaintis on Signal Efficiency

The systematic uncertainty on muon [48] and track [49] reconstruction were both found to be less than 2%. A 1% uncertainty recommended by the muon POG is applied on the correction factors used in the *muon only* analysis described in Section 5.6.5.

The uncertainty on the number of proton-proton collisions per bunch crossing is found by varying by 6% the proton-proton cross-section used to determine the weights for MC events (see end of Sec. 5.3). This leads to an uncertainty of less

than 4% for all samples.

Multiply charged particles deposit a large amount of energy in the calorimeter and if the particle does not have enough energy it may come to a stop in the calorimeter. This is particularly important for high charge, low mass samples, because if the particle has enough energy to pass through the calorimeter then it will be travelling at a high speed and be unlikely to pass the threshold on β^{-1}. Uncertainty on the amount of detector material, determined mostly by the HCAL, affects the number of HSCP that will stop. There is a conservative 5% uncertainty on the material budget as measured by energy loss of cosmic ray muons passing through CMS [50]. Shifting the material density by this amount for a few signal samples has at most a 20% effect. This 20% uncertainty is conservatively taken for all multiply charged samples.

5.10.4 Total Signal Efficiency Uncertainty

The total systematic uncertainty for each signal point is found by adding the above effects in quadrature. Figure 5.42 shows the different sources of signal efficiency systematic uncertainty and their quadratic sum for the various signal models considered in the *muon only* analysis. Figure 5.43 and 5.44 shows the same for the *muon+track* analysis for stau and $R - hadron$ models, respectively. Figure 5.45 shows the sources of systematic uncertainty for a few of the samples in the *track only* and *multiple charge* analyses.

The total signal efficiency uncertainty for all considered models is shown in Figure 5.46 for the four analyses. The signal efficiency uncertainty used for each signal point is what is shown in this figure. For all analyses except for the *multiple charge* analysis, the uncertainty is less than 15% for all signal points and less than 10% for a large majority of signal points. The large uncertainty on the amount

of detector material results in the uncertainty for the multiply charged particles to be between 20% and 30%.

5.11   Final Results

No large excess was observed over the expected background for any of the used selection points. The largest excess is 1.7 sigma observed in the *track only* analysis with a mass cut of 190 GeV. Considering the numerous different mass cuts used in the *muon+track* and *track only* analysis this is consistent with a background only interpretation. Therefore, limits are placed on the production rate of various models of new physics. The statistical method of determining the limits is discussed in Section 5.8. Figure 5.47 shows the cross-section limit at 95% confidence level (CL) in the analyses for all considered models.

The CMS results for all the analyses except for *muon only* combine the 8 TeV data collected in 2012 with 7 TeV data collected in 2011. The combined result places limits on the relative signal strength, σ/σ_{th}. The 7 TeV results are simply added here without further description. The limit on the relative cross-section for the analyses is shown in Figure 5.48. For the *muon only* analysis the limit on signal strength uses only 8 TeV data.

Table 5.10 has the observed and expected limits for all the signal points in the *muon only* analysis as well as the signal efficiency. Table 5.11 shows the same for the *muon+track* analysis. Tables 5.12 and 5.13 show the efficiency and observed and expected limits for some of the signal points in the *track only* and *multiple charge* analyses, respectively.

Table 5.10: Summary table of results for all the considered signal points for the *muon only* analysis. The signal efficiency and observed and expected limits on the cross section (in pb) at $\sqrt{s} = 8$ TeV are presented. Also the observed and expected limits on the signal strength at $\sqrt{s} = 8$ TeV.

Mass	$\sigma(pb)$			$\mu = \sigma/\sigma_{TH}$	
(GeV)	$\sqrt{s} = 8TeV$			$\sqrt{s} = 8TeV$	
	Eff.	Obs.	Exp.	Obs.	Exp.
Gluino 100% $\tilde{g}g$ - *muon only* analysis					
300	0.05	0.0075	0.007	7.3×10^{-5}	6.8×10^{-5}
400	0.07	0.0057	0.005	3.1×10^{-4}	2.7×10^{-4}
500	0.09	0.0044	0.0037	0.00098	8.4×10^{-4}
600	0.10	0.0028	0.0034	0.0022	0.0026
700	0.10	0.0027	0.0032	0.0063	0.0075
800	0.11	0.0025	0.003	0.017	0.02
900	0.11	0.0024	0.0029	0.041	0.049
1000	0.11	0.0022	0.003	0.094	0.12
1100	0.11	0.0025	0.003	0.25	0.3
1200	0.10	0.0026	0.0032	0.6	0.73
1300	0.10	0.0027	0.0032	1.4	1.7
1400	0.09	0.003	0.0036	3.4	4.1
1500	0.09	0.0031	0.0037	7.9	9.5
Gluino 50% $\tilde{g}g$ - *muon only* analysis					

Table 5.10 – *Continued from previous page*

| Mass | $\sigma(pb)$ | | | $\mu = \sigma/\sigma_{TH}$ | |
| (GeV) | $\sqrt{s} = 8TeV$ | | | $\sqrt{s} = 8TeV$ | |
	Eff.	Obs.	Exp.	Obs.	Exp.
300	0.06	0.0065	0.006	6.3×10^{-5}	5.8×10^{-5}
400	0.08	0.0048	0.0041	2.6×10^{-4}	2.2×10^{-4}
500	0.10	0.0037	0.0032	8.3×10^{-4}	7.2×10^{-4}
600	0.11	0.0024	0.0028	0.0019	0.0022
700	0.12	0.0022	0.0026	0.0051	0.0062
800	0.13	0.0021	0.0025	0.014	0.017
900	0.14	0.002	0.0024	0.034	0.041
1000	0.13	0.002	0.0024	0.085	0.1
1100	0.13	0.002	0.0024	0.2	0.24
1200	0.13	0.0021	0.0025	0.48	0.58
1300	0.12	0.0022	0.0026	1.1	1.4
1400	0.12	0.0023	0.0028	2.6	3.2
1500	0.11	0.0024	0.003	6.2	7.5
Gluino 10% $\tilde{g}g$ - *muon only* analysis					
300	0.06	0.0058	0.0054	5.7×10^{-5}	5.3×10^{-5}
400	0.09	0.0042	0.0037	2.3×10^{-4}	2.0×10^{-4}
500	0.11	0.0034	0.0029	7.6×10^{-4}	6.6×10^{-4}
600	0.13	0.0022	0.0026	0.0017	0.002
700	0.14	0.0019	0.0023	0.0044	0.0055
800	0.15	0.0019	0.0022	0.012	0.015
900	0.15	0.0017	0.0021	0.029	0.036
1000	0.15	0.0018	0.0021	0.074	0.089

Table 5.10 – *Continued from previous page*

| Mass | $\sigma(pb)$ | | | $\mu = \sigma/\sigma_{TH}$ | |
| (GeV) | $\sqrt{s} = 8TeV$ | | | $\sqrt{s} = 8TeV$ | |
	Eff.	Obs.	Exp.	Obs.	Exp.
1100	0.15	0.0018	0.0021	0.18	0.21
1200	0.15	0.0018	0.0022	0.41	0.51
1300	0.14	0.0019	0.0023	0.97	1.2
1400	0.14	0.002	0.0024	2.3	2.8
1500	0.13	0.0021	0.0026	5.3	6.5
Stop - *muon only* analysis					
100	0.01	0.073	0.063	1.4×10^{-4}	1.2×10^{-4}
200	0.02	0.016	0.014	8.9×10^{-4}	7.8×10^{-4}
300	0.05	0.0052	0.0066	0.0027	0.0034
400	0.08	0.0035	0.0042	0.01	0.012
500	0.10	0.0027	0.0033	0.032	0.039
600	0.12	0.0022	0.0027	0.09	0.11
700	0.14	0.002	0.0024	0.25	0.3
800	0.15	0.0017	0.0021	0.6	0.75
900	0.17	0.0016	0.002	1.5	1.8
1000	0.18	0.0015	0.0019	3.5	4.4

Table 5.11: Summary table of results for all the considered signal points for the *muon+track* analysis. The signal efficiency and observed and expected limits on the cross section (in pb) at $\sqrt{s} = 8$ TeV. Also the observed and expected limits on the signal strength at $\sqrt{s} = 7+8$ TeV.

Mass (GeV)	Mass Req. (GeV)	$\sigma(pb)$ $\sqrt{s} = 8TeV$			$\mu = \sigma/\sigma_{TH}$ $\sqrt{s} = 7+8TeV$	
		Eff.	Obs.	Exp.	Obs.	Exp.
GMSB Stau - *muon+track* analysis						
100	> 20	0.16	0.0062	0.0063	0.0023	0.0025
126	> 40	0.25	0.0042	0.0042	0.0065	0.0074
156	> 70	0.32	0.0024	0.0017	0.017	0.013
200	> 110	0.41	0.0012	7.7×10^{-4}	0.056	0.031
247	> 150	0.50	8.1×10^{-4}	4.4×10^{-4}	0.15	0.068
308	> 190	0.56	2.8×10^{-4}	2.9×10^{-4}	0.21	0.16
370	> 240	0.60	2.7×10^{-4}	2.6×10^{-4}	0.4	0.38
432	> 290	0.64	2.5×10^{-4}	2.3×10^{-4}	0.92	0.86
494	> 330	0.66	2.5×10^{-4}	2.3×10^{-4}	1.9	1.9
Pair Prod. - *muon+track* analysis						
100	> 20	0.17	0.0056	0.0062	0.099	0.11
126	> 40	0.24	0.0043	0.0044	0.16	0.18
156	> 60	0.28	0.0027	0.0024	0.23	0.21
200	> 100	0.34	0.0013	0.001	0.42	0.26
247	> 140	0.40	0.00099	5.8×10^{-4}	0.85	0.37

Table 5.11 – *Continued from previous page*

Mass (GeV)	Mass Req. (GeV)	$\sigma(pb)$ $\sqrt{s}=8TeV$			$\mu=\sigma/\sigma_{TH}$ $\sqrt{s}=7+8TeV$	
		Eff.	Obs.	Exp.	Obs.	Exp.
308	>190	0.46	3.5×10^{-4}	3.5×10^{-4}	0.66	0.62
370	>240	0.53	3.0×10^{-4}	2.9×10^{-4}	1.4	1.2
432	>280	0.57	2.9×10^{-4}	2.6×10^{-4}	2.5	2.4
494	>330	0.61	2.6×10^{-4}	2.5×10^{-4}	5	4.7
Gluino 50% $\tilde{g}g$ - *muon+track* analysis						
300	>110	0.07	0.0044	0.0041	5.0×10^{-5}	3.1×10^{-5}
400	>190	0.08	0.0021	0.002	9.6×10^{-5}	9.3×10^{-5}
500	>260	0.09	0.0021	0.0016	2.8×10^{-4}	3.1×10^{-4}
600	>330	0.09	0.0018	0.0016	0.0012	0.0011
700	>400	0.09	0.0018	0.0018	0.0037	0.0034
800	>480	0.08	0.0019	0.0019	0.011	0.01
900	>530	0.08	0.0021	0.002	0.031	0.029
1000	>610	0.07	0.0023	0.0023	0.085	0.082
1100	>660	0.06	0.0028	0.0026	0.24	0.23
1200	>710	0.05	0.0034	0.0032	0.69	0.66
1300	>750	0.04	0.0041	0.0039	1.9	1.8
1400	>800	0.03	0.0054	0.0051	5.7	5.3
1500	>830	0.02	0.0069	0.0066	17	16
Gluino 10% $\tilde{g}g$ - *muon+track* analysis						
300	>110	0.14	0.0024	0.0022	2.6×10^{-5}	1.7×10^{-5}
400	>190	0.15	0.0011	0.0011	5.6×10^{-5}	5.1×10^{-5}

Table 5.11 – *Continued from previous page*

Mass (GeV)	Mass Req. (GeV)	$\sigma(pb)$ $\sqrt{s} = 8TeV$			$\mu = \sigma/\sigma_{TH}$ $\sqrt{s} = 7 + 8TeV$	
		Eff.	Obs.	Exp.	Obs.	Exp.
500	> 260	0.16	0.0011	8.7×10^{-4}	1.6×10^{-4}	1.8×10^{-4}
600	> 330	0.17	8.7×10^{-4}	9.1×10^{-4}	6.0×10^{-4}	6.0×10^{-4}
700	> 410	0.16	0.00096	0.001	0.0021	0.0017
800	> 480	0.15	0.0011	0.001	0.0058	0.0057
900	> 540	0.14	0.0012	0.0011	0.017	0.016
1000	> 610	0.12	0.0013	0.0012	0.046	0.045
1100	> 660	0.11	0.0015	0.0014	0.13	0.12
1200	> 710	0.09	0.0018	0.0017	0.37	0.35
1300	> 750	0.07	0.0022	0.0021	1	0.99
1400	> 800	0.06	0.0029	0.0027	2.9	2.8
1500	> 830	0.04	0.0037	0.0035	8.6	8.1
Stop - *muon+track* analysis						
100	> 0	0.06	0.019	0.019	3.0×10^{-5}	2.8×10^{-5}
200	> 0	0.12	0.0088	0.0085	4.0×10^{-4}	2.6×10^{-4}
300	> 20	0.15	0.0068	0.0069	0.0024	0.0019
400	> 80	0.16	0.0039	0.0028	0.0072	0.0055
500	> 140	0.17	0.0022	0.0013	0.019	0.013
600	> 210	0.18	8.8×10^{-4}	9.1×10^{-4}	0.031	0.031
700	> 290	0.17	9.4×10^{-4}	8.8×10^{-4}	0.099	0.094
800	> 370	0.17	0.00097	9.1×10^{-4}	0.29	0.27
900	> 450	0.15	0.0011	0.001	0.84	0.79

Table 5.11 – *Continued from previous page*

Mass (GeV)	Mass Req. (GeV)	$\sigma(pb)$ $\sqrt{s} = 8TeV$			$\mu = \sigma/\sigma_{TH}$ $\sqrt{s} = 7+8TeV$	
		Eff.	Obs.	Exp.	Obs.	Exp.
1000	> 530	0.13	0.0012	0.0012	2.5	2.3
DY Q = 1e - *muon+track* analysis						
100	> 40	0.15	0.0068	0.0069	0.011	0.012
200	> 120	0.36	0.0013	7.7×10^{-4}	0.04	0.019
300	> 190	0.48	3.3×10^{-4}	3.4×10^{-4}	0.06	0.046
400	> 270	0.53	3.0×10^{-4}	2.9×10^{-4}	0.15	0.14
500	> 340	0.56	2.9×10^{-4}	2.8×10^{-4}	0.44	0.41
600	> 400	0.56	2.9×10^{-4}	2.8×10^{-4}	1.2	1.1
700	> 470	0.55	3.0×10^{-4}	2.8×10^{-4}	3.1	3
800	> 530	0.52	3.1×10^{-4}	3.0×10^{-4}	8.1	7.5
900	> 590	0.49	3.3×10^{-4}	3.2×10^{-4}	20	19
1000	> 650	0.45	3.6×10^{-4}	3.4×10^{-4}	49	48

Table 5.12: Summary table of results for some of the considered signal points for the *track only* analysis. The signal efficiency and observed and expected limits on the cross section (in *pb*) at $\sqrt{s} = 8$ TeV. Also the observed and expected limits on the signal strength at $\sqrt{s} = 7 + 8$ TeV.

Mass (GeV)	Mass Req. (GeV)	$\sigma(pb)$ $\sqrt{s} = 8TeV$			$\mu = \sigma/\sigma_{TH}$ $\sqrt{s} = 7+8TeV$	
		Eff.	Obs.	Exp.	Obs.	Exp.
Gluino 50% $\tilde{g}g$ - *track only* analysis						
300	> 100	0.08	0.01	0.01	8.4×10^{-5}	7.3×10^{-5}
500	> 230	0.10	0.002	0.0022	4.6×10^{-4}	4.0×10^{-4}
700	> 360	0.11	0.0015	0.0015	0.003	0.0031
900	> 460	0.09	0.0017	0.0016	0.025	0.025
1100	> 530	0.08	0.0021	0.0019	0.18	0.18
1300	> 540	0.06	0.0028	0.0026	1.4	1.3
1500	> 520	0.04	0.004	0.0039	9.8	9.3
Gluino 10% $\tilde{g}g$ - *track only* analysis						
300	> 100	0.15	0.0055	0.0055	4.6×10^{-5}	4.0×10^{-5}
500	> 240	0.19	0.001	0.0011	2.1×10^{-4}	2.1×10^{-4}
700	> 370	0.19	8.4×10^{-4}	8.1×10^{-4}	0.0018	0.0017
900	> 470	0.17	9.5×10^{-4}	8.9×10^{-4}	0.014	0.014
1100	> 540	0.14	0.0011	0.001	0.1	0.098
1300	> 550	0.11	0.0015	0.0014	0.74	0.68
1500	> 530	0.07	0.0022	0.0021	5.2	5.1

Table 5.12 – *Continued from previous page*

Mass (GeV)	Mass Req. (GeV)	$\sigma(pb)$ $\sqrt{s} = 8TeV$			$\mu = \sigma/\sigma_{TH}$ $\sqrt{s} = 7 + 8TeV$	
		Eff.	Obs.	Exp.	Obs.	Exp.
Gluino Charge Suppressed 10% $\tilde{g}g$ - *track only* analysis						
300	> 130	0.05	0.013	0.013	1.2×10^{-4}	1.1×10^{-4}
500	> 240	0.07	0.0027	0.0028	5.8×10^{-4}	6.4×10^{-4}
700	> 340	0.08	0.0021	0.002	0.0043	0.0044
900	> 400	0.07	0.0022	0.0021	0.035	0.034
1100	> 410	0.06	0.0026	0.0025	0.25	0.24
1300	> 400	0.05	0.0034	0.0033	1.6	1.7
1500	> 340	0.04	0.0045	0.0045	11	11
Stop - *track only* analysis						
200	> 0	0.18	0.005	0.0051	2.9×10^{-4}	2.6×10^{-4}
400	> 60	0.23	0.0058	0.0041	0.0098	0.0076
600	> 190	0.24	0.0024	0.0013	0.075	0.043
800	> 330	0.22	7.3×10^{-4}	7.2×10^{-4}	0.22	0.21
200	> 0	0.05	0.026	0.02	0.0015	0.0011
Stop Charge Suppressed - *track only* analysis						
200	> 0	0.05	0.026	0.02	0.0015	0.0011
400	> 50	0.09	0.015	0.01	0.03	0.023
600	> 170	0.10	0.0055	0.0036	0.18	0.12
800	> 270	0.10	0.0023	0.0019	0.73	0.62
1000	> 360	0.08	0.0019	0.0019	4	3.8

Table 5.13: Summary table of results for some of the considered signal points for the *multiple charge* analysis. The signal efficiency and observed and expected limits on the cross section (in *pb*) at $\sqrt{s} = 8$ TeV. Also the observed and expected limits on the signal strength at $\sqrt{s} = 7 + 8$ TeV.

Mass	$\sigma(pb)$			$\mu = \sigma/\sigma_{TH}$	
(GeV)	$\sqrt{s} = 8TeV$			$\sqrt{s} = 7 + 8TeV$	
	Eff.	Obs.	Exp.	Obs.	Exp.
DY Q = 1e - *multiple charge* analysis					
300	0.34	7.1×10^{-4}	4.8×10^{-4}	0.085	0.06
600	0.47	5.1×10^{-4}	3.5×10^{-4}	2	1.5
900	0.44	5.5×10^{-4}	3.7×10^{-4}	31	22
DY Q = 2e - *multiple charge* analysis					
300	0.47	5.0×10^{-4}	3.5×10^{-4}	0.015	0.011
600	0.58	4.1×10^{-4}	2.8×10^{-4}	0.42	0.29
900	0.53	4.4×10^{-4}	3.0×10^{-4}	6.6	4.7
DY Q = 3e - *multiple charge* analysis					
300	0.32	7.4×10^{-4}	5.2×10^{-4}	0.0096	0.0071
600	0.48	4.9×10^{-4}	3.4×10^{-4}	0.23	0.16
900	0.47	4.9×10^{-4}	3.4×10^{-4}	3.4	2.4
DY Q = 4e - *multiple charge* analysis					
300	0.18	0.0013	9.0×10^{-4}	0.0099	0.0072
600	0.35	6.7×10^{-4}	4.7×10^{-4}	0.17	0.12

Table 5.13 – *Continued from previous page*

Mass (GeV)	$\sigma(pb)$ $\sqrt{s} = 8TeV$			$\mu = \sigma/\sigma_{TH}$ $\sqrt{s} = 7 + 8TeV$	
	Eff.	Obs.	Exp.	Obs.	Exp.
900	0.36	6.5×10^{-4}	4.5×10^{-4}	2.5	1.7
DY Q = 5e - *multiple charge* analysis					
300	0.08	0.0029	0.002	0.015	0.01
600	0.22	0.0011	7.4×10^{-4}	0.18	0.13
900	0.24	0.00099	6.7×10^{-4}	2.4	1.7
DY Q = 6e - *multiple charge* analysis					
300	0.03	0.007	0.0047	0.026	0.018
600	0.13	0.0018	0.0012	0.21	0.15
900	0.15	0.0016	0.0011	2.6	1.9
DY Q = 7e - *multiple charge* analysis					
300	0.01	0.018	0.012	0.049	0.035
600	0.08	0.003	0.0021	0.26	0.19
900	0.10	0.0024	0.0017	3.2	2.2
DY Q = 8E- - *multiple charge* analysis					
300	0.01	0.047	0.032	0.1	0.073
600	0.05	0.0052	0.0035	0.36	0.26
900	0.06	0.0039	0.0027	3.8	2.7

Mass limits are placed on the various models by all analyses. The mass limit is found by where the limit on the relative signal strength crosses one. The *muon only* analysis gives mass limits of 1258, 1283, and 1300 GeV for gluino production

with the fraction, f, of $\tilde{g}g$ set to $f = 100\%$, $f = 50\%$, and $f = 10\%$, respectively. The mass limit on stop production is placed at 853 GeV. The *muon+track* analysis sets a mass limit on gluino production with $f = 50\%$ ($f = 10\%$) of 1224 (1291) GeV. The limit on stop production is placed at 910 GeV. A limit of 435 and 339 GeV is placed on stau production in the GMSB and pair production models, respectively. Drell-Yan production of Q=1e particles has a limit set at 574 GeV.

The *track only* analysis excludes f=10% gluino production for masses below 1320 (1239) GeV in the cloud interaction (charge suppression) model. The mass limit on stop production is placed at 934 (820) GeV for the cloud interaction (charge suppression) model. The *multiple charge* analysis sets limits on Q= 1e, 2e, 3e, 4e, 5e, 6e, 7e, and 8e production at 517, 685, 752, 793, 796, 781, 757, and 737 GeV, respectively.

The mass limits for the various signals and electric charges can be seen in Fig. 5.49 as well as limits from previously published searches by CMS and others. The mass limit obtained with the *multiple charge* analysis for Drell–Yan like production of particles with non-unit charge in the range $1e < |Q| \leq 8e$ can be parametrized as $M^{95\%}(Q) = 404.9 + 154.6|Q/e| - 14.8|Q/e|^2 GeV/c^2$

As can be seen the limits presented here are the most stringent in the world to date. These limits put important constraints on many versions of supersymmetry and the production of multiply charged particles as discussed in Section 2.3. The results also apply to a wide range of other theories not directly considered here that can include the production of long-lived charged particles.

5.12   Conclusion

Four analyses were performed searching for heavy long-lived charged particles in proton-proton collision data collected by CMS. One search only requires the particle be found in the outer muon system allowing it to be sensitive to particles produced neutral and only becoming charged by interacting with the detector. The second analysis looks for particles reconstructed in both the inner tracker and the muon system. This analysis is especially powerful for lepton-like long-lived particles which will always be charged during the entirety of their passage through the CMS detector. The third search only requires particles be found in the inner tracker of CMS making it sensitive to particles becoming neutral before reaching the muon system. The last search is optimized to look for particles with electric charge greater than that of an electron.

The signatures of new long-lived charged particles, long time of flight, high momentum, and large ionization energy loss, are used to separate the signal from the large background of SM particles. A data-driven procedure is used to estimate the SM background in the final selection region. The efficiency for signal particles to be accepted in the selection region is evaluated by numerous studies in control regions. Data are found to agree with the predicted background and limits are placed on the production rates of various models of new physics that predict the existence of long-lived particles. All of the limits are the best produced to date and put important constraints on physics beyond the Standard Model.
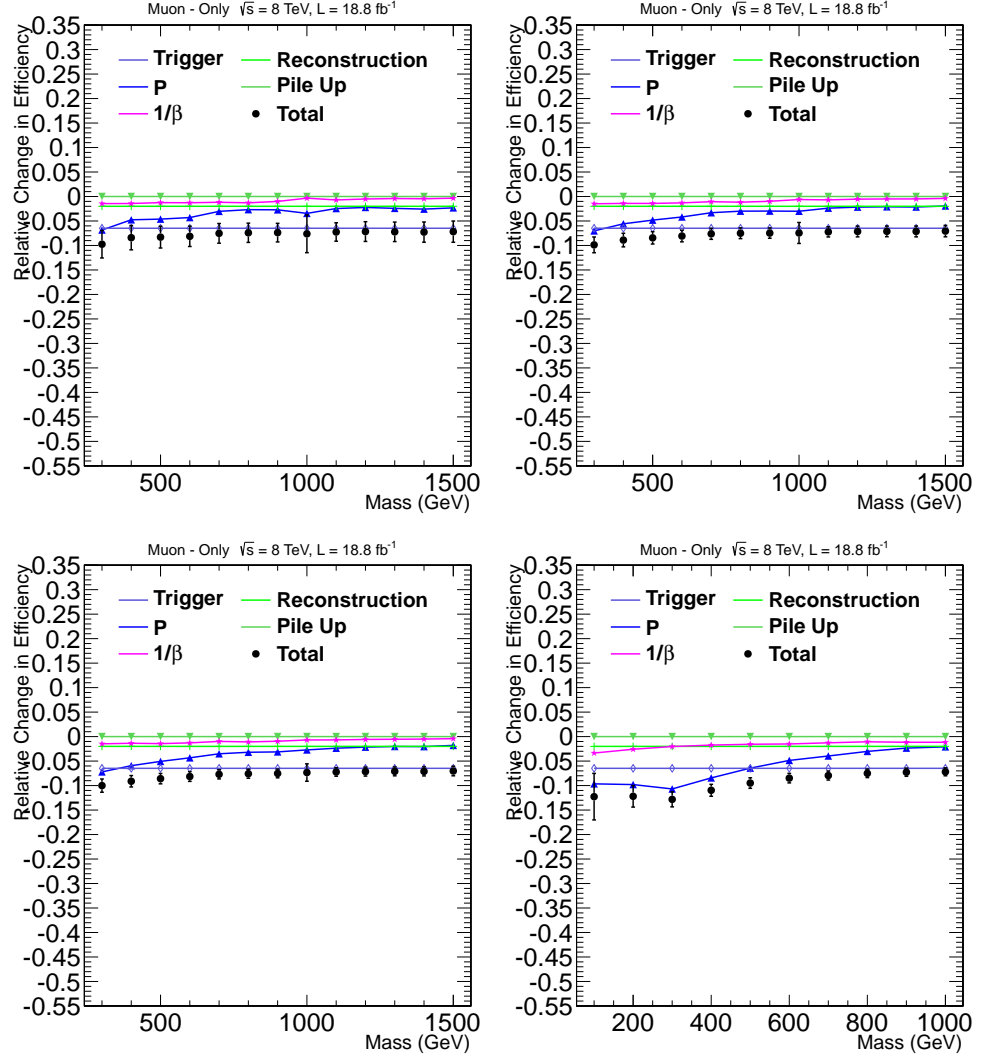
Figure 5.42: Relative signal efficiency change seen for the various sources of uncertainty in the *muon only* analysis. Top row: Gluino with $f = 1.0$ (left) and $f = 0.5$ (right). Bottom row: Gluino with $f = 0.1$ (left) and stop (right)
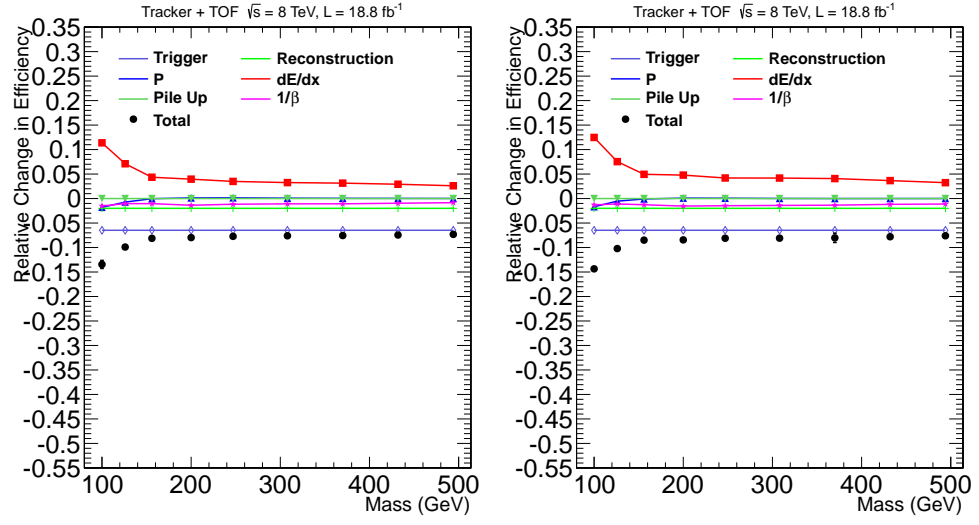
134

Figure 5.43: Relative signal efficiency change seen for the various sources of uncertainty for stau models in the *muon+track* analysis. GMSB (left) and Pair Prod. (right) models.
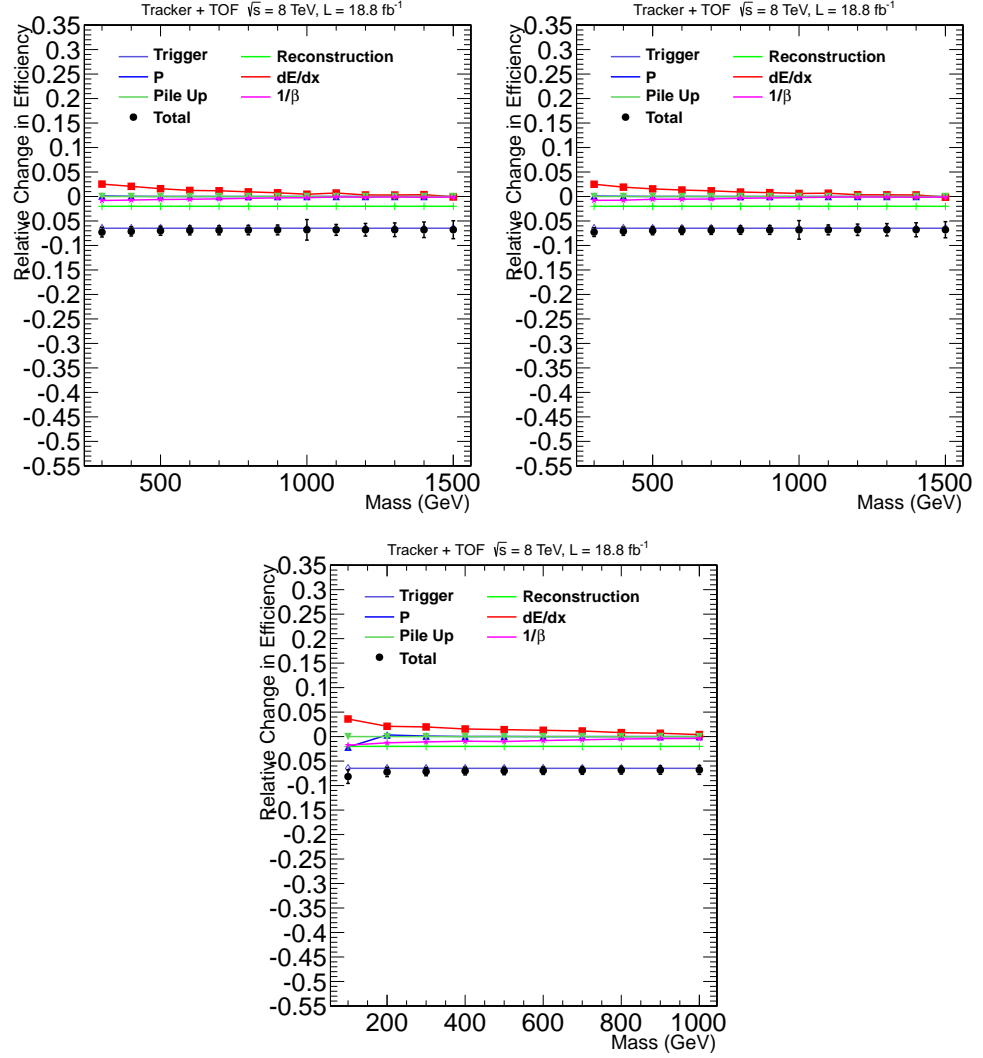
Figure 5.44: Relative efficiency change seen for the various sources of uncertainty for $R-hadron$ models in the $muon+track$ analysis. Top row: Gluino with $f = 0.5$ (left) and $f = 0.1$ (right). Bottom row: Stop
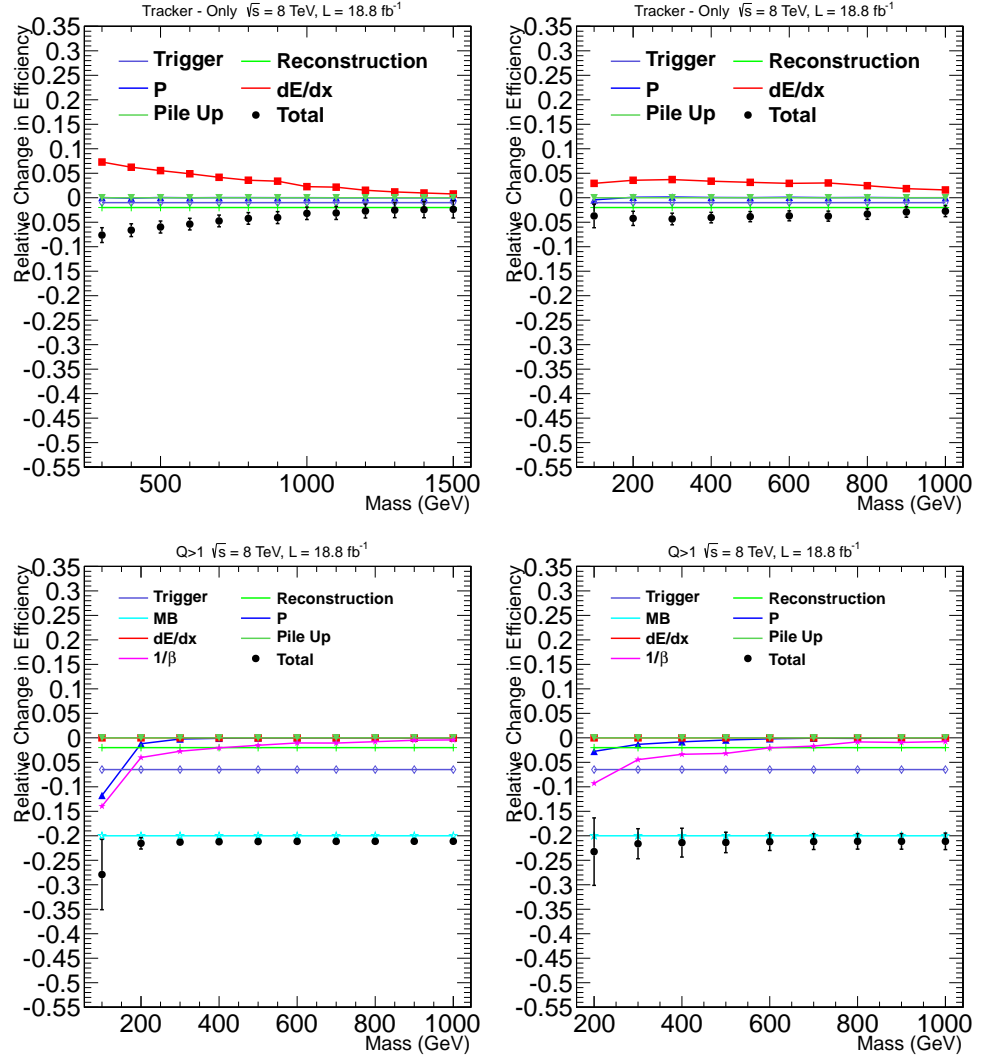
Figure 5.45: Relative signal efficiency change seen for the various sources of uncertainty. Top row: Charge suppressed Gluino with $f = 0.1$ (left) and charge suppressed stop (right) in the *track only* analysis. Bottom row: Q = 4e (left) and 7e (right) in the *multiple charge* analysis.
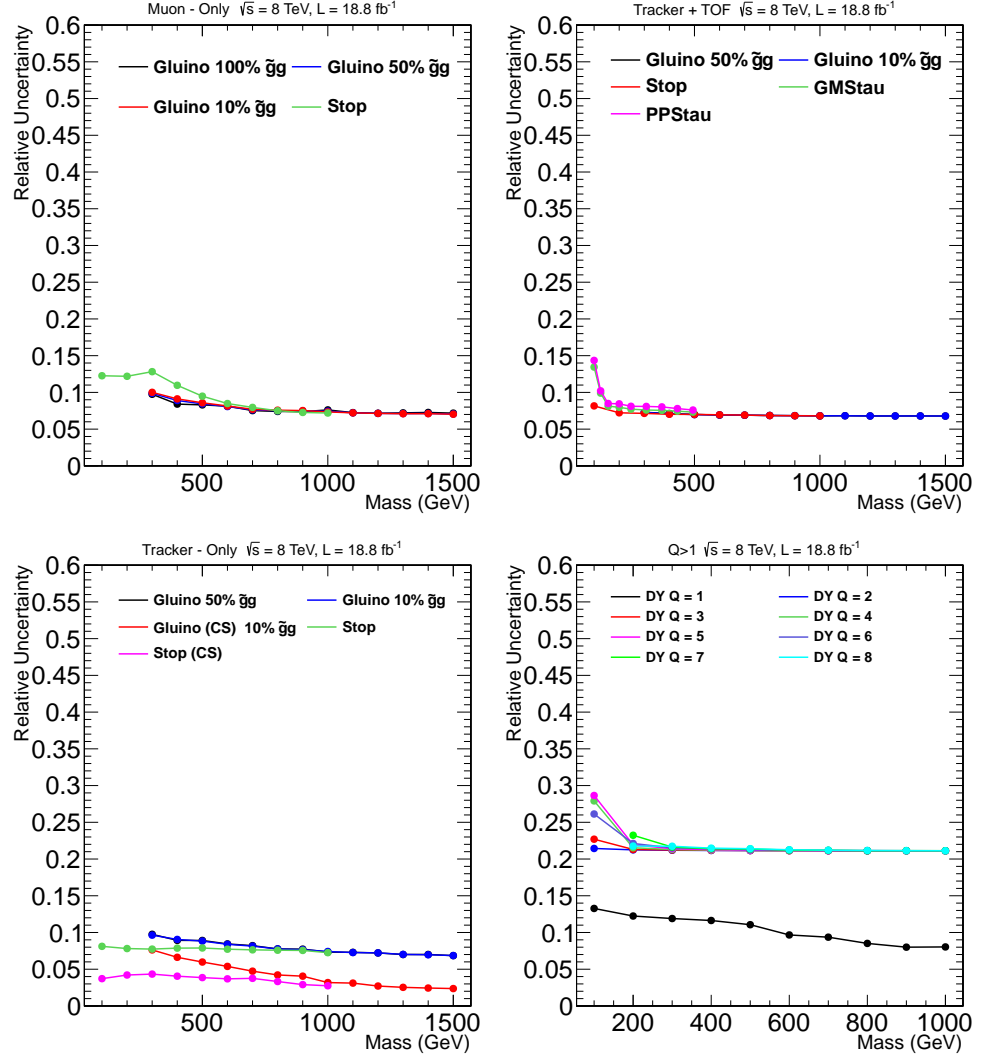
Figure 5.46: Total signal efficiency uncertainty for all considered models. Top: For the *muon only* (left) and *muon+track* (right) analyses. Bottom: For the *track only* (left) and *multiple charge* (right) analyses.
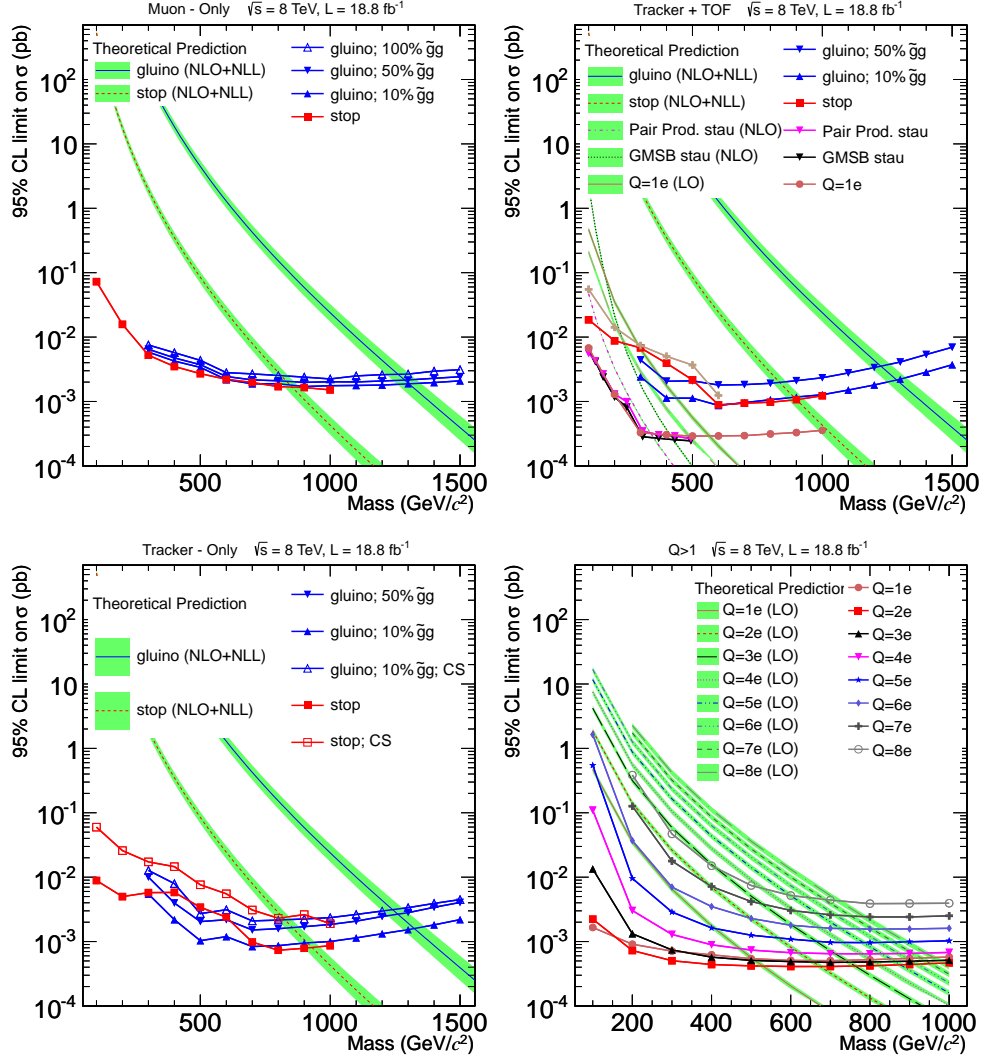
Figure 5.47: Cross-section limits obtained from 8 TeV data for all considered models in the *muon only* (top left), *muon+track* (top right), *track only* (bottom left), and *multiple charge* analyses.
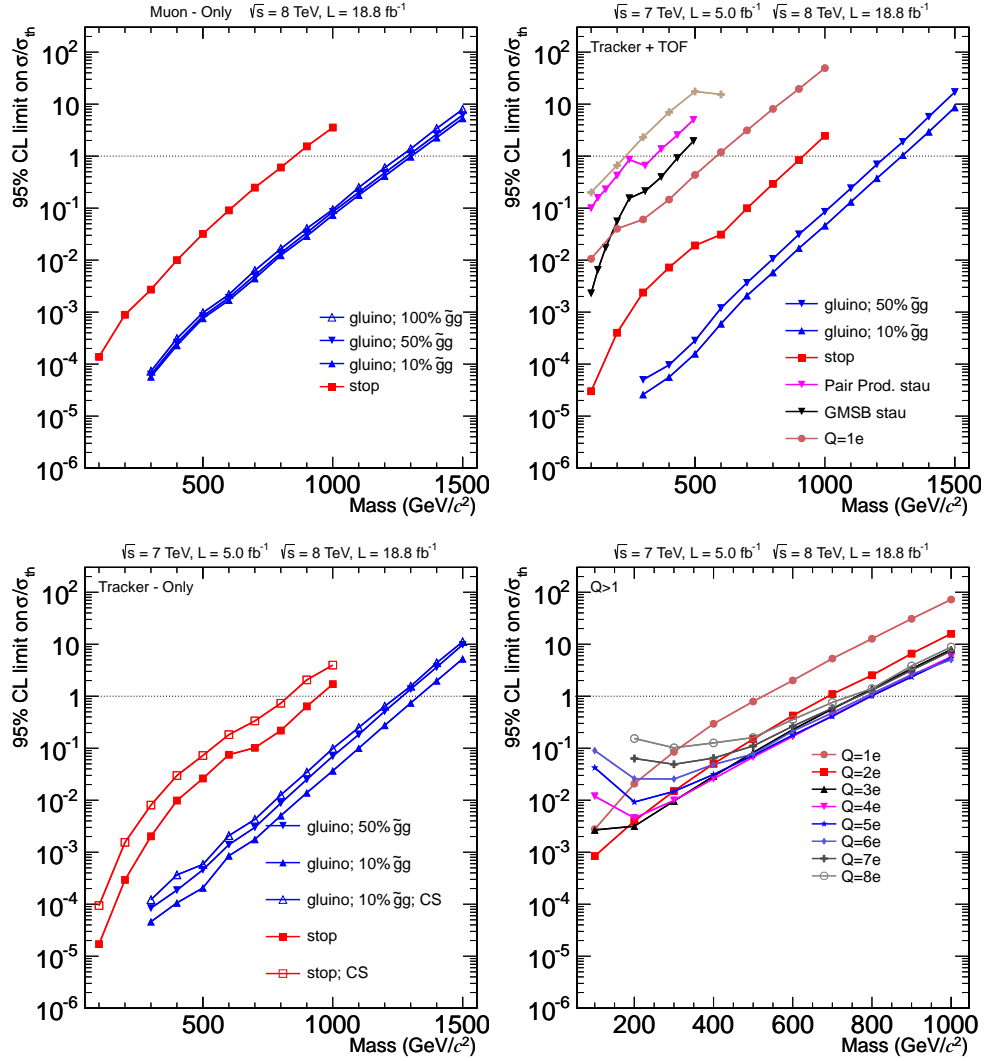
Figure 5.48: Limits on the relative signal strength, σ/σ_{th}, set by the *muon only* (top left), *muon+track* (top right), *track only* (bottom left), and *multiple charge* analyses. The *muon only* limit uses only 8 TeV data while the others use a combination of 7 and 8 TeV.
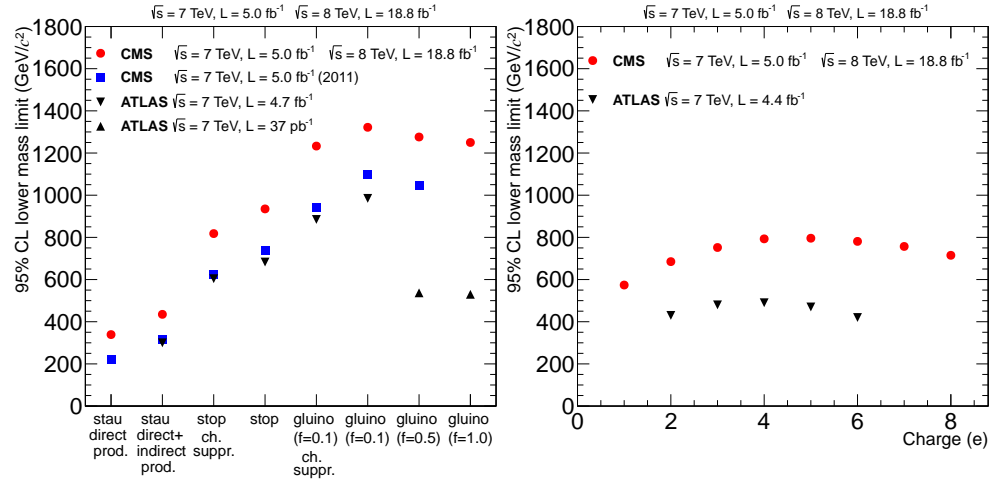
Figure 5.49: Lower mass limits at 95% CL on various SUSY models compared with previously published results [28, 27, 26, 31, 32, 25, 30]. The model type is defined by the x-axis (left). Mass limits for Drell–Yan like production of multiply charged particles versus electric charge (right).

CHAPTER 6

Conclusion

The measurement of the arrival time of hits in the CMS muon system is important for two reasons. The first is to quickly associate hits in the muon system with the appropriate LHC bunch crossing so that the data in the other subdetectors about this collision can be read out. A method was developed to measure the time offset of CSC chambers with respect to a determined optimal time that would give the best performance. The efficiency for chambers to correctly identify the right bunch crossing was brought to 99%, exceeding the design requirement of 92%. The second reason timing is important is to help identify different types of particles.

One of the particles timing can help identify is new heavy long-lived charged particles which would live long enough to interact directly with CMS and would be traveling at an appreciably slower speed than muons. Four searches were performed looking for particles of this type, each being sensitive to different signatures HSCP could have inside of CMS. The searches were performed by looking for tracks with some combination of high momentum, late arrival time in the muon system, or large ionization energy loss in the inner tracker. Backgrounds to the searches were muons form the collisions and in one of the searches muons from cosmic rays. The background in the signal region was predicted using control regions in data and the robustness of the prediction was checked by looking in the control region where particles would be traveling faster than the speed of light.

No excess above the expected background from SM processes was found in any of the four searches. Limits were placed on the production of long-lived charged particles created in many different theories, including versions of supersymmetry. These limits place important bounds on the theories of physics beyond the SM. While no discovery of new long-lived charged particles was found in the data searched there may be other signs of new physics present. Careful study of the recently discovered Higgs Boson-like particle is underway and many other searches are ongoing looking for the production of new particles. In addition, after a two year shutdown, the LHC will restart operations at a higher collision energy and rate which will allowing for probing the production of new physics at even smaller rates. Thus, a major discovery to reshape particle physics may be not far out of reach.

References

[1] D. Griffiths. *Introduction to Elementary Particles*. Physics Textbook. Wiley, 2008.

[2] Lyndon Evans and Philip Bryant. Lhc machine. *Journal of Instrumentation*, 3(08):S08001, 2008.

[3] Serguei Chatrchyan et al. Observation of a new boson with mass near 125 GeV in pp collisions at sqrt(s) = 7 and 8 TeV. 2013.

[4] Georges Aad et al. Observation of a new particle in the search for the Standard Model Higgs boson with the ATLAS detector at the LHC. *Phys.Lett.*, B716:1–29, 2012.

[5] Stephen P. Martin. A Supersymmetry primer. 1997.

[6] Xerxes Tata. What is supersymmetry and how do we find it? 1997.

[7] Mark Srednicki. *Quantum Field Theory*. Cambridge University Press, 1 edition, February 2007.

[8] M. Fairbairn, A.C. Kraan, D.A. Milstead, T. Sjostrand, Peter Z. Skands, et al. Stable massive particles at colliders. *Phys.Rept.*, 438:1–63, 2007.

[9] Aafke Christine Kraan. Interactions of heavy stable hadronizing particles. *Eur.Phys.J.*, C37:91–104, 2004.

[10] Rasmus Mackeprang and Andrea Rizzi. Interactions of Coloured Heavy Stable Particles in Matter. *Eur.Phys.J.*, C50:353–362, 2007.

[11] Rasmus Mackeprang and David Milstead. An Updated Description of Heavy-Hadron Interactions in GEANT-4. *Eur.Phys.J.*, C66:493–501, 2010.

[12] G.F. Giudice and R. Rattazzi. Theories with gauge mediated supersymmetry breaking. *Phys.Rept.*, 322:419–499, 1999.

[13] Paul Langacker and Gary Steigman. Requiem for an FCHAMP? Fractionally CHArged, Massive Particle. *Phys.Rev.*, D84:065040, 2011.

[14] S. Chatrchyan et al. The CMS experiment at the CERN LHC. *JINST*, 3:S08004, 2008.

[15] G. BBayatian et al. *CMS Physics: Technical Design Report Volume 1: Detector Performance and Software.* Technical Design Report CMS. CERN, Geneva, 2006. There is an error on cover due to a technical problem for some items.

[16] R. Barate et al. Search for pair production of longlived heavy charged particles in e^+e^- annihilation. *Phys. Lett. B*, 405:379, 1997.

[17] P. Abreu et al. Search for heavy stable and longlived particles in e^+e^- collisions at $\sqrt{s} = 189$GeV. *Phys. Lett. B*, 478:65, 2000.

[18] P. Achard et al. Search for heavy neutral and charged leptons in e^+e^- annihilation at LEP. *Phys. Lett. B*, 517:75, 2001.

[19] G. Abbiendi et al. Search for stable and longlived massive charged particles in e^+e^- collisions at $\sqrt{s} = 130$GeV to 209GeV. *Phys. Lett. B*, 572:8, 2003.

[20] A. Aktas et al. Measurement of anti-deuteron photoproduction and a search for heavy stable charged particles at HERA. *Eur. Phys. J. C*, 36:413, 2004.

[21] V. M. Abazov et al. Search for long-lived charged massive particles with the D0 detector. *Phys. Rev. Lett.*, 102:161802, 2009.

[22] T. Aaltonen et al. Search for long-lived massive charged particles in 1.96TeV $\bar{p}p$ collisions. *Phys. Rev. Lett.*, 103:021802, 2009.

[23] V.M. Abazov et al. A search for charged massive long-lived particles. *Phys. Rev. Lett.*, 108:121802, 2012.

[24] Victor Mukhamedovich Abazov et al. Search for charged massive long-lived particles at $\sqrt{s}$=**1.96** TeV. *Phys. Rev. D*, 87:052011, 2013.

[25] Vardan Khachatryan et al. Search for heavy stable charged particles in pp collisions at $\sqrt{s} = 7$TeV. *JHEP*, 03:024, 2011.

[26] Georges Aad et al. Search for Massive Long-lived Highly Ionising Particles with the ATLAS Detector at the LHC. *Phys.Lett.*, B698:353–370, 2011.

[27] Georges Aad et al. Search for stable hadronising squarks and gluinos with the ATLAS experiment at the LHC. *Phys.Lett.*, B701:1–19, 2011.

[28] Georges Aad et al. Search for Heavy Long-Lived Charged Particles with the ATLAS detector in *pp* collisions at $\sqrt{s} = 7$ TeV. *Phys.Lett.*, B703:428–446, 2011.

[29] Serguei Chatrchyan et al. Search for fractionally charged particles in *pp* collisions at $\sqrt{s} = 7$TeV. 2012.

[30] Serguei Chatrchyan et al. Search for heavy long-lived charged particles in *pp* collisions at $\sqrt{s} = 7$ TeV. *Phys.Lett.*, B713:408–433, 2012.

[31] Georges Aad et al. Searches for heavy long-lived sleptons and R-Hadrons with the ATLAS detector in *pp* collisions at $\sqrt{s} = 7$ TeV. *Phys. Lett. B*, 720:277, 2013.

[32] Georges Aad et al. Search for long-lived, multi-charged particles in pp collisions at $\sqrt{s} = 7$TeV using the ATLAS detector. 2013.

[33] Carola F. Berger, James S. Gainer, JoAnne L. Hewett, and Thomas G. Rizzo. Supersymmetry Without Prejudice. *JHEP*, 02:023, 2009.

[34] Matthew W. Cahill-Rowley, JoAnne L. Hewett, Ahmed Ismail, and Thomas G. Rizzo. More energy, more searches, but the pMSSM lives on. 2012.

[35] Nima Arkani-Hamed and Savas Dimopoulos. Supersymmetric unification without low energy supersymmetry and signatures for fine-tuning at the LHC. *JHEP*, 0506:073, 2005.

[36] G.F. Giudice and A. Romanino. Split supersymmetry. *Nucl.Phys.*, B699:65–89, 2004.

[37] Torbjorn Sjostrand, Stephen Mrenna, and Peter Z. Skands. A Brief Introduction to PYTHIA 8.1. *Comput.Phys.Commun.*, 178:852–867, 2008.

[38] B.C. Allanach, M. Battaglia, G.A. Blair, Marcela S. Carena, A. De Roeck, et al. The Snowmass points and slopes: Benchmarks for SUSY searches. *Eur.Phys.J.*, C25:113–123, 2002.

[39] Frank E. Paige, Serban D. Protopopescu, Howard Baer, and Xerxes Tata. ISAJET 7.69: A Monte Carlo event generator for pp, anti-p p, and e+e- reactions. 2003.

[40] Torbjorn Sjostrand, Stephen Mrenna, and Peter Z. Skands. PYTHIA 6.4 Physics and Manual. *JHEP*, 0605:026, 2006.

[41] Jet Performance in pp Collisions at 7 TeV. 2010.

[42] J. Beringer et al. Review of Particle Physics (RPP). *Phys. Rev.*, D 86:010001, 2012.

[43] W. T. Eadie, D. Drijard, F. E. James, M. Roos, and B. Sadoulet. *Statistical methods in experimental physics*. North Holland, Amsterdam, 1971.

[44] F. James. *Statistical methods in experimental physics*. World Scientific, Singapore, 2006.

[45] A L Read. Modified frequentist analysis of search results (the cl_s method). (CERN-OPEN-2000-205), 2000.

[46] Glen Cowan, Kyle Cranmer, Eilam Gross, and Ofer Vitells. Asymptotic formulae for likelihood-based tests of new physics. *Eur.Phys.J.*, C71:1554, 2011.

[47] CMS Collaboration. Absolute calibration of the luminosity measurement at CMS: Winter 2012 update. CMS Physics Analysis Summary CMS-PAS-SMP-12-008, CMS, 2012.

[48] The CMS Collaboration. Performance of CMS muon reconstruction in pp collision events at $\sqrt{s} = 7$ TeV. *Journal of Instrumentation*, 7:2P, October 2012.

[49] Measurement of tracking efficiency. Technical Report CMS-PAS-TRK-10-002, CERN, 2010. Geneva, 2010.

[50] CMS Collaboration. Precise mapping of the magnetic field in the CMS barrel yoke using cosmic rays. *Journal of Instrumentation*, 5:3021, March 2010.